# ASTEROSEISMOLOGY OF RED GIANT STARS: A TOOL FOR CONSTRAINING STELLAR MODELS

by

Diego Bossini

**A thesis submitted to the University of Birmingham for the degree of DOCTOR OF PHILOSOPHY**

School of Physics and Astronomy
University of Birmingham
June 2016

*A Nonno Gino*

# Abstract

The aim of this thesis is to study stellar evolution and asteroseimology of red-giant stars mainly from a modelling point of view, in particular the impact on core-convective-burning stars of adopting different mixing schemes. Thanks to NASA space telescope *Kepler*, asteroseismology of thousands of giants provided us new information related to their internal structure, that can be used for finding constraints on their cores. I used several stellar evolution codes (MESA, BaSTI, and PARSEC) to investigate the effect of different mixing schemes in the helium-core-burning stars. Comparing them with observed stars, I concluded that standard stellar models, largely used in literature, cannot describe the combined observed distribution of luminosity and period spacing. I then proposed as solution a penetrative convection model with moderate overshooting parameter. Additional tests on Kepler's open clusters (NGC6791 and NGC6819) and secondary clump stars, allowed me to revised to my mixing model.

# Ringraziamenti

Un grandissimo grazie ad Andrea per questi straordinari, indimenticabili quattro anni, non avrei potuto desiderare un migliore supervisor e amico. Per avermi sempre fatto sentire il benvenuto, grazie a Bill, Yvonne e tutti i componenti del gruppo HiROS. Grazie a Guy, Tiago, Nadege, Daniel, Rasmus, Mikkel, Hugo, Caitlin, James, Tom, Matt e Ben per tutte le discussioni, l'aiuto, le cene e le risate. Grazie anche ai miei collaboratori, in particolare a Maurizio, Léo, Josefina, Santi e Arlette. Un grazie a Sara, Emma e Anita per avermi fatto sentire un po' più a casa. E infine, un grazie a mia madre e a mio padre e alla mia famiglia per aver sempre supportato (e sopportato) tutte le mie scelte in questi 11 lunghi anni di università.

A great thank to Andrea for these terrific and unforgettable four years, I could not ask for a better supervisor and friend. For always making me feel welcome, thank to Bill, Yvonne, and all the members of the HiROS group. Thank to Guy, Tiago, Nadege, Daniel, Rasmus, Mikkel, Hugo, Caitlin, James, Tom, Matt, and Ben for all the discussions, the help, the dinners, and the laughs. Thank to all my collaborators and in particular to Maurizio, Léo, Josefina, Santi, and Arlette. Thank also to Sara, Emma, and Anita for having made me feel a little more at home. Last but not least, a special thank to Mum and Dad and family for always having supported me in all my choices in these eleven years of university.

# Contents

# Statement of Collaboration

Part of this thesis has been written with the contribution of many collaborators. The following section are reported as written Bossini et al. (2015), in which I highlight the contribution of Andrea Miglio, Maurizio Salaris, Adriano Pietrinferni, Josefina Montalbán, Alessandro Bressan, Arlette Noels, Santi Cassisi, Léo Girardi, and Paola Marigo:

- Introduction, third paragraph.
- Chapter 3, Sections 3.2.1 and 3.2.2.
- Chapter 4, Sections from 4.1 to 4.4 and Section 4.6

For the observed data in Chapter 5 and 6, I thank Mathieu Vrard, Benoit Mosser, and the APOKASC collaboration.

Diego Bossini

# Introduction

In recent years, seismology of red-giant stars has become an extraordinarily fruitful field in stellar astrophysics, mainly thanks to the availability of data of unprecedented quality from the space-based telescopes *Kepler* and CoRoT. Red-giant stars have very rich frequency spectra that provide, for the first time, direct constrains on their internal structures, which are inaccessible to traditional observations. Using a combination of theoretical models, photospheric and asteroseismic constraints, it is now possible to make a step forward in the study of the physical processes that occur in their interiors and in the determination of their global parameters (like mass, age, distance, and metallicity). This has strong implication on both our understanding of stellar physics and on the characterisation of stellar populations in our Galaxy.

This thesis is mainly focused on red giants in their helium-core burning phase. The helium-core-burning (HeCB) phase of low-mass stars affects many aspects of their subsequent evolution, and has therefore been the subject of numerous studies in the literature. In particular, the red clump (RC) is a well-known feature in the Hertzsprung-Russell diagram – as well as the color-magnitude diagram – of simple and composite stellar populations, and is associated to the low-mass, metal-rich stars in the He-core-burning phase (Cannon, 1970). The RC plays a key role in many fields of astrophysics: its luminosity, for instance, can be used as a distance and age indicator of clusters and nearby galaxies, while the observed chemical composition of its members is useful to investigate the chemical evolution of galaxies (e.g., see Girardi & Salaris, 2001; Catelan, 2009; Nidever et al., 2014).

Current models of the internal structure and evolution of such stars, however, still suffer from systematic uncertainties which are due in most cases to our limited understanding of the physical processes in stellar conditions (energy transport and nuclear processes). In particular, predictions of stellar lifetimes in the HeCB phase are strongly dependent on the (poorly constrained) amount of mixing applied beyond boundaries of convective regions and on the adopted definition (and correct implementation) of such boundaries (e.g. see Chiosi 2007; Castellani, Giannone & Renzini 1971a; Gabriel et al. 2014; Bressan et al. 2015). Crucially, our ability to

test models has been limited so far by the lack of observational constraints which are specific to the internal structure of evolved stars.
Asteroseismology of thousands of red giants observed by CoRoT (Baglin et al., 2006) and *Kepler* (Borucki et al., 2010) has changed the situation. We can now use the pulsation frequencies to place tight constraints not only on the fundamental stellar properties, but also to probe their internal structure (see e.g. Chaplin & Miglio 2013 and references therein). In particular, as presented in Montalbán et al. (2013), the frequencies of oscillation modes detected in HeCB stars are sensitive diagnostics of the chemical and thermal stratification of the energy-generating core, providing us with a novel and independent constraint, which is specific to the core structure of HeCB stars.
The main aim of this thesis is to use these new seismic constrains in order to take a significant step forward in the characterization and quantification of uncertainties in stellar modelling, with the final goal to produce accurate models.

This thesis is organized as follows:
The first part presents an overview of the foundations of stellar structure, evolution, and pulsation theory.

- In Chapter 1 I will give a brief introduction to low- and intermediate-mass stars, which are the main subject of this thesis. I will describe the evolution of their internal structure and the main physical processes involved.
- In Chapter 2 I will introduce the theory behind stellar oscillations. I will derive the general equations that describe them, and I will then describe the evolution of the oscillation properties of a low-mass stars, from the main sequence to the early asymptotic giant branch.

In the second part I focus on the original results obtained in my work.

- The first part of Chapter 3 is dedicated to the description of the micro and macro physics used as an input in the stellar evolution models presented in this thesis. I will introduce my investigation on the near-core mixing in helium-core-burning stars, giving an exhaustive review of the possible mixing treatments that various codes adopt during this phase. The second part concerns the description of the tools I used to extract seismic information from stellar models (large separation of the acoustic modes and small separations $\delta_{01}$ and

$\delta_{02}$). The discussion includes few practical application of the technical work described in this chapter.

- Chapter 4 describes the work presented in Bossini et al. (2015). I will show how in low mass stars, classical parameters (luminosity) can be combined with global seismic attributes (period spacing) in order to constrain the properties of the mixed core during the helium-core burning phase, discriminating between competing models. I will outline an optimum model able to describe simultaneously the observed distribution of luminosity and period spacing in the APOKASC sample.

- Chapter 5 aims to continue the work started in Chapter 4, testing model predictions using the period spacing of red clump stars observed in the old-open clusters monitored by *Kepler*. I will also evaluate the uncertainties that chemical composition, mass, and $^{12}C(\alpha,\gamma)^{16}O$ reaction rates introduce in the prediction of the period spacing.

- The last chapter contains my preliminary results on the study secondary clump stars. The particular behaviour of period spacing during the He-core burning as a function of mass is strongly dependent on the core mixing during the main sequence. This allows me to investigate and calibrate the size of the mixed core also for these phases, which is one of the major current uncertainties in stellar models.

# Part I

# Theoretical Background

# Chapter 1

# Stellar Evolution of Low- and Intermediate-Mass Stars

The main subject of this thesis is the study of stars with masses belonging to the interval between $0.45 - 0.55$ and $5 - 6$ solar masses ($M_\odot$).In the first part of this chapter I will briefly introduce some of the physical processes that occur in such stars in order to outline the **four fundamental equations** of stellar structure. These define a system of differential equations that specifically designed codes need to solve to predict the structure and evolution of stars, along with a set of ordinary relations between the thermodynamic variables involved (i.e pressure, density, temperature, and mean molecular weight).
The four equations of stellar structure:

**1 equation of hydrostatic equilibrium** (conservation of momentum)

$$\frac{\mathrm{d}P(r)}{\mathrm{d}r} = -\frac{\mathrm{G}M(r)\rho}{r^2}. \tag{1.1}$$

**2 mass continuity equation** (conservation of mass)

$$\frac{\mathrm{d}M(r)}{\mathrm{d}r} = 4\pi r^2 \rho. \tag{1.2}$$

**3 equation of energy transport** (temperature stratification)

radiative

$$\frac{\mathrm{d}T(r)}{\mathrm{d}r} = \frac{3}{16\pi acG}\frac{\kappa\rho}{r^2T^3}L(r). \tag{1.3}$$

convective

$$\frac{\mathrm{d}T(r)}{\mathrm{d}r} = \frac{\Gamma_2 - 1}{\Gamma_2}\frac{T}{P}\frac{\mathrm{d}P(r)}{\mathrm{d}r}. \tag{1.4}$$

**4 energy equation** (conservation of energy)

$$\frac{\mathrm{d}L(r)}{\mathrm{d}r} = 4\pi r^3 \rho(\epsilon_{nuc} - \epsilon_\nu + \epsilon_g), \tag{1.5}$$

where $P$ is the pressure, $\rho$ is the density, $T$ is the temperature, $L$ is the luminosity, $\Gamma_1$ is an adiabatic coefficient, $\epsilon$ terms are the energy generation rates from different sources, $M$ and $r$ are respectivelly the mass and radius coordinates, and G, a, and c are three physical constants (Gravitational constant, radiation constant, and light speed). Explanations of the single terms will be given in the following paragraphs.
Based on their mass, we can divide the stars studied in this thesis in two main categories (according to the definition given by Kippenhahn, Weigert & Weiss, 2013, from now on KWW):

> **low-mass stars** (LMS). *From* $0.45 - 0.55$ *to* $1.80 - 2.20$ $M_\odot$. Stars that form electron-degenerate helium cores after the end of hydrogen-burning phase and ignite the helium nuclear reaction in a highly-degenerate condition.
>
> **intermediate-mass stars** (IMS). *From* $1.80 - 2.20$ *to* $5 - 6$ $M_\odot$. Stars that can ignite helium nuclear reactions in non-degenerate conditions, but, like LMS, terminate their evolution as carbon-oxygen white dwarfs.

The limits given are slightly dependent on the initial chemical composition of the star, i.e. the **helium mass fraction** $Y$ and the **metallicity** $Z$ (mass fraction of all the elements with atomic number greater than helium). It must be notice that the upper limit given to the IMS is referred to the range of interest of this thesis, while, in reality, masses up to $\sim$10 $\mathrm{M}_\odot$ are still considered intermediate masses.
Additional categories are the **very-low-mass stars** (VLMS), with masses smaller than $0.45 - 0.55$ $\mathrm{M}_\odot$, and **massive stars** ($M > 10$ $\mathrm{M}_\odot$). Their characteristics, however, will not be (or just partially) discussed here. I refer an interested reader to KWW.

## 1.1 Mechanic Equilibrium

### 1.1.1 Hydrostatic Equilibrium

Stars usually maintain a status of equilibrium between the expanding and collapsing forces, called hydrostatic equilibrium. For a spherical non-rotating and non-magnetic

star, the hydrostatic equilibrium requires a perfect balance between the pressure-gradient forces and the gravity forces in each point of its structure:

$$\frac{\mathrm{d}P}{\mathrm{d}r} = -\frac{GM(r)}{r^2}\rho. \tag{1.6}$$

Deviations from eq. 1.7 generate a restoring force with acceleration

$$\frac{\mathrm{d}^2r}{\mathrm{d}t^2}\frac{1}{\rho}\frac{\mathrm{d}P}{\mathrm{d}r} + \frac{GM(r)}{r^2}, \tag{1.7}$$

from which we can derive a characteristic timescale, called **hydrostatic timescale** ($\tau_{\mathrm{hydr}}$), by imposing equal to zero one of the two terms in the right part of the equation. The hydrostatic timescale indicates the time necessary to a sound wave generated in the centre to reach the surface and is equal to the time of free fall ($\tau_{\mathrm{ff}}$), obtained imposing to zero the pressure term in eq. 1.7, or, alternatively, to the explosion timescale ($\tau_{\mathrm{expl}}$, gravity term to zero). The hydrostatic timescale is equal to:

$$\tau_{\mathrm{hydr}} = \sqrt{\frac{3}{2\pi}\frac{1}{G\bar{\rho}}}, \tag{1.8}$$

where $\bar{\rho}$ is the mean density of the star. For the Sun, $\tau_{\mathrm{hydr}}$ is about 27 minutes, while a small deviation of the order of 1% from the hydrostatic equilibrium generates an acceleration that contracts (or expands) the stellar radius of about 10% in a timescale of hours (Chiosi, 2008). Since a similar situation has never been observed, the condition of hydrostatic equilibrium in stars is generally fulfilled. Despite for few exceptions (collapsing protostars and evolved iron-core stars), $\tau_{\mathrm{hydr}}$ is several orders of magnitude smaller than any timescales corresponding to radius changes in stellar evolution theory (e.g the ascent on the red giant branch, see section 1.4.3). Therefore we can consider that a star evolves through approximatively continuous states of hydrostatic equilibrium in its evolution.

### 1.1.2 Mass Distribution

The second equation of stability (mass continuity equation) simply states that the total mass $M$ remains constant with time and is given by the integration of the density $\rho$ over the volume:

$$M = \int_0^R 4\pi r^2 \rho \mathrm{d}r. \tag{1.9}$$

In differential form it can be written as:

$$\frac{\mathrm{d}M(r)}{\mathrm{d}r} = 4\pi r^2 \rho, \tag{1.10}$$

which means that a variation of radius in a spherical shell, at fixed time, induces a variation of mass that maintains constant their ratio. Equation 1.10 is particularly useful to change the system of coordinates from Lagrangian (independent variables mass and time) to Eulerian (independent variables radius and time):

$$\frac{\mathrm{d}}{\mathrm{d}M(r)} = \frac{\mathrm{d}}{\mathrm{d}r}\frac{1}{4\pi r^2 \rho}. \tag{1.11}$$

### 1.1.3 Equation of State

An **equation of state** (EoS) is an expression that describes the behaviour of pressure in function of the other thermodynamic quantities, like temperature $T$, density, and mean molecular weight $\mu$ (average mass of the particles in a gas divided by the atomic mass unit). In stellar evolution, we can encounter several types of equation of states, specifically designed to describe particular gas conditions. In the mass interval of the LMS and IMS stars, we are mainly interested in these EoS:

**perfect non-relativistic gas**. In a non-relativistic gas of ions and electrons, the pressure is simply described by the Boyle's law:

$$P = \frac{k_\mathrm{B}\rho T}{m_\mathrm{u}\mu}. \tag{1.12}$$

This EoS is typical of stellar cores with nuclear-burning and the envelopes.

**degenerate non-relativistic gas**. The EoS of a degenerate gas of electrons follows the Fermi-Dirac statistics and the expression for pressure results to be dependent only on the density. Therefore any changes in temperature will not impact the pressure. The expression is:

$$P_\mathrm{e} \propto \rho^{5/3}, \tag{1.13}$$

where the power equal to 5/3 indicates that the gas in non-relativistic. The complete degenerate gas of electrons is an extreme case, nevertheless, it can be used as a good approximation in case of high $\mathrm{e}^-$-degeneracy scenarios. Moreover, the total gas pressure is given by the sum of the electron pressure with the ion pressure, that is usual in the perfect gas condition. For stars that

belong to the LMS and IMS mass interval, this condition is typical of their cores during the red-giant branch, asymptotic-giant branch, and white dwarf evolutionary phases (see sections 1.4.3 and 1.4.6).

**gas of photons**. The radiative pressure is described by a relativistic gas of bosons and its expression depends only on the temperature:

$$P = \frac{1}{3} a T^4, \tag{1.14}$$

where $a$ is the radiation density constant. If we consider a system with a mixture of radiation and particles behaving like an ideal, the total pressure will be given by the sum of eq. 1.12 and 1.14 (particle and radiation parts). The radiative pressure will be particularly relevant at high temperature, where the $T^4$ term in the radiative parts dominates, or at low density, that only affects the particle part.

## 1.2 Energy Transport in Stellar Interiors

From the centre to the surface of a star, there is a small, usually negative, gradient of temperature $\frac{\mathrm{d}T}{\mathrm{d}r}$. Therefore, stars have mechanisms to transport heat from hotter to the colder regions. The main types of energy transport are:

- **radiation**. Energy is carried outward by photons.
- **conduction**. Collision of electrons and nuclei.
- **convection**. Energy is transported by macroscopic movements of material.

In addition, there is also a fourth type: the energy loss by neutrino emission, that becomes relevant in electron-degenerate condition (e.g at the final stage of the RGB phase and at the start of the helium flash, see section 1.4.4). Since the cross section of the neutrinos with the matter is very low, they escape easily from the star.
Each of these mechanisms is responsible for a component of the local flux of energy. The determination of the dominant mechanism will give fundamental information about thermodynamic and chemical properties in each point of a stellar structure, like for instance the local $\frac{\mathrm{d}T}{\mathrm{d}r}$. The conductive energy transport is usually relevant only in degenerate conditions (typical e.g. of the red giant branch star cores, section 1.4.3), while for the other cases its contribution can be easily neglected (KWW). In the remaining cases, usually the only two important mechanisms present are radiation and convection.

### 1.2.1 Radiative Energy Transport

The energy transport by radiation in stars is characterized by extremely frequent processes of emission, absorption, and scattering of photons that results in a net flux of energy from the hotter to colder layers. The expression that describes this flux can be written in form of diffusive equation:

$$F_{\rm rad} = -\frac{4acT^3}{3\kappa\rho}\frac{{\rm d}T}{{\rm d}r}, \tag{1.15}$$

where $c$ is the speed of light, $T$ is the temperature, $\rho$ the density, and $\kappa$ is the mean absorption coefficient (or **opacity**, radiative cross section per unit mass averaged over frequency). The equation 1.15 is built under the condition that the mean free path of the photons is small compared to the scale of variation of temperature and is generally fulfilled over the entire structure of a star, with the only exception for the most external layers. The time necessary to transport the photons from the centre to the surface is of the order of about $10^5$ years.
Equation 1.15 can be also written substituting the flux with the local luminosity $l$

$$l(r) = -4\pi r^2\frac{4acT^3}{3\kappa\rho}\frac{{\rm d}T}{{\rm d}r} = -\frac{16\pi ac}{3}\frac{r^2T^3}{3\kappa\rho}\frac{{\rm d}T}{{\rm d}r}. \tag{1.16}$$

Rearranging the formula in order to get $\frac{{\rm d}T}{{\rm d}r}$, and introducing the logarithmic gradient of temperature $\nabla = {\rm d}\ \ln T/{\rm d}\ \ln P$, we find:

$$\nabla_{\rm rad} = -\frac{3}{16\pi acG}\frac{\kappa lP}{mT^4}. \tag{1.17}$$

$\nabla_{\rm rad}$ is a fictitious gradient of temperature that represents the value that the actual gradient temperature $\nabla_T$ would have if all the energy was transported by radiation. It is easy to notice that $\nabla_{\rm rad}$ increases in regions of strong energy generation (which is typical of the strong nuclear burning regions), and of high opacity (which is typical of the colder outer regions).

#### Opacity

The efficiency of radiative transport is strongly related to the value of the opacity, which, in turn, depends on the mechanisms of interaction between photons and matter. The main mechanisms of photon-particle interaction are:

**Thomson scattering**. A photon interacts with a free electron and modifies its direction without changing the frequency. The contribution of the Thomson

scattering to the opacity ($\kappa_{\rm Ths}$) is therefore independent from the frequency of the radiation and is given by the simple equation:

$$\kappa = 0.2(1 + X), \tag{1.18}$$

where $X$ is the mass fraction of hydrogen.

**free-free absorption**. In the proximity of a nucleus, a photon is absorbed by an electron, that increases its kinetic energy.

**bound-free absorption**. A bound electron absorbs a photon and becomes free.

**bound-bound absorption**. A bound electron absorbs a photon, moving into a higher-energy state.

At a given frequency $\nu$, the opacity is the sum of the contribution of the single processes:

$$\kappa_T(\nu) = [\kappa_{\rm ff}(\nu) + \kappa_{\rm bf}(\nu) + \kappa_{\rm bb}(\nu)] \cdot \left(1 - e^{\frac{-h\nu}{k_{\rm B}T}}\right) + \kappa_{\rm Ths}, \tag{1.19}$$

where the exponential term represents the effect of the stimulated emission. An atomic system in a radiation field of frequency $\nu$ , in fact, is stimulated to emit photons at the same frequency of the field, adding a negative contribution to the total opacity.

The correct determination of the single contributions to the opacity, however, requires complex calculations, since each process may be more or less efficient in different regions of the star, according to the thermal proprieties of the matter and the chemical mixture. Every element has different absorption and emission coefficients, which can also vary with temperature, density, and ionization state. In general the heavier elements are associated to higher opacities, therefore, also their abundance plays a fundamental role to determine the overall opacity, as we will see in the helium-core-burning and asymptotic giant branch stars (sections 1.4.5 and 1.4.6). For these reasons, nowadays stellar evolution codes use interpolation algorithms over pre-compiled tables in order to estimate the opacity value (see section 3.1.3 for details).

Assuming a Plank distribution of the radiative energy $B(\nu, T)$, the total opacity can be expressed by the **mean Rosseland opacity** equation:

$$\kappa = \left[ \frac{\int \frac{1}{\kappa_T(\nu)} \frac{{\rm d}B(\nu,T)}{{\rm d}T} {\rm d}r}{\int \frac{{\rm d}B(\nu,T)}{{\rm d}T} {\rm d}r} \right]^{-1} . \tag{1.20}$$

### 1.2.2 Conductive Energy Transport

The conductive energy transport is caused by the collisions between the particles in thermal motion. Its efficiency is usually negligible compared with the mechanism of radiation and convection, since the high densities of the stellar interiors guarantee that the particles have a mean free path significantly smaller than photons. However this condition is not fulfilled anymore in a electron-degenerate gas, typical, for instance, of LMS and IMS cores during the red-giant branch phase. The high degeneracy forces, in fact, the electrons in higher energy states since the lower are all occupied, with the consequence that their mean free path increase substantially. The conductive flux can be expressed as a diffusive equation of conductive coefficient $D_{\rm cond}$:

$$F_{\rm cond} = -D_{\rm cond}\frac{{\rm d}T}{{\rm d}r}. \tag{1.21}$$

### 1.2.3 Convective Energy Transport

Convection is a phenomenon that involves macroscopic movements of material and may affect large portions of a star. The simplest and most popular theory describing convective heat transport in stars is the **Mixing Length Theory** (MLT).
Consider a small parcel of matter in a perfect chemically homogeneous gas. If a small quantity of energy is introduced in the parcel, its temperature slightly rises by a quantity $\delta T$. The variation of temperature will lead the pressure to increase too. As a consequence, the density tends to decrease by $\delta\rho$ in order to restore the equilibrium of pressure between the parcel and the rest of the medium. The lower density generates a buoyancy force that pulls the parcel outwards for a distance of the order of $\Delta r$. Maintaining the equilibrium of pressure, the parcel will expand almost adiabatically. After the parcel has travelled a distance $\Delta r$ we have two possible scenarios: if the density of the parcel is lower than surroundings, then (1) the parcel will continue to rise (the medium is convectively unstable), in the opposite case, if the density is higher, (2) the parcel will tend to sink back to the initial position (the medium is convectively stable). Therefore, convection is established when the gradient of density of the parcel is steeper than the one of the surroundings or, in terms of temperature, if the temperature gradient of the parcel is:

$$\left|\frac{{\rm d}T}{{\rm d}r}\right|_{\rm parcel} < \left|\frac{{\rm d}T}{{\rm d}r}\right|_{\rm medium}. \tag{1.22}$$

Supposing that the parcel can only release energy to the surroundings by radiation

or conduction, its gradient of temperature will be similar to:

$$\left(\frac{\mathrm{d}T}{\mathrm{d}r}\right)_{\mathrm{s}} = \frac{\Gamma_2 - 1}{\Gamma_2}\frac{T}{P}\frac{\mathrm{d}P(r)}{\mathrm{d}r}, \tag{1.23}$$

where $\Gamma_2$ is one of the adiabatic exponents. This gradient, known as **adiabatic gradient of temperature**, can be written in logarithmic form as

$$\nabla_{\mathrm{ad}} = \frac{P\delta}{T\rho c_P}, \tag{1.24}$$

where $c_P$ is the specific heat capacity at constant pressure and $\delta$ is

$$\delta = \left(\frac{\mathrm{d}\ \ln\rho}{\mathrm{d}\ \ln T}\right)_P. \tag{1.25}$$

Similarly to the radiative case, $\nabla_{\mathrm{ad}}$ is a fictitious term that represents the gradient of temperature that a star would have if all the thermodynamic transformations were in adiabatic form. If all the energy is transported by radiation, then the temperature gradient of the medium (right term in eq. 1.22) would be equal to $\nabla_{\mathrm{rad}}$ (**radiative region**, $\nabla_T = \nabla_{\mathrm{rad}}$). Therefore, if we associate the temperature gradient of the parcel and the medium respectively to $\nabla_{\mathrm{ad}}$ and $\nabla_{\mathrm{rad}}$, the sufficient condition for convection in an homogeneous gas is (**Schwarzschild criterion**):

$$\nabla_{\mathrm{rad}} > \nabla_{\mathrm{ad}}. \tag{1.26}$$

In case of inhomogeneous gas, a gradient of $\mu$ is also present and the eq. 1.26 becomes (**Ledoux criterion**):

$$\nabla_{\mathrm{rad}} > \nabla_{\mathrm{ad}} + \frac{\chi_\mu}{\chi_T}\nabla_\mu, \tag{1.27}$$

where $\nabla_\mu = \partial \ln\mu / \partial \ln P$, while $\chi_\mu$ and $\chi_T$ are two of the set of three structure variables:

$$\chi_T = \left(\frac{\partial \ln P}{\partial \ln T}\right)_{\rho,\mu}, \quad \chi_\rho = \left(\frac{\partial \ln P}{\partial \ln \rho}\right)_{T,\mu}, \quad \chi_\mu = \left(\frac{\partial \ln P}{\partial \ln \mu}\right)_{T,\rho}. \tag{1.28}$$

If the condition for convention is fulfilled (**convective region**), the established motion of material will participate to the transport of heat from the hotter and deeper layers of a star to the colder and outer layers. The convective region will modify the temperature profile in order to reach an equilibrium between the radiative and convective transport and the actual $\nabla_T$ will assume a value between $\nabla_{\mathrm{rad}}$ and

$\nabla_{\rm ad}$ (**super-adiabaticity**). In the deeper convective regions the level of super-adiabaticity is expected to be small enough to consider with a good approximation $\nabla_T = \nabla_{\rm ad}$.

### Mixing Length Theory

In the regions where the super-adiabaticity is not negligible, like in the most external and coldest parts of the stars, the full treatment by MLT must be taken in account in order to determine the actual $\nabla_T$. To do that we need to derive the total flux of energy that will be given by the sum of the radiative and convective contribution (from eq. 1.16):

$$F = F_{\rm rad} + F_{\rm conv} = \frac{4acT^4 g}{3\kappa P}\nabla_{\rm rad} \tag{1.29}$$

(in the hypothesis that the conductive flux is negligible). $g$ is the local gravity. Since $F_{\rm rad}$ was been already derived in the paragraph 1.2.1 (eq. 1.15), the only expression that has to be determined is the convective flux. In analogy with the conductive transport, we can use a diffusive equation to describe the convective flux. Before dissolving, a convective element will move of a average quantity $\lambda_{\rm MLT}$ with a mean velocity $\bar{v}$, generating a flux equal to

$$F_{\rm conv} = \frac{1}{2}\rho\bar{v}c_P T\frac{\lambda_{\rm MLT}}{H_P}(\nabla_{T,\rm medium} - \nabla_{T,\rm parcel}) \tag{1.30}$$

where $H_p$ is the pressure of scale

$$\frac{1}{H_p} = -\frac{{\rm d}\ln P}{{\rm d}r} = \frac{\rho g}{P} \tag{1.31}$$

$\lambda_{\rm MLT}$ is usually taken equal to a factor $\alpha_{\rm MLT}$ multiplied by the pressure of scale. $\alpha_{\rm MLT}$ is an arbitrary value, normally calibrated on the Sun (see section 3.1.6). However, we still need to find an expression for the mean velocity $\bar{v}$. Given a convective element that shows a density excess of $\Delta\rho$ with respect to the surrounding density $\rho_0$, it will be affected by a buoyancy force per unit of volume:

$$f_{\rm B} = \left(-g - \frac{1}{\rho}\frac{\partial P}{\partial r}\right)\Delta\rho \approx \left(-g_0\frac{\Delta\rho}{\rho_0}\right)\Delta\rho = -g\Delta\rho \tag{1.32}$$

If the convective element, initially at rest, is accelerated by $f_{\rm B}$, after travelling a distance $\Delta r$, the new force that acts on it will be:

$$f_{\rm B} = -g\Delta\rho(\Delta r) \tag{1.33}$$

Using eq. 1.33, it is possible to calculate the mean work per unit of volume necessary to move the element by averaging on $\Delta r$ and introducing $\lambda_{\rm MLT}$:

$$\bar{W} = -\frac{1}{8}\Delta\rho(\lambda_{\rm MLT})\lambda_{\rm MLT} \tag{1.34}$$

In MLT it is claimed that that during the movement only half of $\bar{W}$ is converted in kinetic energy, therefore the mean velocity of the elements will be:

$$\frac{1}{2}\rho\bar{v}^2 = \frac{1}{2}\bar{W} \Longrightarrow \bar{v}^2 = -\frac{1}{8}\frac{\Delta\rho(\lambda_{\rm MLT})}{\rho}\lambda_{\rm MLT} \tag{1.35}$$

Introducing the gradient of temperature and the expression for $\bar{v}$ in eq. 1.30, the convective flux will therefore become

$$F_{\rm conv} = \frac{\sqrt{2}}{8}\rho c_P T\sqrt{g\delta}\frac{{\lambda_{\rm MLT}}^2}{H_P^{3/2}}(\nabla_{T,\rm medium} - \nabla_{T,\rm parcel})^{3/2} \tag{1.36}$$

This equation, combined with the expression for the total and radiative flux, leads to a relation between $\nabla_{\rm rad}$, $\nabla_{T,\rm medium}$, and $\nabla_{T,\rm parcel}$

$$\nabla_{\rm rad} = \nabla_{T,\rm medium} + \frac{3}{16\sqrt{2}ac}\frac{c_P\kappa\delta^{1/2}\rho^{5/2}g{\lambda_{\rm MLT}}^2}{P^{1/2}T^3}(\nabla_{T,\rm medium} - \nabla_{T,\rm parcel})^{3/2} \tag{1.37}$$

that can be simplified, defining the **convective effiency** $\Gamma$ (.i.e the ratio between the excess of energy of a parcel before dissolving in the medium and the energy lost during its motion):

$$\Gamma = \frac{3}{4ac}\frac{c_P\kappa\rho^2}{T^3}\bar{v}\frac{V}{A} = \frac{1}{12\sqrt{2}ac}\frac{c_P\kappa\delta^{1/2}\rho^{5/2}g{\lambda_{\rm MLT}}^2}{P^{1/2}T^3}(\nabla_{T,\rm medium} - \nabla_{T,\rm parcel})^{1/2} \tag{1.38}$$

where $V/A$ is the ratio between volume and surface of the parcel and is equal to $2/9\lambda_{\rm MLT}$. Equation 1.37 will therefore become:

$$\nabla_{\rm rad} = \nabla_{T,\rm medium} + \frac{9}{4}\Gamma(\nabla_{T,\rm medium} - \nabla_{T,\rm parcel}) \tag{1.39}$$

or

$$\Gamma = \frac{9}{4}\frac{\nabla_{\rm rad} - \nabla_{T,\rm medium}}{\nabla_{T,\rm medium} - \nabla_{T,\rm parcel}} \tag{1.40}$$

It is obvious that we need estimate $\nabla_{T,\rm parcel}$, in order to determine $\nabla_{T,\rm medium}$, which is the actual $\nabla_T$ of the star. This gradient is related to the adiabatic gradient and

the convection efficiency by the equation:

$$\frac{\Gamma}{1-\eta} = \frac{\nabla_{T,\text{medium}} - \nabla_{T,\text{parcel}}}{\nabla_{T,\text{parcel}} - \nabla_{\text{ad}}} \tag{1.41}$$

where $\eta$ is a corrective factor that consider the of energy production in the parcel. Since we are interested in the external regions of the stars, where no relevant energy production is present, $\eta$ can be considered negligible. Combining equations 1.40 and 1.41 together, is possible to estimate the gradient of temperature in any situation. For the extreme cases, we can find again:

- for an high convection efficiency $\Gamma \to \infty$, $\nabla_{T,\text{medium}} = \nabla_{T,\text{parcel}} \to \nabla_{\text{ad}}$.
- for a low convection efficiency $\Gamma \to 0$, $\nabla_{T,\text{medium}} = \nabla_{T,\text{parcel}} \to \nabla_{\text{rad}}$.

## 1.3 Energy Sources

Together with the mechanical equilibrium, the thermal equilibrium is also necessary to guarantee the stationary state of stars. Since a gradient of temperature is always present in the stellar interiors (except in particular situations), it is therefore known from the previous section that an energy flux is established. Given an element of mass with volume $V$ and surface area $A$, the thermal equilibrium in stars states that the energy is radiated at its surface at the same rate at which is produced or transported in its interior:

$$\oint_A \boldsymbol{F} \cdot \mathrm{d}\boldsymbol{A} = \int_V \rho\epsilon \mathrm{d}V, \tag{1.42}$$

where $\epsilon$ represents the total energy generation rate per second per gram in the volume $\mathrm{d}V$.
Applying the divergence theorem, we have:

$$\boldsymbol{\nabla} \cdot \boldsymbol{F} = \rho\epsilon. \tag{1.43}$$

For a spherical symmetric star, eq. 1.43 becomes:

$$\frac{1}{r^2}\frac{\mathrm{d}}{\mathrm{d}r}\left(r^2 F(r)\right) = \rho\epsilon, \tag{1.44}$$

that can be written in terms of luminosity gradient ($L(r) = 4\pi r^2 F(r)$):

$$\frac{\mathrm{d}L(r)}{\mathrm{d}r} = 4\pi r^2 \rho\epsilon. \tag{1.45}$$

The main sources of energy that occur in stars are:

- **Nuclear Energy** ($\epsilon_{\rm nuc}$)
- **Gravitational Energy** ($\epsilon_{\rm grav}$)
- **Energy loss by neutrinos** ($\epsilon_{\nu}$)

Each of them gives a contribution to the overall energy generation rate $\epsilon$:

$$\epsilon = \epsilon_{\rm nuc} + \epsilon_{\rm grav} - \epsilon_{\nu} \tag{1.46}$$

### 1.3.1 Nuclear Energy

The internal thermal conditions of stars allow nuclear reactions to take place.Nuclear reactions are divided in two categories: reactions that generate significant amounts of energy to impact on the stellar evolutionary timescales, and the reactions important mainly for the synthesis of new elements.
A nuclear burning consists in one or many reactions that belong to the two categories. In LMS and IMS we can identify two major burning events (the hydrogen and the helium burning), that, as we will see, are confined in stellar cores or in shells, depending on the evolutionary stage.

#### Hydrogen burning

Hydrogen burning is present for the entire life of a LMS and IMS star, with the only exception of stellar formation phases (pre-main sequence, PMS) and white dwarfs (WD). During the burning, the hydrogen is converted into helium by two main series of reactions: the **proton−proton chain** (*pp*-chain) and the **CNO cycle**.
The *pp*-chain consists in a direct fusion of four protons in a nucleus of helium:

$$\begin{aligned} p + p &\rightarrow {}^2\mathrm{He} \rightarrow {}^2\mathrm{H} + e^+ + \nu_{\rm e} \quad \times 2 \\ p + {}^2\mathrm{H} &\rightarrow {}^3\mathrm{He} + \gamma \quad \times 2 \\ {}^3\mathrm{He} + {}^3\mathrm{He} &\rightarrow {}^4\mathrm{He} + 2p \end{aligned} \tag{1.47}$$

This group of reactions is also indicated by $PP1$, in order to distinguish it from two alternative channels ($PP2$ and $PP3$) that might appear when a considerable amount of helium is present in the medium. Nevertheless, the relative efficiency of the three *pp*-chains changes with increasing temperature from $PP1$ to $PP3$.

The CNO cycle, instead, uses C, N, and O as catalysts to burn four protons into He (indirect channel). The cycle consists in several reactions that destroy and recreate the catalyst elements. The main cycle of this nuclear burning (CNO-I) is:

$$\begin{aligned} {}^{12}\mathrm{C} + p &\rightarrow {}^{13}\mathrm{N} + \gamma \\ {}^{13}\mathrm{N} &\rightarrow {}^{13}\mathrm{C} + e^{+} + \nu_{\mathrm{e}} \\ {}^{13}\mathrm{C} + p &\rightarrow {}^{14}\mathrm{N} + \gamma \\ {}^{14}\mathrm{N} + p &\rightarrow {}^{15}\mathrm{O} + \gamma \\ {}^{15}\mathrm{O} &\rightarrow {}^{15}\mathrm{N} + e^{+} + \nu_{\mathrm{e}} \\ {}^{15}\mathrm{N} + p &\rightarrow {}^{12}\mathrm{C} + {}^{4}\mathrm{He} \end{aligned} \tag{1.48}$$

During the burning the overall abundance of the heavy elements involved remains unchanged, however the single element abundances reach asymptotic values, according to the relative efficiencies of the reactions. In addition to the main cycle, there are additional branches of reactions connected to it. Moreover, the CNO cycle can start from any reaction.

Once we compare the two nuclear burnings, we can see that the *pp*-chain is dominant in a range of temperature $\sim 0.6-1.5\cdot10^7$ K, while the CNO cycles start to be efficient at $T > 2 \cdot 10^7$ K.

In terms of energy generation rates, the two main H-burning processes are proportional to:

$$\epsilon_{\mathrm{pp}} \propto \rho X_{^1\mathrm{H}}^2 T^4, \tag{1.49}$$

$$\epsilon_{\mathrm{CNO}} \propto \rho X_{^1\mathrm{H}} X_{^{12}\mathrm{C}} T^{18}, \tag{1.50}$$

where $X_{^1\mathrm{H}}$ and $X_{^{12}\mathrm{C}}$ are respectively the mass fraction of hydrogen and $^{12}$C. In the stars where CNO cycle is dominant, $\epsilon_{\mathrm{nuc}}$ is so high that the energy transport by radiation alone is not able to transport all the energy (like in the *pp*-chain), and core-convection sets in.

### Helium burning

Helium burning takes place in the later phases of the LMS and IMS evolution (as well as in massive stars), in particular during the helium-core-burning (HeCB) and the asymptotic giant branch phase (AGB). It consists of two main reactions chains: the **triple-alpha reaction** (Eq.1.51) and carbon-to-oxygen reaction ($^{12}\mathbf{C}(\alpha,\gamma)^{16}\mathbf{O}$).

The triple-alpha reaction converts three nuclei of $^4$He (i.e. $\alpha$ particles) in $^{12}$C:

$$\begin{aligned} {}^4\mathrm{He} + {}^4\mathrm{He} &\rightarrow {}^8\mathrm{Be} \\ {}^8\mathrm{Be} + {}^4\mathrm{He} &\rightarrow {}^{12}\mathrm{C}^* \rightarrow {}^{12}\mathrm{C} + 2\gamma \end{aligned} \tag{1.51}$$

$^{12}$C($\alpha$,$\gamma$)$^{16}$O, instead consists in an $\alpha$-capture by a nucleus of $^{12}$C:

$$^{12}\mathrm{C} + {}^4\mathrm{He} \rightarrow {}^{16}\mathrm{O} + \gamma$$

These two reactions may act simultaneously with an efficiency that depends on the evolutionary phase of the star. The helium burning starts to be efficient at temperatures higher than $10^8$ K, and the energy generation rates (especially the triple-$\alpha$) have an extremely high dependence on temperature :

$$\epsilon_{3\alpha} \propto \rho^2 X_{^4\mathrm{He}}^3 T^{40} \tag{1.52}$$

$$\epsilon_{^{12}\mathrm{C}(\alpha,\gamma)^{16}\mathrm{O}} \propto \rho X_{^4\mathrm{He}} X_{^{12}\mathrm{C}} T^{20}. \tag{1.53}$$

This is the reason why the core where helium burning takes place is very compact and convective.

## 1.4 Evolutionary Phases

During its life, a star evolves through several stages, in which the internal structure changes. The evolution can be followed on different diagrams. For example, the **Hertzsprung-Russell diagram** (HRD) describes how the surface luminosity ($L$) and the effective temperature $T_{\mathrm{eff}}$ vary with age (figure 1.1), while the **Kippenhahn diagram** shows schematically the evolution of the internal structure with age (figure 1.2).
In the following paragraphs I will give an overview of the evolutionary stages that Low- and Intermediate-Mass Stars undergo.

### 1.4.1 Main Sequence

Stars spend most of their life in the **Main Sequence** (MS, figure 1.3). During the Main Sequence, the hydrogen burning provides the nuclear energy necessary to maintain the stability of the star. In stars where the CNO cycle is the main burning channel, the core tend to become convective, since the radiation is not sufficient to

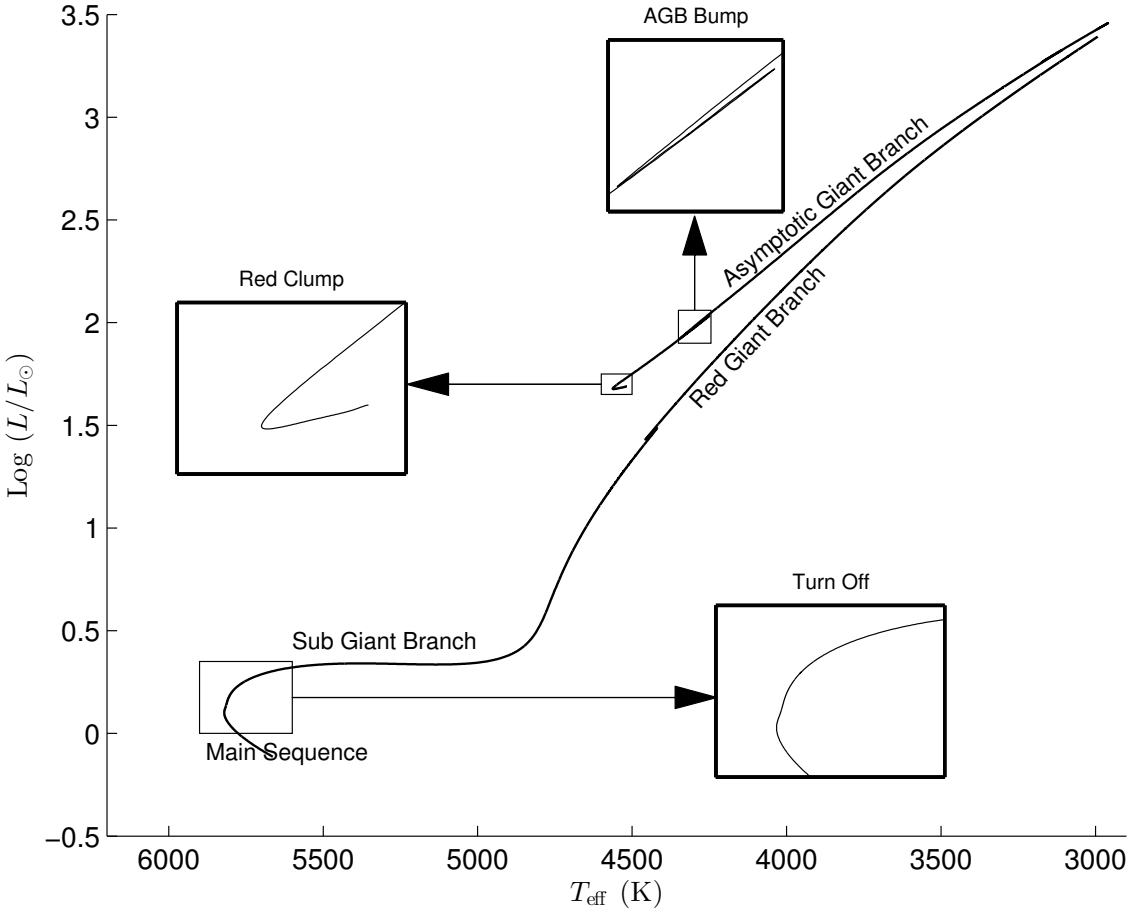


**Figure 1.1:** Evolutionary track of 1 $M_\odot$ star with solar chemical composition on the Hertzsprung-Russell diagram from the Main Sequence to the first thermal pulse on the Asymptotic Giant Brunch. The model is computed using the publicly available stellar evolution code MESA, Paxton et al. 2011, 2013, 2015

carry outward the energy produced by the nuclear reactions. On the contrary, stars where *pp*-chain is the dominant nuclear burning develop a radiative core.
As I previously mentioned in section 1.3, the factor that mostly influences the efficiency of the nuclear burning is the temperature, which, in turn, has a strong dependence on the initial mass of the star. The transition between the two H-burning channels is located in the LMS interval, in particular stars with masses around $1.2 - 1.3$ $M_\odot$ start to develop CNO-burning convective cores, whose size increases with the stellar mass. Stars with masses higher than $1.2 - 1.3$ $M_\odot$, however, still have a radiative region above the mixed core where *pp*-chain dominates.

### 1.4.2 Sub Giant Branch

Once the hydrogen in the core is depleted, the nuclear reactions in the centre stop. The star leaves the MS and continues its evolution along the **Sub Giant Branch**

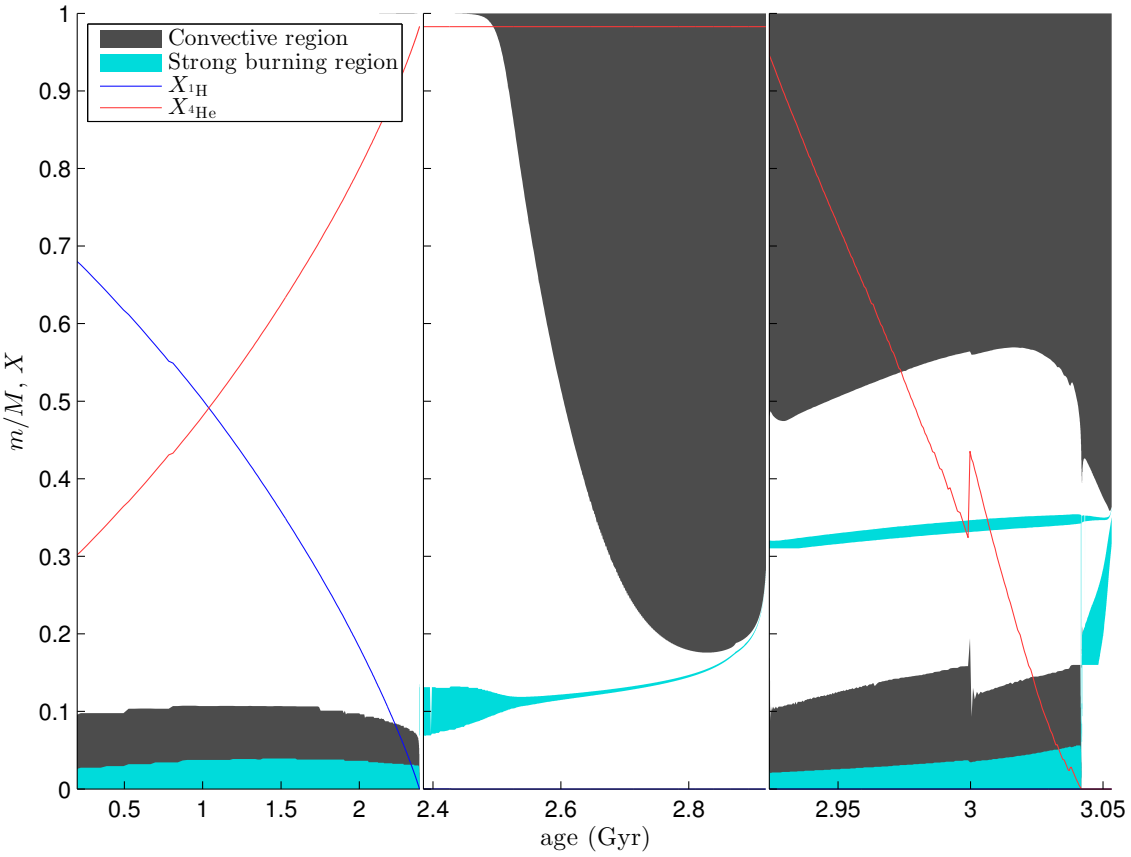


**Figure 1.2:** Kippenhahn diagram. The graph shows the internal evolution of a star of 1.5 $M_\odot$ with solar chemical composition from the Main Sequence to the first thermal pulse on the Asymptotic Giant Brunch. The grey regions corresponds to the zones of the star affected by convection, the blue regions are instead the zones where a strong nuclear burning is active, while the two solid lines represent the mass fractions of hydrogen (blue) and helium (red). The model is computed using MESA, Paxton et al. 2011, 2013, 2015.

(SGB, figure 1.4).

Without the nuclear reactions, the core, mainly made of helium, contracts and becomes more and more hot and dense. As a result, the layers immediately above the core rise their temperature too and ignite hydrogen nuclear reactions in a thick shell surrounding the core. The burning shell becomes thinner and thinner, converting hydrogen by the CNO-cycle channel into helium, which is deposited on the core in contraction. In the meantime, the envelope reacts to the contraction expanding and cooling down. The external convection slowly penetrates deep in the interior of the star (figure 1.2), bringing the products of the nuclear reactions to the surface (**first dredge-up**). During the process, the star maintains an almost constant luminosity, while the effective temperature decreases. As consequence, the total radius increases,

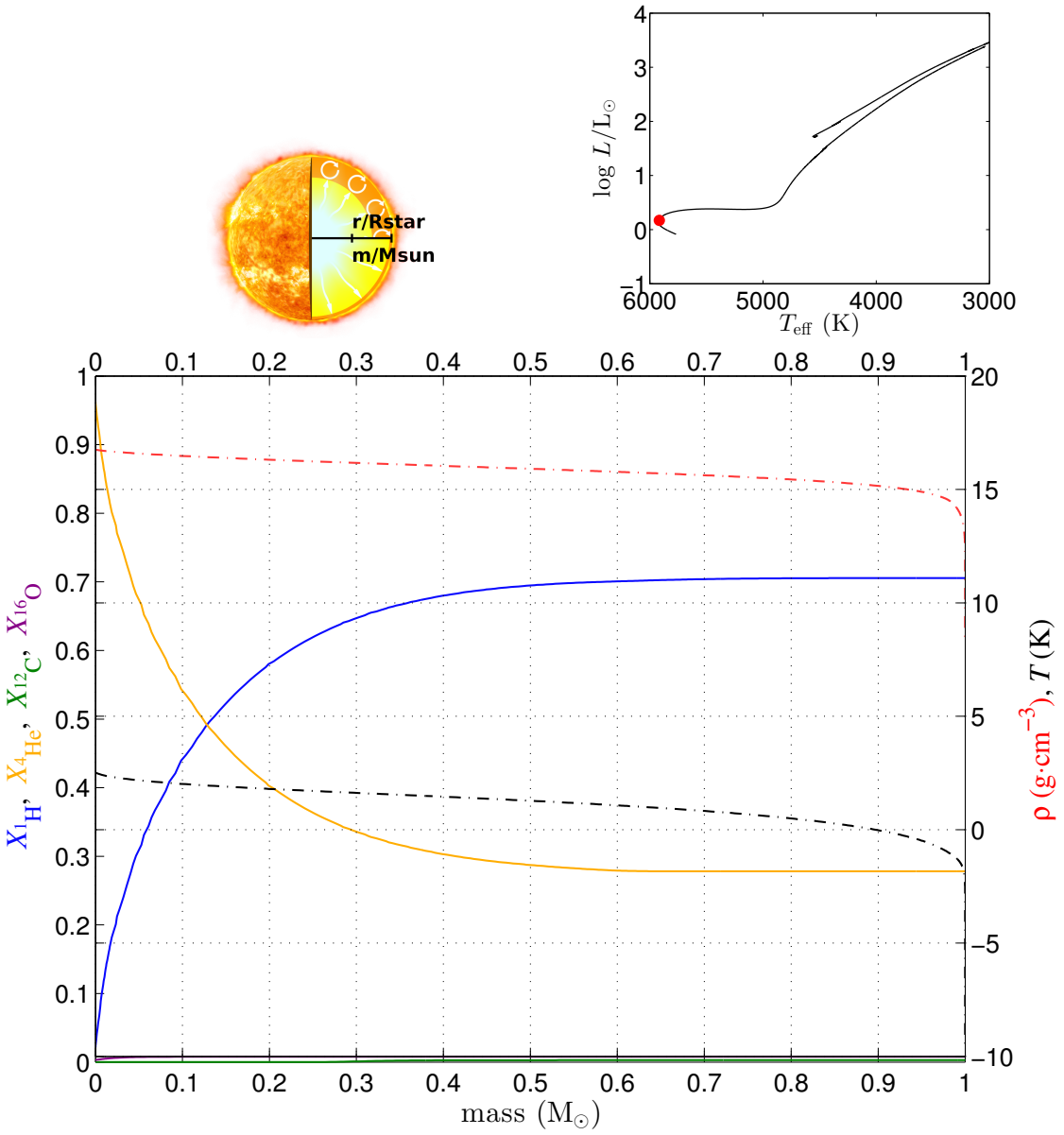


**Figure 1.3:** Typical internal structure of a 1 $M_\odot$ star during the main sequence. The red dot indicates the location on the HR diagram. The solid lines corresponds to the mass faction in function of the mass coordinate of hydrogen (blue), helium (yellow), carbon (green), and oxygen(purple). The dashed lines are respectively the density (red) and the temperature (black) profile.

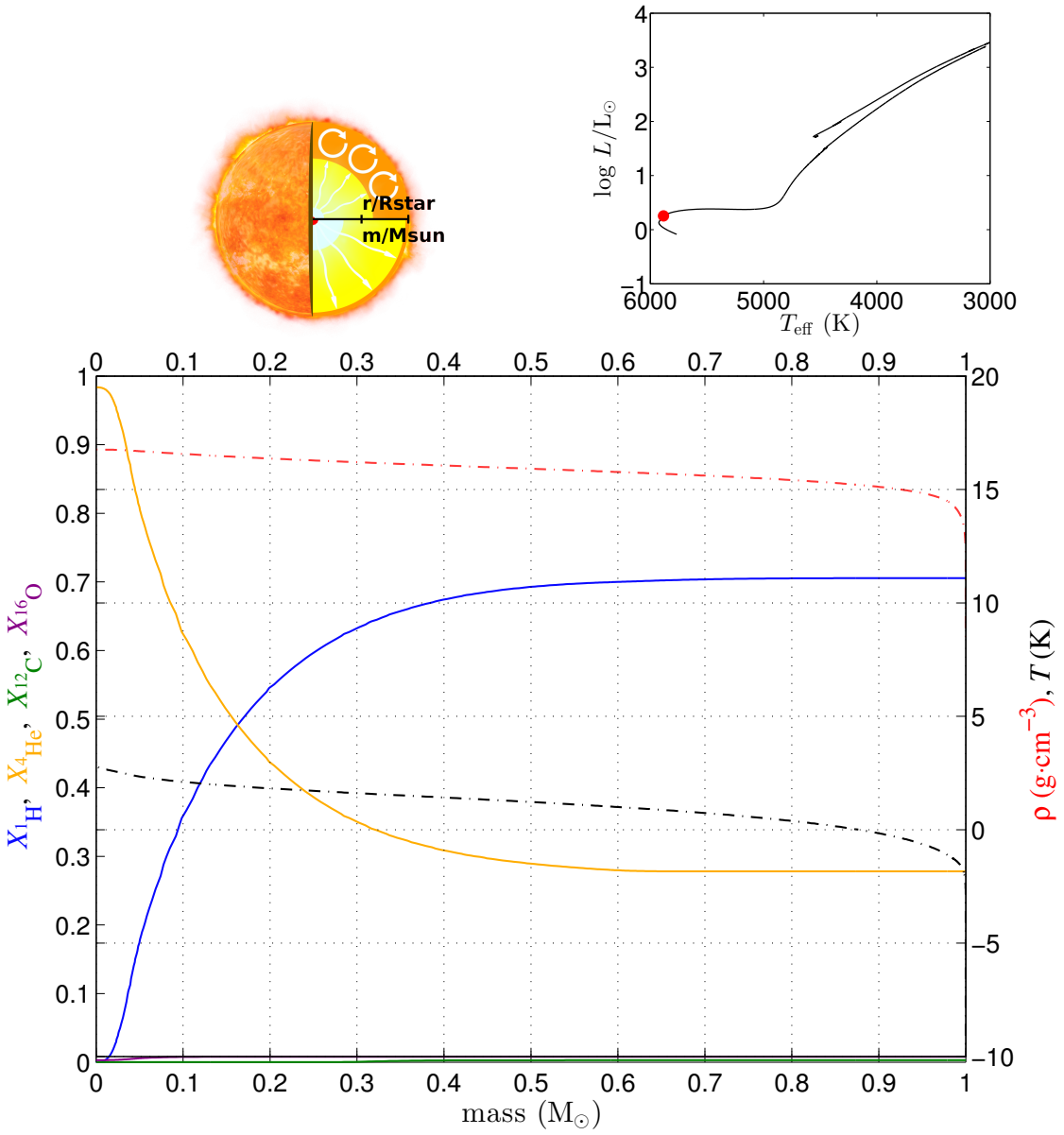


**Figure 1.4:** Typical internal structure of a 1 $M_\odot$ star in the sub-giant branch phase. The red dot indicates the location on the HR diagram. The solid lines corresponds to the mass faction in function of the mass coordinate of hydrogen (blue), helium (yellow), carbon (green), and oxygen(purple). The dashed lines are respectively the density (red) and the temperature (black) profile.

since $L$ and $T_{\rm eff}$ are related by the black body equation:

$$L = 4\pi\sigma R^2 {T_{\rm eff}}^4. \tag{1.54}$$

**Schönberg-Chandrasekhar limit**

With the exhaustion of hydrogen in the core and the end of nuclear reactions, the luminosity in the centre goes to zero as well as the gradient of temperature. Depending on the initial mass, stars can develop an isothermal core in a non-$e^-$-degenerate regime. For such stars the hydrostatic equilibrium persists until the mass of the helium core, in constant growth, exceeds the limit of Schönberg-Chandrasekhar (Schönberg & Chandrasekhar, 1942):

$$M_{\rm SC} = M \cdot 0.37 \left(\frac{\mu_{\rm env}}{\mu_{\rm core}}\right)^2, \tag{1.55}$$

where $\mu_{\rm env}$ and $\mu_{\rm core}$ are respectively the mean molecular weight of the envelope and the core. For a core mass larger than $M_{\rm SC}$, the electron gas in core starts to become degenerate.

### 1.4.3 Red Giant Branch

Continuing along its evolution, the star then approaches the *Hayashi limit*, an almost vertical line in the HRD where fully convective objects are in hydrostatic equilibrium. Almost the entire envelope is convective and the H-burning shell is now thin. The core is still in contraction but $T_{\rm eff}$ cannot decrease any longer, since no stars in hydrostatic equilibrium can exist at $T_{\rm eff}$ cooler than the Hayashi limit. Therefore the only possibility to expand the envelope is to increase the luminosity: the **Red Giant Branch** (RGB) begins (figure 1.5). The electron component of the gas gradually becomes fully degenerate and creates a strong pressure able to contrast the gravity and slows down the contraction:

$$P_{\rm e} \propto \rho^{5/3}. \tag{1.56}$$

The total pressure is formed now of two components: the pressure of the electrons $P_{\rm e}$ (Eq.1.56) and the pressure of the nuclei of helium which are still in a perfect gas condition:

$$P = P_{\rm e} + P_{\rm nuclei} = K\rho^{5/3} + \frac{k_{\rm B}\rho T}{m_{\rm u}\mu} \tag{1.57}$$

$\mu$ is the molecular weight.

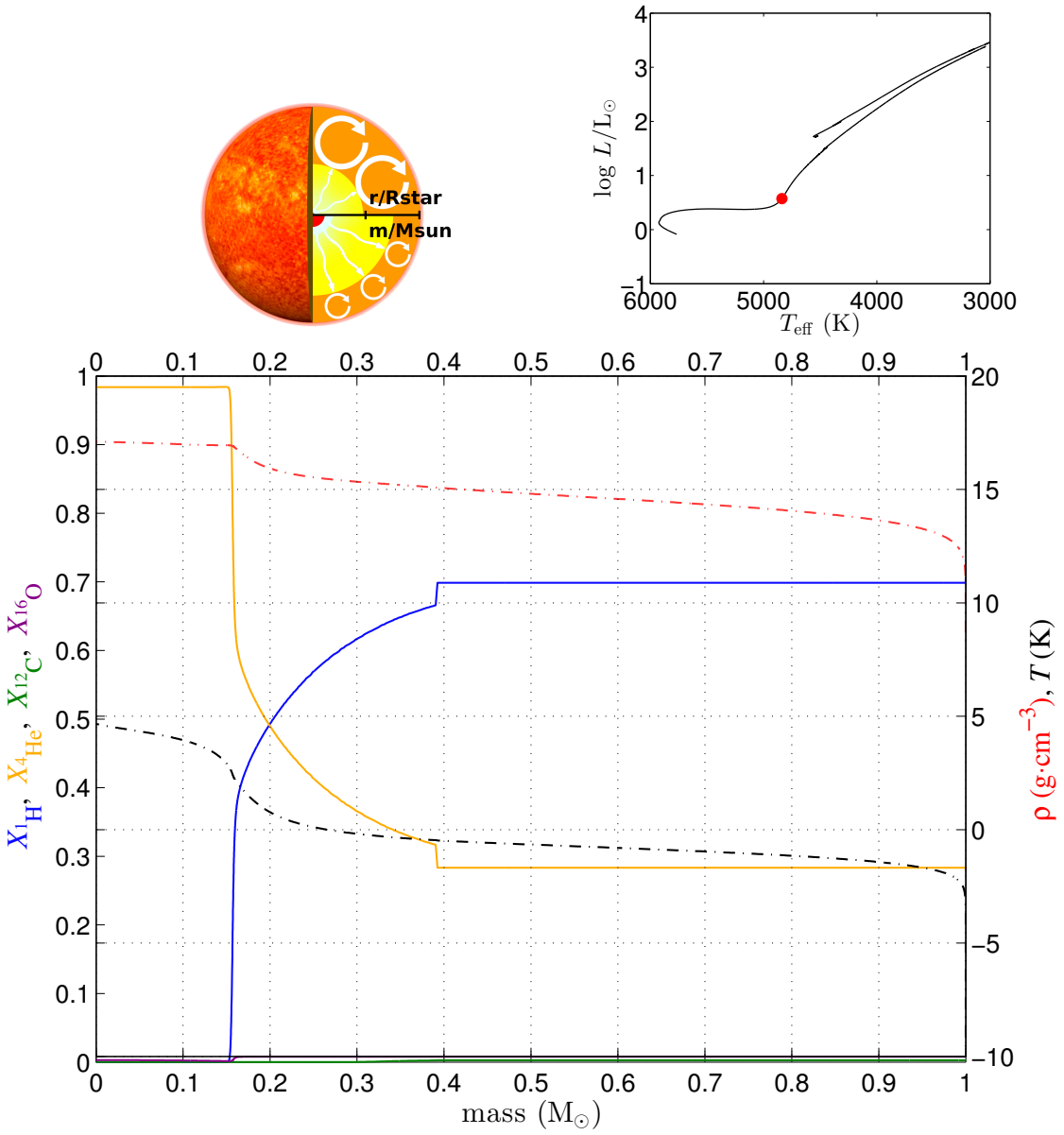


**Figure 1.5:** Typical internal structure of a 1 $M_\odot$ star at the bottom of the RGB. The red dot indicates the location on the HR diagram. The solid lines corresponds to the mass faction in function of the mass coordinate of hydrogen (blue), helium (yellow), carbon (green), and oxygen(purple). The dashed lines are respectively the density (red) and the temperature (black) profile.

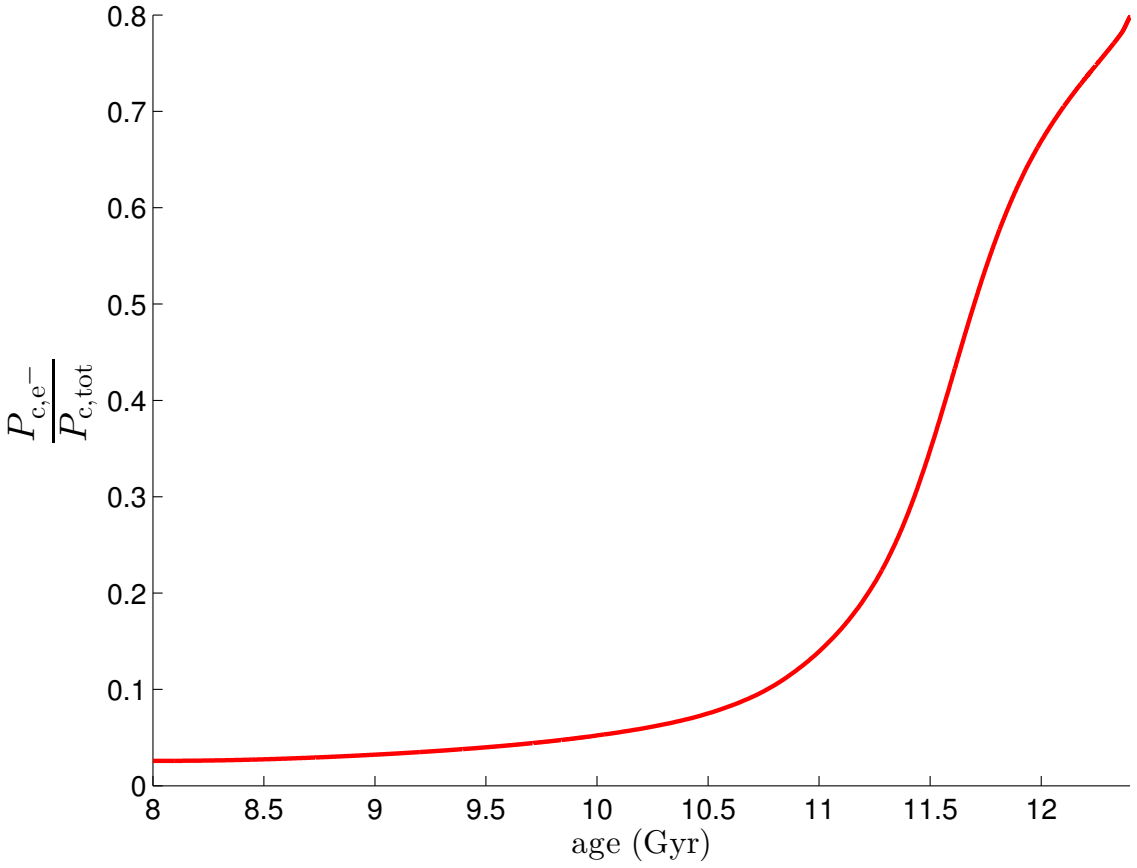


**Figure 1.6:** Central pressure of the electrons $P_{c,e^-}$ over total central pressure star in function of age for a 1 $M_\odot$ between the end of the Main Sequence and the top of the RGB. $P_{c,e^-}$ grows with the age and dominates the total pressure since the electron gas becomes more and more degenerate and the centre density rises. The Model is computed with MESA (Paxton et al., 2011)

The pressure of the perfect gas component is negligible with respect to the degenerate component, hence the central temperature does not affect the total pressure but depends only on the density (Figure 1.6).

Since the H-burning shell is active, new helium is produced and deposited on the surface of the core, which grows in mass and becomes more and more hot and dense (figure 1.7). The H-burning shell is also responsible for the surface luminosity. It can be shown that luminosity and core mass are connected by homology relations, $L \propto M^{8-10}$. Low-mass stars ascend the RGB until the overall mass of the helium core reaches the critical value $M_{\mathrm{HeF}} = 0.45 - 0.55 M_\odot$. Once $M_{\mathrm{HeF}}$ is reached, the star experiences the helium flash which lifts the electron degeneracy and starts the helium-core-burning phase (section 1.4.4)

In the case of VLMS, this situation cannot happen since the overall mass is lower than the critical value. VLMS are the prototypes of helium white dwarfs. On the other hand, IMS (and higher masses) reach the temperature needed for He ignition

before they experience high degeneracy. Therefore IMS develop an helium core with mass smaller than $M_{\rm HeF}$.

#### RGB bump

During their ascent on the RGB, the H-burning shell crosses the chemical discontinuity left by the first dredge-up. In low-mass stars this event generates the **RGB-bump** (RGBb). The monotonic increase of luminosity is abruptly interrupted since the molecular weight $\mu$ in H-shell decreases. In fact, the homology relation shows that $L \sim \mu^7$. Once the H-burning shell has passed the discontinuity, the luminosity rises again. Observationally speaking, the bump produces an accumulation of stars that is easily visible as a peak in the luminosity function of globular and open clusters.

### 1.4.4 Helium Flash

As already anticipated in section 1.4.3, low-mass stars need to grow their helium core to the mass of $M_{\rm HeF}$(figure 1.8) in order to reach temperatures necessary to ignite the helium nuclear reactions. Due to the energy release by He-burning reactions, the temperature in the core increases further. However, the pressure is dominated by the electron-degenerate component, therefore the gas can not expand and cool down. Since the temperature and the nuclear energy production are strongly related, a *thermal runaway* occurs. When the temperature becomes high enough, the perfect gas component of the total pressure (eq.1.57) is no longer negligible and the gas is free to expand and cool down, removing the degeneracy. The entire process is called **helium Flash** (HeF). The critical mass $M_{\rm HeF}$ is independent from the initial mass of the star and has a slight dependence on metallicity. However, stars with mass higher than $1.8 - 2.2$ $\rm M_\odot$(high and intermediate-mass stars) reach the temperature needed to ignite helium nuclear reactions before the electrons are fully degenerate. Stars with mass lower than $0.45 - 0.55$ $\rm M_\odot$(very low-mass stars) have not enough material to form cores with mass equal to $M_{\rm HeF}$ and they evolve into helium white dwarfs.

### 1.4.5 Helium-Core Burning

Once the helium-core-burning is set up, the star has a different structure and global properties with respect to the RGB phase. From the surface to the centre, the internal structure consists of a large convective envelope, a H-burning shell and a

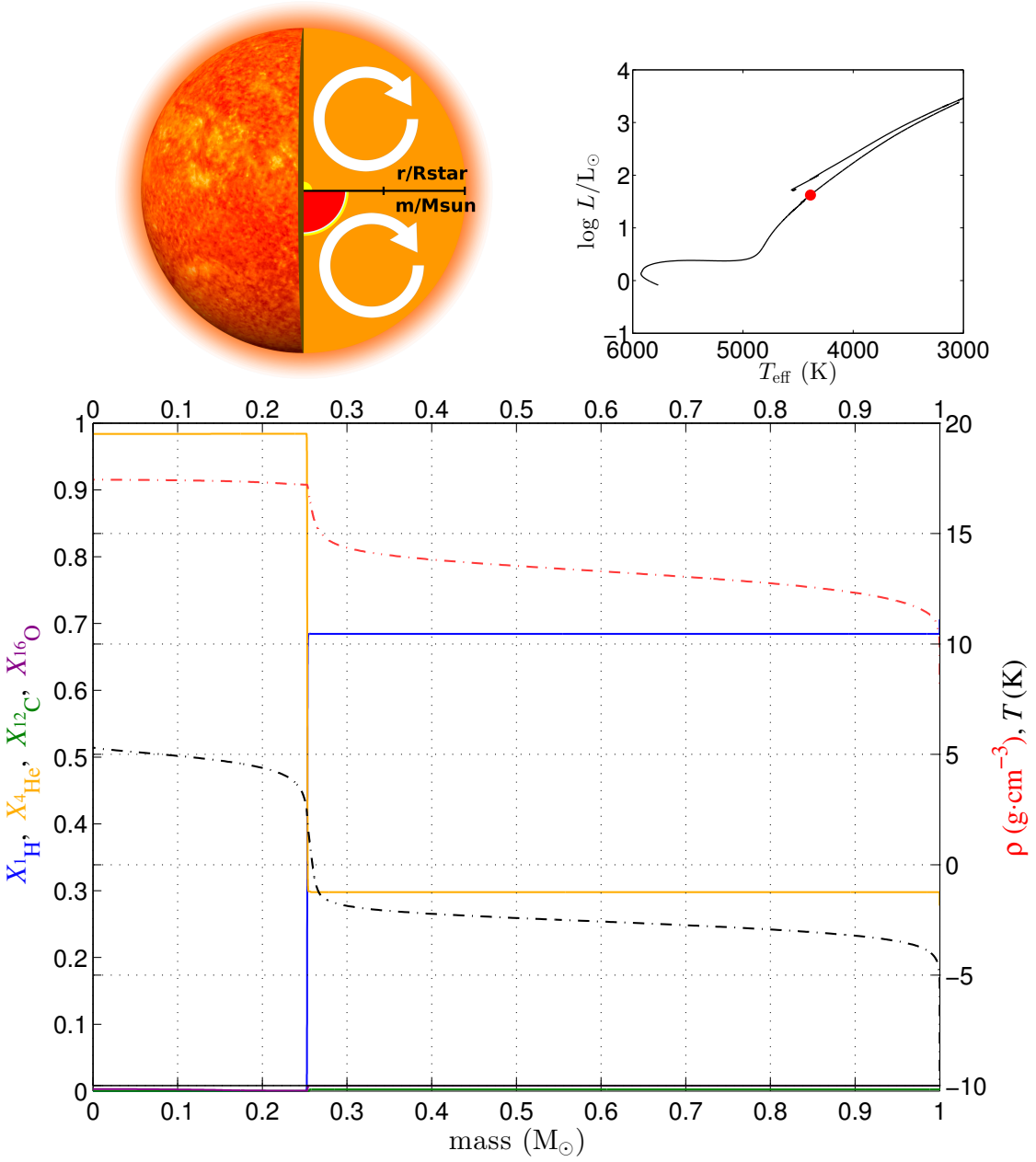


**Figure 1.7:** Typical internal structure of a 1 $M_\odot$ star during the RGB. The red dot indicates the location on the HR diagram. The solid lines corresponds to the mass faction in function of the mass coordinate of hydrogen (blue), helium (yellow), carbon (green), and oxygen(purple). The dashed lines are respectively the density (red) and the temperature (black) profile.

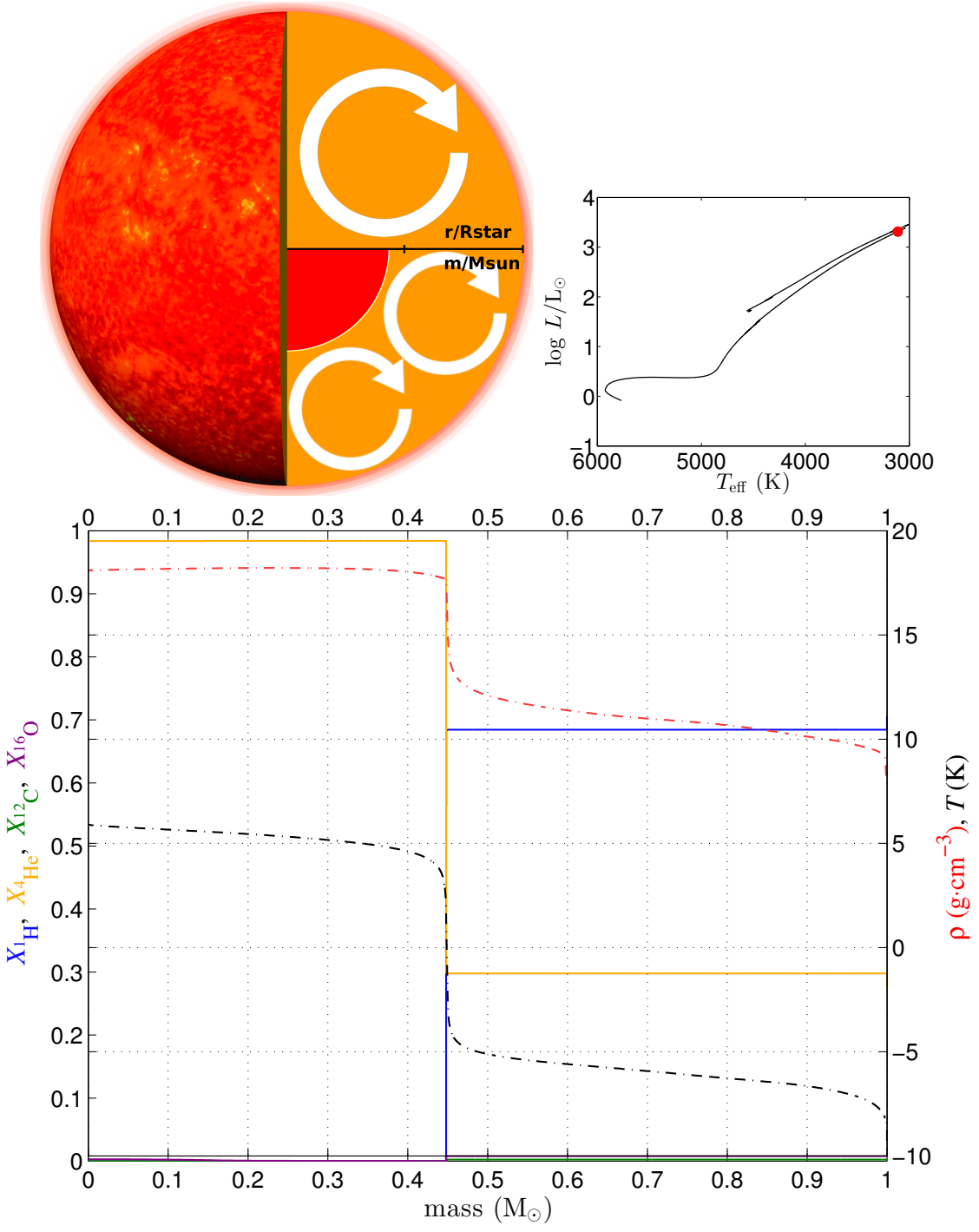


**Figure 1.8:** Typical internal structure of a 1 $M_\odot$ star at the tip of the RGB. The red dot indicates the location on the HR diagram. The solid lines corresponds to the mass faction in function of the mass coordinate of hydrogen (blue), helium (yellow), carbon (green), and oxygen(purple). The dashed lines are respectively the density (red) and the temperature (black) profile.

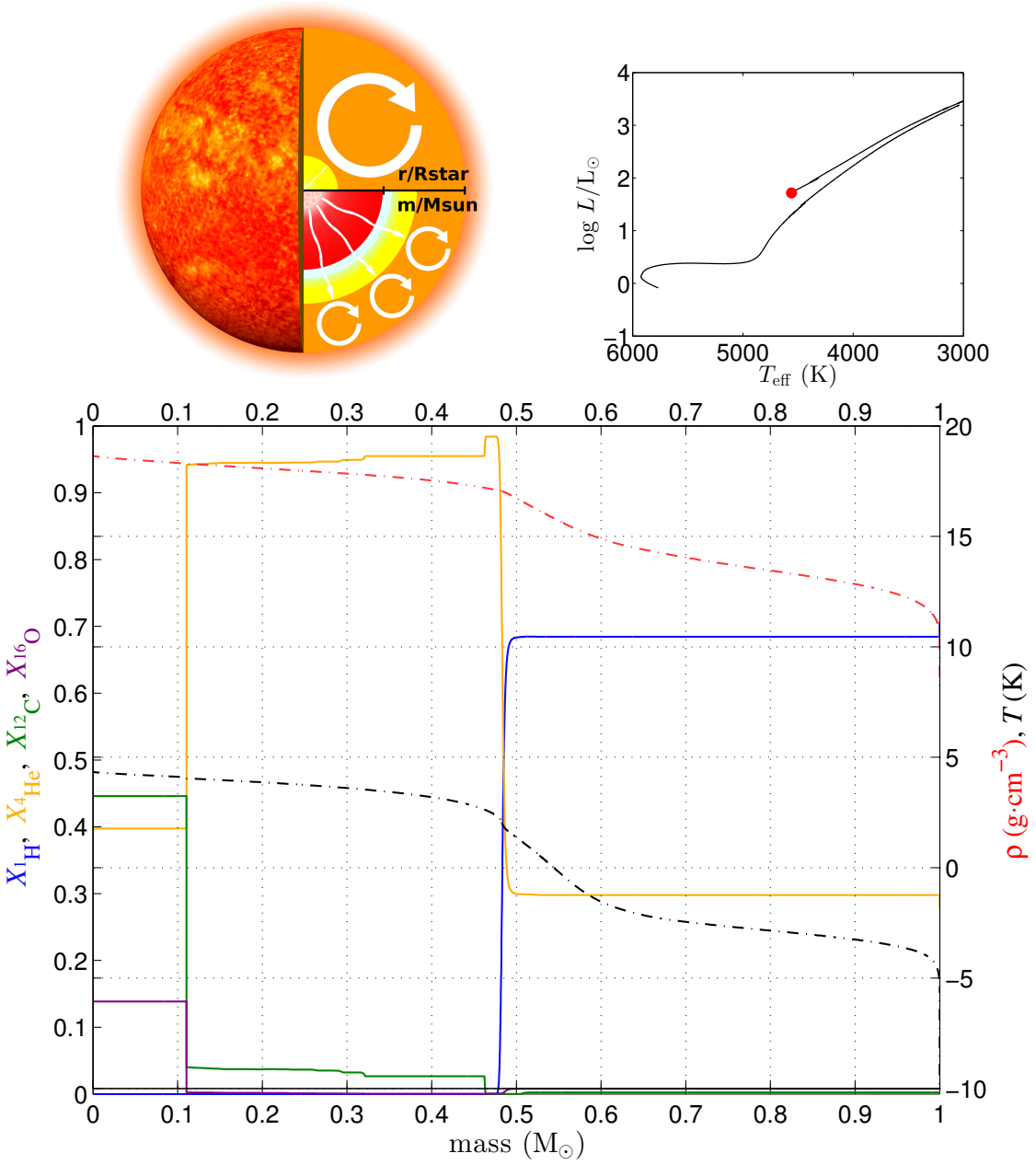


**Figure 1.9:** Typical internal structure of a 1 $M_\odot$ He-core-burning star. The red dot indicates the location on the HR diagram. The solid lines corresponds to the mass faction in function of the mass coordinate of hydrogen (blue), helium (yellow), carbon (green), and oxygen(purple). The dashed lines are respectively the density (red) and the temperature (black) profile.

region composed of a plasma composed primarily of helium (figure 1.9). At the center two nuclear reactions are present simultaneously: the triple-alpha reaction and carbon into oxygen reaction. Given the high dependence on the temperature of helium-burning reactions, nuclear energy generation is confined inside a very compact and convective core.
Due to the central convection, the helium core is chemically homogeneous. Therefore, since the core grows, a chemical discontinuity at the convective border develops, and becomes more and more pronounced as He-burning proceeds (the situation changes depending on the mixing prescription adopted to define the convective boundaries, see chapter 4.2).
At the beginning of the helium burning phase, the tri-alpha reactions dominate until the mass fraction of helium in the core drops under $\sim 0.2$ (Straniero et al., 2003). Then, the energy production by the $^{12}C(\alpha,\gamma)^{16}O$ reactions becomes greater than that by the triple-$\alpha$ reactions. The entire helium core becomes more compact, the H-burning shell increases its energy generation rate and the total luminosity rises.

### 1.4.6 Asymptotic Giant Branch

With the exhaustion of helium in the core, He-burning stops hence the central convective region rapidly recedes and disappears. The luminosity in the centre goes to zero as well as the gradient of temperature, therefore the core becomes almost isothermal. The star approaches again the Hayashi limit and its luminosity starts to increase, climbing the **Asymptotic Giant Branch** (AGB). The core contracts again and, analogously to the H-burning in the SGB, the He-burning ignites in a shell. The nuclear burning in the He-shell is not convective, thus the He-burning shell moves outward as the helium abundance decreases, leaving behind the products of the nuclear reactions, increasing the mass of the C/O core, and bringing the He-shell closer to the H-shell.
During the AGB phase the structure of the star from the centre is (Figure 1.10):

- a core composed primarily of C and O and degenerate electrons,
- a He-burning shell,
- a H-burning shell,
- and a deep convective envelope.

In low-mass stars, the overall mass is not enough to reach the temperature of the carbon nuclear reaction, thus the star continues to increase its luminosity until

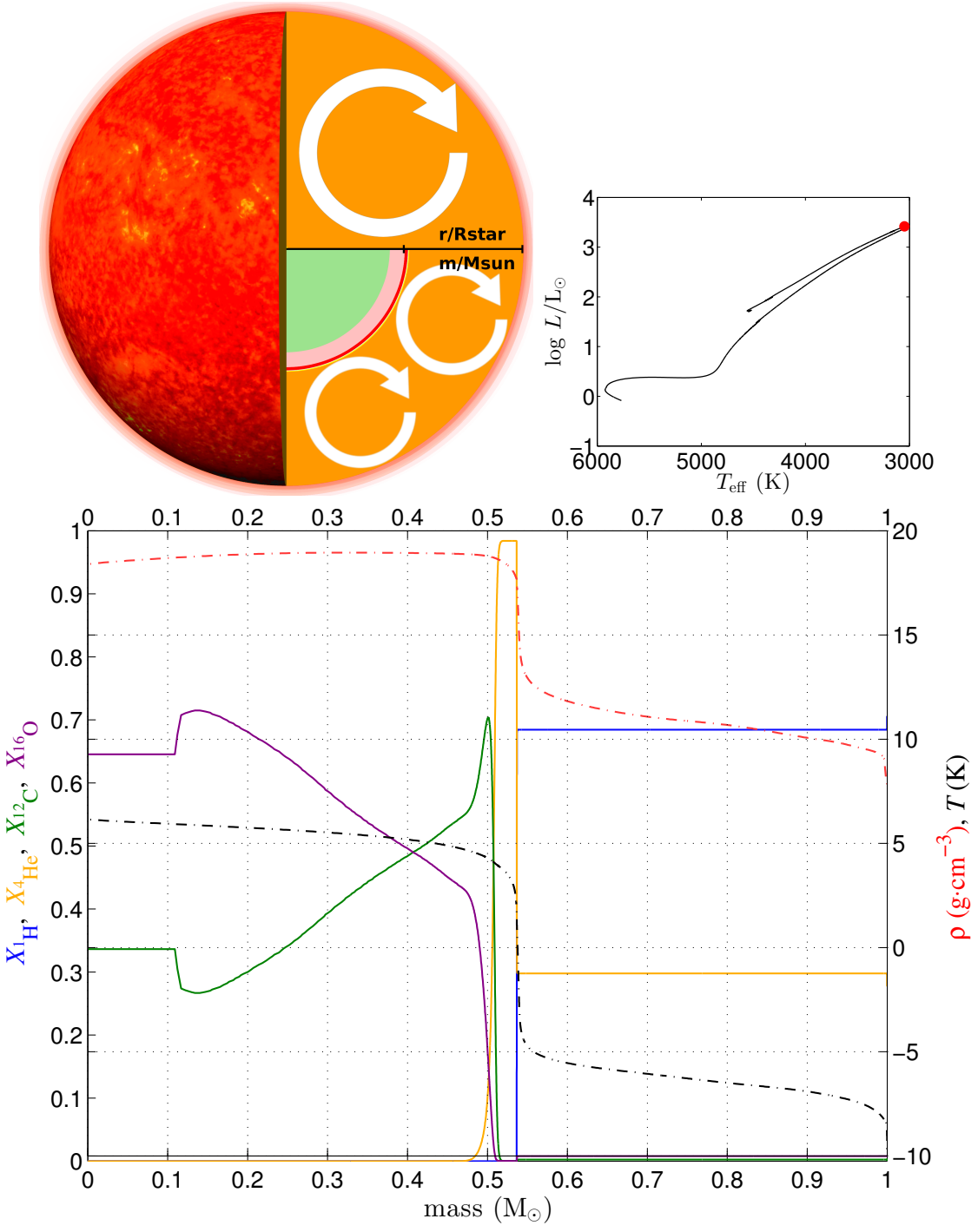


**Figure 1.10:** Typical internal structure of a 1 $M_\odot$star at the first thermal pulse. The red dot indicates the location on the HR diagram. The solid lines corresponds to the mass faction in function of the mass coordinate of hydrogen (blue), helium (yellow), carbon (green), and oxygen(purple). The dashed lines are respectively the density (red) and the temperature (black) profile.

$L \simeq 10^4 L_\odot$. At the end of the AGB phase the two shells are very close together and start to experience periodic thermal instabilities, called **Thermal Pulses**. The base of the envelope becomes unstable and detaches from the star forming the *Planetary Nebula* (PN). The remnant is a compact object made mainly of carbon and oxygen in high electron degeneracy called *White Dwarf* (WD).

### AGB bump

On the HRD the formation of the He-burning shell corresponds to the **AGB bump** (AGBb). Similarly to the RGB bump, it consists in a decrease followed by an increase of the total luminosity. The reason behind the AGBb must be searched immediately after the end of the Helium-core-burning. Without any nuclear energy production in the centre, the entire stellar structure reacts in order to compensate the loss of this energy source. Outside the border of the former convective core, the energy generation rate from He-burning reactions rises in a shell, mainly due to the larger helium abundance relative to the inner zone (the discontinuity) and the temperature profile. First, the total luminosity and the H-shell-burning luminosity drops, while the He shell provides a higher and higher fraction of $L$. At some point the He-burning-shell replaces the H-burning-shell as the main source of nuclear energy. Therefore the total luminosity starts to grow again while the H-burning shell decreases its energy production, since it has expanded and cooled down due to the ignition of a second burning shell.

# Chapter 2

# Theory of Oscillation in Stars

Asteroseismology is a branch of stellar astrophysics specialised in the detection and interpretation global oscillations that can be observed at the surface of stars. Oscillations in single stars are excited by two main mechanisms (Aerts, Christensen-Dalsgaard & Kurtz, 2010):

- **Self-exited oscillations** (e.g. $\kappa$-mechanism);
- **Stochastic oscillations** (excited by external convective layers).

While the the former are unstable oscillations, typical in stars like Cepheids, RR Lyrae, Mira, $\delta$ Scuti, $\beta$ Cephei, and other classical pulsators, the latter are dumped modes which have been investigated for the first time in the Sun (Helioseismology) and they are called **Solar-Like Oscillations**. Solar-like oscillations are present in stars with a $T_{\rm eff}$ low enough to have a superficial convective region, typical, for instance, in low main sequence stars, or in the sub-giant and in the red-giant stars. The concepts introduced in sections 2.1-2.4 are mostly based on (Aerts, Christensen-Dalsgaard & Kurtz, 2010) and the Unno et al. (1989) books on stellar oscillations, and gives a brief review of the theory behind oscillations in stars.

## 2.1 Mathematical tools in Spherical Coordinates

To describe oscillations under the condition of spherical symmetry, it is useful to adopt a spherical system of coordinates for the equations. In a three dimensional space, the system of Cartesian coordinates $x, y, z$ can be converted in spherical co-

ordinates $r, \theta, \phi$ through the equations

$$\begin{cases} r = \sqrt{x^2 + y^2 + z^2} \\ \theta = \arccos\left(\dfrac{z}{\sqrt{x^2 + y^2 + z^2}}\right) \\ \phi = \arctan\left(\dfrac{y}{x}\right) \end{cases} \tag{2.1}$$

Assuming the generic scalar and vectorial variables $\varphi$ and $\boldsymbol{\psi}$, the basic mathematical operations of gradient, divergence and the Laplacian become respectively:

$$\nabla\varphi = \frac{\partial\varphi}{\partial r}\boldsymbol{u_r} + \frac{1}{r}\frac{\partial\varphi}{\partial\theta}\boldsymbol{u_\theta} + \frac{1}{r\sin\theta}\frac{\partial\varphi}{\partial\phi}\boldsymbol{u_\phi} \tag{2.2}$$

$$\boldsymbol{\nabla}\cdot\boldsymbol{\psi} = \frac{1}{r^2}\frac{\partial}{\partial r}\left(r^2\psi_r\right) + \frac{1}{r\sin\theta}\frac{\partial}{\partial\theta}\left(\sin\theta\psi_\theta\right) + \frac{1}{r\sin\theta}\frac{\partial\psi_\phi}{\partial\phi} \tag{2.3}$$

$$\boldsymbol{\nabla}\cdot(\nabla\varphi) = \nabla^2\varphi = \frac{1}{r^2}\frac{\partial}{\partial r}\left(r^2\frac{\partial\varphi}{\partial r}\right) + \frac{1}{r^2\sin\theta}\frac{\partial}{\partial\theta}\left(\sin\theta\frac{\partial\varphi}{\partial\theta}\right) + \frac{1}{r^2\sin^2\theta}\frac{\partial^2\varphi}{\partial\phi^2} \tag{2.4}$$

where $\boldsymbol{u_r}$, $\boldsymbol{u_\theta}$, and $\boldsymbol{u_\phi}$ are the unit vectors of the three coordinates $r, \theta, \phi$. If we consider the $\theta$ and $\phi$ coordinates together, we can define the already introduced horizontal (or angular) component $h$ for which is valid:

$$\boldsymbol{\psi}_h = \psi_\theta\boldsymbol{u_\theta} + \psi_\phi\boldsymbol{u_\phi} \tag{2.5}$$

With the notation $\nabla_h$, $\boldsymbol{\nabla_h}\cdot$, and $\nabla_h^2$ are indicated the three differential operations acting only on the horizontal coordinate. The displacement $\boldsymbol{\delta r}$ and the other vectorial quantities can be expressed as sum of the radial and horizontal components.

$$\boldsymbol{\delta r} = \xi_{\mathrm{r}}\boldsymbol{a}_{\mathrm{r}} + \boldsymbol{\xi}_{\mathrm{h}}. \tag{2.6}$$

For instance, the Laplace operator (eq. 2.4) can be written as the sum of a operators $D_r$, that acts only on the radial coordinate, and a operator $L^2$, for the angular part:

$$\nabla^2\varphi = D_r\varphi + \frac{1}{r^2}L^2\varphi \longrightarrow \begin{cases} D_r\varphi = \dfrac{1}{r^2}\dfrac{\partial}{\partial r}\left(r^2\dfrac{\partial\varphi}{\partial r}\right) \\ L^2\varphi = \dfrac{1}{\sin\theta}\dfrac{\partial}{\partial\theta}\left(\sin\theta\dfrac{\partial\varphi}{\partial\theta}\right) + \dfrac{1}{\sin^2\theta}\dfrac{\partial^2\varphi}{\partial\phi^2} \end{cases} \tag{2.7}$$

## 2.2 Adiabatic Oscillations

### 2.2.1 Hydrodynamic equations

In order to present the theory behind stellar oscillations, I need first to introduce the set of hydrodynamic equations that describe an ideal fluid.

#### Equation of continuity

This equation was already introduced in Chapter 1, eq. 1.10, which is here expressed in differential form:

$$\frac{\partial \rho}{\partial t} + \boldsymbol{\nabla} \cdot (\rho \boldsymbol{v}) = 0, \tag{2.8}$$

where $\boldsymbol{v}$ is the time derivative of the position $\boldsymbol{r}$.

#### Equation of motion

The equation of motion in differential form is written as:

$$\rho \left( \frac{\partial}{\partial t} + \boldsymbol{v} \cdot \boldsymbol{\nabla} \right) \boldsymbol{v} = \rho \boldsymbol{f} - \boldsymbol{\nabla} p - \boldsymbol{\nabla} \cdot \boldsymbol{T}_{\mathbf{s}} \tag{2.9}$$

In this equation, $\boldsymbol{f}$ represents the body force per unit of mass. Under the condition of a non-rotating non-magnetic star, the only existing force that contrasts the pressure gradient is the gravitational force $\rho g$ (force per unit of volume), whose potential $\Phi$ satisfies the equation

$$\nabla^2 \Phi = 4\pi G \rho \qquad \text{(Poisson's equation)} \tag{2.10}$$

The term $\boldsymbol{T}_{\mathbf{s}}$ is a tensor associated to viscosity. Since we are assuming that the gas is ideal, this term can be ignored (typical situation in stellar conditions).

#### Energy equation

For an ideal fluid the energy conservation states that the rate of energy variation is equal to the total force by unit of time for a given material volume. The equation can be written in the following form:

$$\rho T \left( \frac{\partial}{\partial t} + \boldsymbol{v} \cdot \boldsymbol{\nabla} \right) S = \rho \epsilon - \boldsymbol{\nabla} \cdot \boldsymbol{F}_{\mathrm{rad}}, \tag{2.11}$$

where $S$ is the specific entropy, $\epsilon$ is the energy generation rate and $F_{\mathrm{rad}}$ is the radiative flux (eq. 1.15). In case of no viscosity, no energy dissipation, and assuming

only adiabatic transformations, equation 2.11 is reduced to the equation of entropy conservation:

$$\frac{\partial S}{\partial t} + \boldsymbol{v} \cdot \boldsymbol{\nabla} S = 0. \tag{2.12}$$

This approximation can be justified by the fact that generally timescales for radiative energy transport at each point of a star are several orders of magnitude larger than the typical periods of oscillation, hence the right side of eq. 2.11 becomes negligible (Aerts, Christensen-Dalsgaard & Kurtz, 2010).

The energy equation can also be written to show explicitly the relation between adiabatic changes in pressure and density:

$$\frac{\mathrm{d}p}{\mathrm{d}t} = \Gamma_1 \frac{p}{\rho} \frac{\mathrm{d}\rho}{\mathrm{d}t}. \tag{2.13}$$

### 2.2.2 Deviation from equilibrium state: perturbation analysis

The theory of stellar oscillations can be described by first order perturbations (or small perturbations) of the basic hydrodynamic equations around a state of equilibrium. Within this context, a generic variable $\varphi$ of the problem (e.g. the pressure, the density, etc...) can be written in the form:

$$\varphi(\boldsymbol{r}, t) = \varphi_0(\boldsymbol{r}) + \varphi'(\boldsymbol{r}, t), \tag{2.14}$$

where "0„ corresponds to the value at the equilibrium, while "′„ indicates the perturbation. Eq. 2.14 is referred to the perturbation of $\varphi$ at fixed position (**Eulerian perturbation**). Alternatively, we can instead consider the frame of reference that follows an element of the fluid. In this case, the variation $\delta\varphi$ of $\varphi_0$ induced by the element motion from an initial position $\boldsymbol{r}_0$ to $\boldsymbol{r}_0 + \boldsymbol{\delta r}$ (**Lagrangian perturbation**):

$$\delta\varphi = \varphi(\boldsymbol{r}_0 + \boldsymbol{\delta r}) - \varphi_0(\boldsymbol{r}_0) = \varphi(\boldsymbol{r}_0) - \varphi_0(\boldsymbol{r}_0) + \boldsymbol{\delta r} \cdot \boldsymbol{\nabla}\varphi = \varphi'(\boldsymbol{r}_0) + \boldsymbol{\delta r} \cdot \boldsymbol{\nabla}\varphi. \tag{2.15}$$

If we consider $\varphi \equiv \rho$ and we substitute eq. 2.14 into the continuity equation, we find

$$\frac{\partial \rho'}{\partial t} + \boldsymbol{\nabla} \cdot (\rho_0 \boldsymbol{v}) = 0, \tag{2.16}$$

where $\boldsymbol{v}$ is the partial time derivative of the displacement $\boldsymbol{\delta r}$. $\rho' \boldsymbol{\nabla} \cdot \boldsymbol{v}$ and $\boldsymbol{v} \cdot \boldsymbol{\nabla}\rho'$ were cancelled out since are terms of the second order.

Similarly, for the equation of motion, energy, and Poisson we have:

$$\rho_0 \frac{\partial \boldsymbol{v}}{\partial t} = -\nabla p' + \rho_0 \boldsymbol{g}' + \rho' \boldsymbol{g}_0, \tag{2.17}$$

$$p' + \boldsymbol{\delta r} \cdot \boldsymbol{\nabla} p_0 = \Gamma_{1_0} \frac{p_0}{\rho_0} (\rho' + \delta \boldsymbol{r} \cdot \boldsymbol{\nabla} \rho_0), \tag{2.18}$$

$$\nabla^2 \Phi' = -4\pi G \rho'. \tag{2.19}$$

These four equations are the **perturbed hydrodynamic equations**.

### 2.2.3 Example of application: simple waves

In the formulation of equation 2.9 we considered the presence of two forces: the pressure gradient and the gravity. Starting from the set of perturbed equations, this opens up a whole range of simple oscillatory waves that we are going to explore in the following paragraphs.

#### Acoustic waves

For this scenario, we assume that the fluid is spatially homogeneous and the only restoring force is given by the pressure. Therefore the gravitational terms in the set of equations are considered negligible and the equation of motion simply becomes:

$$\rho_0 \frac{\partial^2 \boldsymbol{\delta r}}{\partial t^2} = -\nabla p'. \tag{2.20}$$

This equation can be further simplified by taking its divergence and introducing eq. 2.18, finding:

$$\frac{\partial^2 p'}{\partial t^2} = c_0^2 \nabla^2 p', \tag{2.21}$$

where $c_0$ is the adiabatic sound speed

$$c_0 = \sqrt{\Gamma_{1_0} \frac{p_0}{\rho_0}}. \tag{2.22}$$

(where $\Gamma_{1_0}$ is the adiabatic coeffient). The equation found is in the form of a wave equation. An acceptable solution is the monochromatic wave function of frequency $\omega$ (radiant per second) and wave vector $\boldsymbol{k}$ (radiant per cm):

$$p' = A e^{i(\boldsymbol{k} \cdot \boldsymbol{r} - \omega t)} \tag{2.23}$$

If we substitute eq. 2.23 into 2.21, we have

$$-\omega^2 = c_0^2 \left|\boldsymbol{k}\right|^2, \tag{2.24}$$

which represents the **dispersion relation** for the acoustic wave.
We want now to identify the direction of the displacement with respect to the propagation. A real solution of $p'$ is:

$$p' = A\cos(\boldsymbol{k}\cdot\boldsymbol{r} + \omega t). \tag{2.25}$$

Considering a $xyz$ coordinate system in which $\boldsymbol{k}$ is parallel with $x$, eq. 2.20 becomes:

$$\begin{cases} \dfrac{\partial \boldsymbol{v}_x}{\partial t} = -\dfrac{1}{\rho_0}\nabla_x p' = \dfrac{A}{\rho_0}\sin(\boldsymbol{k}\cdot\boldsymbol{r} + \omega t)\boldsymbol{k}_x \neq 0 \\ \dfrac{\partial \boldsymbol{v}_y}{\partial t} = -\dfrac{1}{\rho_0}\nabla_y p' = 0 \\ \dfrac{\partial \boldsymbol{v}_z}{\partial t} = -\dfrac{1}{\rho_0}\nabla_z p' = 0 \quad . \end{cases} \tag{2.26}$$

Therefore only the component of $\boldsymbol{v}$ parallel to $\boldsymbol{k}$ will vary with time, while $\boldsymbol{v}_y$ and $\boldsymbol{v}_z$ remain constant. Choosing the coordinate system where these components are null, the displacement $\boldsymbol{\delta r}$ has same direction the wave (**longitudinal wave**).
The relevance of adopting a monochromatic wave function as solution of eq. 2.21 comes from the Fourier's analysis, for which a generic wave that satisfied the equation can be seen as a superposition of monochromatic waves of different frequencies and amplitudes.

### Internal gravity waves

We now assume the fluid to be incompressible and stratified under the action of a gravitational potential, whose perturbations can be considered negligible. This leads to several consequences:

1. The fluid is inhomogeneous with respect to a preferred direction. Let's assume a spherical coordinate defining only two coordinate: the radial $r$ and the horizontal component $\boldsymbol{h}$ (see the Chapter appendix 2.1). For simplicity the vectorial quantities, like the displacement, can be decomposed along the radial and horizontal coordinates

$$\boldsymbol{\delta r} = \xi_{\mathrm{r}}\boldsymbol{a}_{\mathrm{r}} + \boldsymbol{\xi}_{\mathrm{h}}. \tag{2.27}$$

   We assume that fluid is inhomogeneous in the radial direction.

2. Since the gravitational perturbations are negligible, by the hydrostatic relation the gradient of the pressure will be negligible as well.

3. Given the incompressibility of the fluid, any density perturbations induced by changes of pressure can be ignored.

The perturbed equation of motion for this case will be:

$$\rho_0 \frac{\partial \boldsymbol{v}}{\partial t} = -\nabla p' + \rho' \boldsymbol{g}_0. \tag{2.28}$$

If we assume again a monochromatic solution for $\delta r$, $p'$, and $\rho'$ in the form $Ae^{i(\boldsymbol{k}\cdot\boldsymbol{r}-\omega t)}$, the equations of motion for the radial and horizontal component will become

$$\begin{cases} \rho_0 \omega^2 \xi_\mathrm{r} = i k_\mathrm{r} p' + \rho' g_0 \\ \rho_0 \omega^2 \boldsymbol{\xi}_\mathrm{h} = i \boldsymbol{k}_\mathrm{h} p' \quad . \end{cases} \tag{2.29}$$

while the equation of continuity will be:

$$\rho' + \rho_0 i k_\mathrm{r} \xi_\mathrm{r} + \rho_0 i \boldsymbol{k}_\mathrm{h} \cdot \boldsymbol{\xi}_\mathrm{h} = 0. \tag{2.30}$$

Combining the two equations together we find:

$$\rho_0 \omega^2 \left(1 + \frac{k_\mathrm{r}^2}{k_\mathrm{h}^2}\right) \xi_\mathrm{r} = \left(i \frac{k_\mathrm{r}}{k_\mathrm{h}^2} \omega^2 + g_0\right) \rho'. \tag{2.31}$$

If we study this equation in the very low frequency range with respect to the gravitational acceleration($\omega^2 \ll k_h^2/k_r g_0$) , the complex term on the right can be ignored, simplifying to:

$$\rho_0 \omega^2 \left(1 + \frac{k_\mathrm{r}^2}{k_\mathrm{h}^2}\right) \xi_\mathrm{r} = g_0 \rho' \tag{2.32}$$

and, recalling the adiabatic relation (perturbed energy equation, eq. 2.18), we find the dispersion relation for the internal gravity waves:

$$\omega^2 = \frac{N^2}{1 + k_\mathrm{r}^2/k_\mathrm{h}^2}, \tag{2.33}$$

where $N$ is the **Brunt-Väisälä frequency**:

$$N^2 = g_0 \left(\frac{1}{\Gamma_{1_0}} \frac{\mathrm{d} \ln p_0}{\mathrm{d}r} - \frac{\mathrm{d} \ln \rho_0}{\mathrm{d}r}\right). \tag{2.34}$$

The Brunt-Väisälä frequencies is strictly connected to the convective stability, and in particular to the Ledoux criterion. This can be simply seen introducing the logarithm gradients in eq. 2.34:

$$N^2 = \frac{g_0^2 \rho_0}{p_0} \frac{\chi_T}{\chi_\rho} \left( \nabla_{\rm ad} - \nabla_T - \frac{\chi_\mu}{\chi_T} \nabla_\mu \right). \tag{2.35}$$

Under the assumption of an adiabatic displacement, the Brunt-Väisälä frequency describes at what rate a parcel oscillates vertically around its equilibrium position in any point of the fluid. $N^2$ could be either positive or negative. If $N^2 < 0$, then the fluid is unstable to convection, the frequency $\omega$ is complex and the wave solution behaves exponentially with time. On the contrary, if $N^2 > 0$, $\omega$ is real and the motion is oscillatory: in this case the fluid is convectively stable.

**Surface gravity waves**

In this scenario I consider an indefinitely deep incompressible fluid with a free surface, constant density $\rho_o$ and under the presence of a uniform gravity acceleration $\boldsymbol{g}$ directed along the radial coordinate $r$ (with $r = 0$ at the surface). The situation we are going to analyse generates waves due to a discontinuity in density on the surface of the fluid. Moreover, the wave will propagate along the horizontal coordinate $h$ on surface . Since $\rho'$ is null (incompressible fluid), the equation of continuity will be reduced to the divergence of $\boldsymbol{v}$ equal to 0:

$$\boldsymbol{\nabla} \cdot \boldsymbol{v} = 0. \tag{2.36}$$

The perturbation of the gravity $\boldsymbol{g'}$ will be negligible too, and the equation of motion simply becomes:

$$\rho_0 \frac{\partial \boldsymbol{v}}{\partial t} = -\nabla p'. \tag{2.37}$$

Taking its divergence and substituting in the continuity equation, we find:

$$\nabla^2 p' = 0. \tag{2.38}$$

The solution can be in the form

$$p' = f(r) \cos(k_{\rm h} h - \omega t). \tag{2.39}$$

where $f$ is (from eq. 2.37)

$$\frac{\mathrm{d}^2 f}{\mathrm{d}r^2} = k_\mathrm{h}^2 f \Longrightarrow f = A\mathrm{e}^{-k_\mathrm{h} r}. \tag{2.40}$$

Therefore, the solutions for the displacement (in the $r$ and $h$ directions) are:

$$\begin{cases} \xi_\mathrm{r} = -A\dfrac{k_\mathrm{h}}{\rho_0\omega^2}\mathrm{e}^{-k_\mathrm{h} r}\cos(k_\mathrm{h} h - \omega t) = -\dfrac{k_\mathrm{h}}{\rho_0\omega^2}p' \\ \xi_\mathrm{h} = -A\dfrac{k_\mathrm{h}}{\rho_0\omega^2}\mathrm{e}^{-k_\mathrm{h} r}\sin(k_\mathrm{h} h - \omega t) \quad . \end{cases} \tag{2.41}$$

This describes a circle whose radius decreases exponentially with $r$ (the depth). To find the dispersion relation for the surface gravity waves, we consider first the boundary condition at the surface that requires the local pressure to be constant (Lagrangian perturbation $\delta p = 0$). Combining this condition with eq. 2.15 for $\varphi \equiv \rho$, eq. 2.39, and $h$ component of eq. 2.41, we find:

$$\omega^2 = g_0 k_\mathrm{h}. \tag{2.42}$$

## 2.3 Equations for Non-Radial Adiabatic Stellar Oscillations

The purpose of this section is to derive the set of differential equations that describes the oscillations in a spherical symmetric structure in equilibrium and under the adiabatic assumption.

### 2.3.1 Variable Separation and Linear Equations

Considering a spherical coordinate system $r, h$ (see Appendix 2.1), the four perturbed equations 2.16-2.19 become:

$$\rho' = \frac{1}{r^2}\frac{\partial}{\partial r}\left(\rho_0 r^2 \xi_r\right) - \rho_0 \boldsymbol{\nabla}_h \cdot \boldsymbol{\xi}_h, \tag{2.43}$$

$$\begin{cases} \rho_0 \dfrac{\partial^2 \xi_r}{\partial t^2} = -\dfrac{\partial p'}{\partial r} - \rho' g_0 - \rho_0 \dfrac{\partial g'}{\partial r} & \text{radial} \\ \rho_0 \dfrac{\partial^2 \boldsymbol{\xi}_h}{\partial t^2} = -\nabla_h p' - \rho_0 \nabla_h \Phi' & \text{horizontal} \quad , \end{cases} \tag{2.44}$$

$$p' + \xi_r \frac{\partial p_0}{\partial r} = \Gamma_{1_0}\frac{p_0}{\rho_0}\left(\rho' + \xi_r \frac{\partial \rho_0}{\partial r}\right), \tag{2.45}$$

$$\frac{1}{r^2}\frac{\partial}{\partial r}\left(r^2\frac{\partial \Phi'}{\partial r}\right) + \nabla_h^2 \Phi' = 4\pi G\rho'. \tag{2.46}$$

The horizontal component of eq. 2.44 can be further simplified taking its divergence and substituting $\boldsymbol{\nabla}_h \cdot \boldsymbol{\xi}_h$ from eq. 2.43:

$$\frac{\partial^2}{\partial t^2}\left[\rho' + \frac{1}{r^2}\frac{\partial}{\partial r}\left(\rho_0 r^2 \xi_r\right)\right] = \nabla_h^2 p' + \rho_0 \nabla_h^2 \Phi'. \tag{2.47}$$

A possible solution for the equations can be expressed as a combination of independent functions of the individual coordinates, including time:

$$\varphi(\boldsymbol{r}, t) = R(r)a(\theta, \phi)\tau(t). \tag{2.48}$$

For what concerns the time-dependent function $\tau(t)$ we can assume a simple expression ($\exp(-i\omega t)$). Concerning the space-dependent part, possible solutions are given by the eigenfunctions of the Laplace operator (see section 2.1): the function $u = R(r)a(\theta, \phi)$ is an eigenfunction of $\nabla^2 u = -\lambda u$ only if $R$ and $a$ satisfy the relation:

$$\frac{1}{R}\frac{\partial}{\partial r}\left(r^2\frac{\partial R}{\partial r}\right) + \lambda r^2 = \frac{L^2 a}{a}, \tag{2.49}$$

which is possible if exist a constant $\mu$ for witch:

$$\begin{cases} \dfrac{1}{R}\dfrac{\partial}{\partial r}\left(r^2\dfrac{\partial R}{\partial r}\right) + \lambda r^2 = \mu & (a) \\ L^2 a = -\mu a. & (b) \end{cases} \tag{2.50}$$

The eigenfunctions of equation 2.50b are known to be the **spherical harmonic** $Y_l^m$ (figure 2.1):

$$Y_l^m(\theta, \phi) = (-1)^m c_{l,m} P_l^m \cos(\theta) e^{im\phi}, \tag{2.51}$$

where $P_l^m$ is the polynomial of Lagrange of angular order (degree) $l$ and azimuthal order $m$ ($l, m \in \mathbb{N}$, $|m| \leq l$) and $c_{l,m}$ a normalization constant.

Regular solutions of eq. 2.50 will be obtained only if

$$\mu = l(l+1). \tag{2.52}$$

The set of dependent variables can be written therefore as:

$$\xi_r = \sqrt{4\pi}\tilde{\xi}_r(r) Y_l^m(\theta, \phi) e^{-i\omega t}, \tag{2.53}$$

$$p' = \sqrt{4\pi}\tilde{p}'(r) Y_l^m(\theta, \phi) e^{-i\omega t}, \tag{2.54}$$

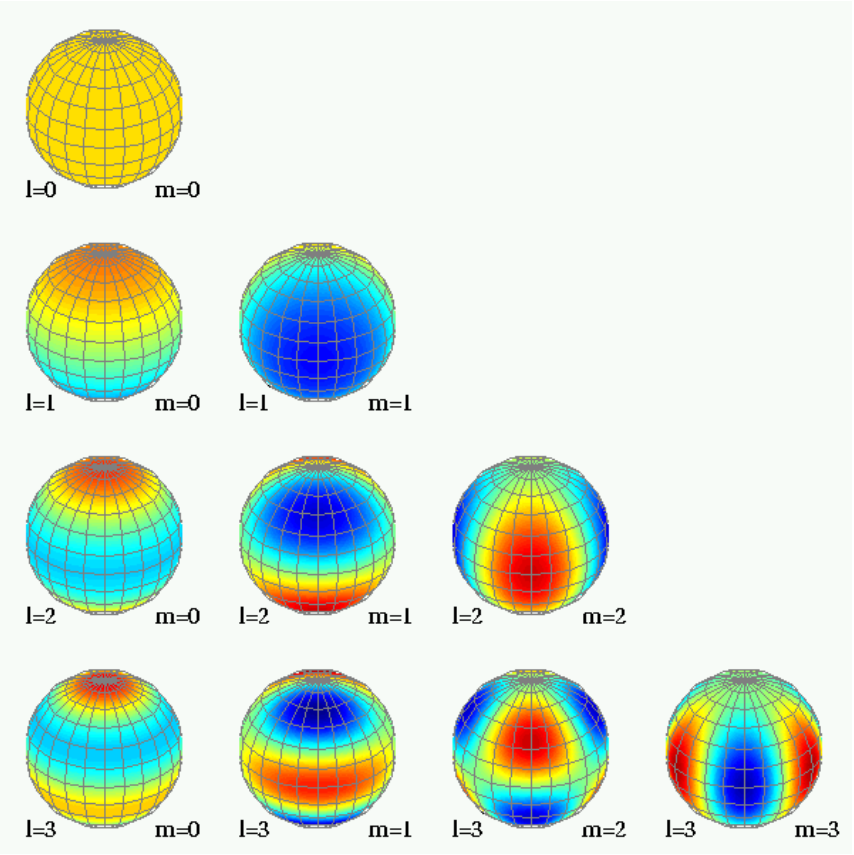


**Figure 2.1:** Representation of spherical harmonics $Y_l^m$. $l$ varies with each line from 0 to 5, while $m$ varies on each column. Credit for the picture to Clem Pryke (http://spud.spa.umn.edu/~pryke/logbook/20000922/static_poles.gif).

$$\boldsymbol{\xi}_h = \sqrt{4\pi}\tilde{\xi}_h(r)\left(\frac{\partial Y_l^m}{\partial\theta} + \frac{1}{\sin\theta}\frac{\partial Y_l^m}{\partial\phi}\right)e^{-i\omega t}, \tag{2.55}$$

with

$$\tilde{\xi}_h = \frac{1}{r\omega^2}\left(\frac{1}{\rho_0}\tilde{p'}(r) + \tilde{\Phi'}\right). \tag{2.56}$$

Finally for the vectorial displacement:

$$\boldsymbol{\delta r} = \sqrt{4\pi}\,\mathrm{Re}\left\{\left[\tilde{\xi}_r\, Y_l^m \boldsymbol{u_r} + \tilde{\xi}_h\left(\frac{\partial Y_l^m}{\partial\theta}\boldsymbol{u_\theta} + \frac{1}{\sin\theta}\frac{\partial Y_l^m}{\partial\phi}\boldsymbol{u_\phi}\right)\right]e^{-i\omega t}\right\}. \tag{2.57}$$

The explicit expression for the functions of the radial coordinates $\tilde{\xi}_r$, $\tilde{\xi}_h$, and $\tilde{p}'$ along with $\tilde{\Phi}'$ can be found substituting eq. 2.53-2.57 into eq. 2.43-2.46 and rearranging as follow:

$$\begin{cases} \dfrac{\mathrm{d}\xi_r}{\mathrm{d}r} = -\left(\dfrac{2}{r} + \dfrac{1}{\Gamma_1 H_p}\right)\xi_r + \dfrac{1}{\rho c^2}\left(\dfrac{S_l^2}{\omega^2} - 1\right)p' + \dfrac{l(l+1)}{\omega^2 r^2}\Phi', & (a) \\ \dfrac{\mathrm{d}p'}{\mathrm{d}r} = \rho\omega^2\left((1 - \dfrac{N^2}{\omega^2}\right)\xi_r + \dfrac{1}{\Gamma_1 H_p}p' + \rho\dfrac{\mathrm{d}\Phi'}{\mathrm{d}r}, & (b) \\ \dfrac{1}{r^2}\dfrac{\mathrm{d}}{\mathrm{d}r}\left(r^2\dfrac{\mathrm{d}\Phi^2}{\mathrm{d}r}\right) = 4\pi G\left(\dfrac{p'}{c^2} + \dfrac{\rho\xi_r}{g}N^2\right) + \dfrac{l(l+1)}{r^2}\Phi', & (c) \end{cases} \tag{2.58}$$

where $H_p$ is the pressure scale (eq. 1.31), $N$ is the Brunt-Väisälä frequency (eq. 2.34) and $S_l$ is another characteristic frequency called the **Lamb frequency**:

$$S_l = l(l+1)\frac{c^2}{r^2}. \tag{2.59}$$

This forms a complete set of differential equations of the 4th order (for matter of simplicity the symbols ˜ and $_0$ were dropped), that depend on only four variables:

$$p, \quad \rho, \quad \Gamma_1, \quad \text{and} \quad g.$$

The unknown variables are $\xi_r$, $p'$, $\Phi'$, and $\dfrac{\mathrm{d}\Phi'}{\mathrm{d}r}$ (or in alternative $\rho'$).

### Boundary Conditions

In order to solve the set of differential equations 2.58 we also need to define the boundary conditions at the centre and at the surface, for a total of four conditions:

**Centre.** The central point corresponds to $r = 0$. It can be shown that by linear expansions of the equations in the limit $r \to 0$, $\xi_r$, $p'$, and $\Phi'$ become:

$$\xi_r \sim \begin{cases} r^{l-1} & l > 0 \\ r & l = 0 \end{cases} \tag{2.60}$$

$$\Phi', p' \sim r^l. \tag{2.61}$$

Therefore $\mathrm{d}\Phi'/\mathrm{d}r$ near the centre will be (first condition):

$$\frac{\mathrm{d}\Phi'}{\mathrm{d}r} = \frac{l}{r}\Phi'. \tag{2.62}$$

It can be noticed that only for $l = 1$, we always have $\xi_r(r = 0) \neq 0$. The second condition comes from the expansion of eq. 2.58b and considering $g = 0$, $N^2 = 0$ and

$N/g = 0$ in the centre. We then obtain:

$$\tilde{\xi}_r - \frac{l}{r\omega^2}\left(\frac{1}{\rho_0}\tilde{p'} + \tilde{\Phi'}\right) \tag{2.63}$$

i.e., reminding eq. 2.56,

$$\xi_r \simeq l\xi_h \tag{2.64}$$

(for $l > 0$).

**Surface.** On the surface $r = R$. The third condition is found imposing the continuity of $\Phi'$ and its derivative at the surface boundary:

$$\frac{\mathrm{d}\Phi'}{\mathrm{d}r} + \frac{l(l+1)}{r}\Phi' = 0, \tag{2.65}$$

which requires to have $\Phi'$ in a form $\Phi' \sim r^{-l-1}$. The last condition is found imposing $p(R)$ constant at the surface that corresponds to impose the Lagrangian perturbation $\delta p$ equal to 0:

$$\delta p = p' + \xi_r \frac{\partial}{\mathrm{d}r} = 0. \tag{2.66}$$

In reality finding this condition on a stellar structure is more complex since it requires a detailed analysis of the atmospheric model applied at he surface.

**limit case: radial oscillations.**

The radial oscillations are a particular family of solutions in which $l = 0$. Since the spherical harmonic $Y_0^0$ is a simple constant (i.e. without the dependency from $\theta$ and $\phi$), the application of the operator $\nabla_h$ to any dependent variables during the resolution of the equations will return 0.

## 2.4 Mode properties

Solving the system of equations 2.58 is the primary aim of oscillation codes like GYRE (Townsend & Teitler, 2013) and LOSC (Scuflaire et al., 2008). The solutions consist in a set of discrete eigenfunctions which describe the properties of oscillation modes. Each solution/mode can be identified by three integers numbers:

- **the radial order** $n$. The radial order corresponds to the numbers of nodes of the mode between the centre and the surface.

- **the angular order** $l$ (or degree). The angular order represents the total number of nodal lines on the stellar surface.

- **the azimuthal order** $m$. The azimuthal order indicates how many of these surface nodal lines cross the equator. In absence of rotation or other features that break the spherical symmetry of the star, $m$ does not affect the frequencies. This can be seen also in the system of differential equations, where $m$ does not appears and therefore cannot influence the solutions.

### 2.4.1 Cowling approximation

The **Cowling approximation** aims to simplify the system of differential equations (eq.2.58) by neglecting the perturbation of the gravitational potential $\Phi'$. This approximation reduces the 4th order differential equation system (eq.2.58) down 2nd order, which is analytically solvable. The number of boundary conditions decreases also to 2. However, the approximation requires that the radial $n$ and angular $l$ orders assume large values. Under the approximation, the equations become:

$$\begin{cases} \dfrac{\mathrm{d}\xi_r}{\mathrm{d}r} = -\left(\dfrac{2}{r} + \dfrac{1}{\Gamma_1 H_p}\right)\xi_r + \dfrac{1}{\rho c^2}\left(\dfrac{S_l^2}{\omega^2} - 1\right)p' & (a) \\ \dfrac{\mathrm{d}p'}{\mathrm{d}r} = \rho\omega^2\left((1 - \dfrac{N^2}{\omega^2}\right)\xi_r + \dfrac{1}{\Gamma_1 H_p}p'. & (b) \end{cases} \tag{2.67}$$

Even if the Cowling approximation does not need to be taken when numerically computing oscillation modes, it introduces simplifications which are very useful to understand the physical properties of the modes, as shown in the next sections.

### 2.4.2 Mode classification

As a first and very rough approximation we can delete the terms in eq.2.67 in which the derivatives of equilibrium quantities appear. The assumption here is that those terms vary slowly compared to the eigenfunctions of high radial order modes:

$$\begin{cases} \dfrac{\mathrm{d}\xi_r}{\mathrm{d}r} = \dfrac{1}{\rho c^2}\left(\dfrac{S_l^2}{\omega^2} - 1\right)p' & (a) \\ \dfrac{\mathrm{d}p'}{\mathrm{d}r} = \rho\omega^2\left((1 - \dfrac{N^2}{\omega^2}\right)\xi_r. & (b) \end{cases} \tag{2.68}$$

Combining these two equations leads to a second order equation:

$$\frac{\mathrm{d}^2\xi_r}{\mathrm{d}r^2} = \frac{\omega^2}{c^2}\left(\frac{S_l^2}{\omega^2} - 1\right)\left(1 - \frac{N^2}{\omega^2}\right)\xi_r. \tag{2.69}$$

Even if eq. 2.69 was derived under rather crude assumptions, it can be used to have simple physical information about the nature of the modes. It shows that the two characteristic frequencies $S_l$ and $N$ play a fundamental role in order to define the mode properties. We define the function $K$ as:

$$K(r) = \frac{\omega^2}{\rho c^2}\left(\frac{S_l^2}{\omega^2} - 1\right)\left(1 - \frac{N^2}{\omega^2}\right). \tag{2.70}$$

The sign of this function will affect the solution of $\xi_r$ which is either an oscillatory function($K > 0$):

$$\xi_r = \cos\left(\int \sqrt{K}\mathrm{d}r + \delta\right) \tag{2.71}$$

or an exponential decay (or growth, $K < 0$):

$$\xi_r = \exp\left(\pm \int \sqrt{|K|}\mathrm{d}r + \delta\right). \tag{2.72}$$

We can therefore distinguish between four possible scenarios depending on the comparison between the mode frequency $\omega$ and the two characteristic frequencies:

**Case 1a**: $|\omega| > |N|$ and $|\omega| > |S_l|$ then $K < 0$: exponential function

**Case 1b**: $|\omega| < |N|$ and $|\omega| < |S_l|$ then $K < 0$: exponential function

**Case 2a**: $|N| < |\omega| < |S_l|$ then $K > 0$: oscillatory function

**Case 2b**: $|S_l| < |\omega| < |N|$ then $K > 0$: oscillatory function

Since $N$ and $S_l$ are functions of $r$, the internal structure of a star may contain several regions where $\xi_r$ goes from an oscillatory to an exponential behaviour. Figure 2.2 gives a schematic overview of the regions where $K$ is positive or negative. In general we identify as **trapping region** a region where $\xi_r$ has an oscillatory behaviour, delimited between two turning points ($K(\tilde{r}) = 0$). The latter correspond either to the beginning of a region where the eigenfunction behaves exponentially or, as a limiting case, the centre and the surface of the star. Typically the modes with high frequency oscillate near the surface and we refer to them as **p-mode**. On the contrary low-frequency modes usually are trapped near the core and they are called **g-modes** (figure 2.2). This definition is related to the main restoring forces that drive the stellar oscillations: the pressure gradient for the p-modes, and the buoyancy for the g-modes.

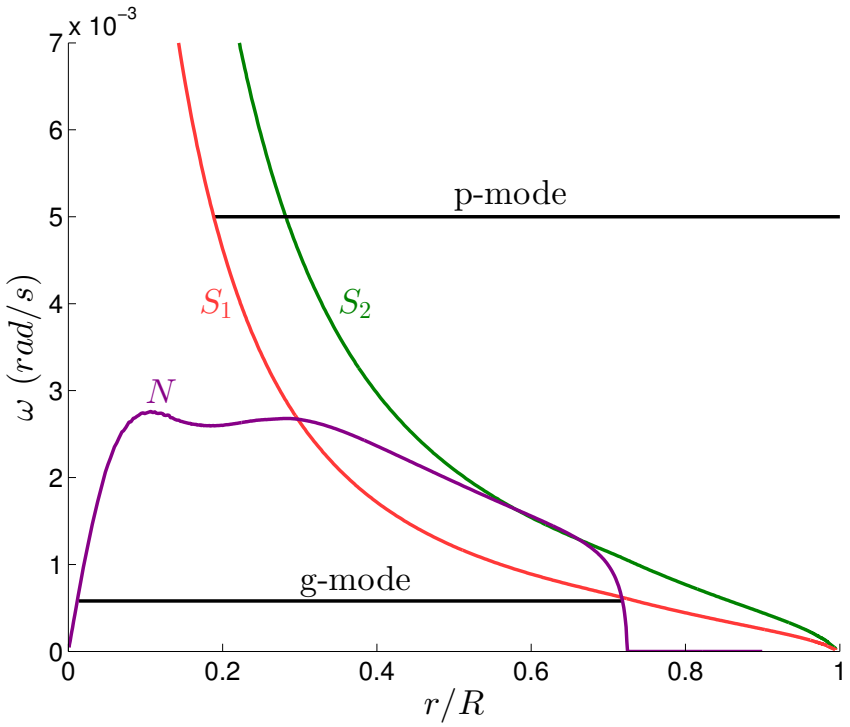


**Figure 2.2:** Schematic example of of a propagation diagram. The star corresponds to the Sun (1 $M_\odot$ solar composition at 4.57 Gyr). Inside the stellar interior 2 types of modes propagate: the p-modes, high frequency modes trapped between the surface and the point where $\omega = S_l$, and the g-modes, low frequency modes trapped in the deep interior inside a cavity delimited by the Brunt-Väisälä frequency.

### 2.4.3 p modes

The pure pressure modes (or p modes) correspond to case 2a. They are standing waves of frequency $\omega$ trapped between the surface and the turning point $\tilde{r}$ that satisfies the expression $\omega^2 = S_l^2(\tilde{r})$. The trapping point at the surface, which is not explained by this simple analysis, can be inferred by a general asymptotic description of the oscillations derived in Deubner & Gough (1984).

It is typical for the p modes having frequencies much larger than the Brunt-Väisälä frequency ($\omega^2 \gg N^2$). Therefore eq. 2.70 is reduced to:

$$K(r) \sim \frac{1}{c^2}\left(\omega^2 - S_l^2\right), \tag{2.73}$$

which recalls the properties of the acoustic waves, since $K(r)$ depends on the variation of the sound speed with $r$. When $n$ is very large, the frequencies $\nu_{nl}$ of the p-mode and the g-mode acquire an asymptotic behaviour (Christensen-Dalsgaard,

2012). For the p-modes with low $l$ the following asymptotic equation holds:

$$\nu_{nl} \simeq \Delta\nu \left( n + \frac{l}{2} + \varepsilon_{\mathrm{p}} \right) - \delta_{nl}, \tag{2.74}$$

where $\varepsilon_{\mathrm{p}}$ is a phase dependent on the boundary conditions. The quantity $\Delta\nu$ is called **large separation** and is equal to the frequency difference between two modes of consecutive order $n$ and the same degree $l$. This quantity is nearly constant, making the pressure modes almost exactly equally spaced. The large separation is of the order of the inverse of twice the **acoustic radius** (time required for a sound wave to travel from the centre to the surface of a star):

$$\Delta\nu = \left( 2 \int_0^R \frac{\mathrm{d}r}{c} \right)^{-1}. \tag{2.75}$$

Finally $\delta_{nl}$ is a small correction also known as **small separation** (see chapter 3 for more details).

### 2.4.4 g modes

g-modes are defined by the case 2b. These are low frequencies modes trapped in the stellar interior between two turning points, which are given by the equality $N^2 = \omega^2$. Similarly to the approximation 2.76 for the p-modes, for high order g-modes we have $\omega^2 \ll S_l$ and, consequently:

$$K(r) \sim \left( \frac{N^2}{\omega^2} - 1 \right) \frac{l(l+1)}{r^2}. \tag{2.76}$$

Equation 2.76 reveals similarities with the internal gravity waves, both related to the buoyancy frequency $N$.

The asymptotic behaviour for large $n$ g-modes periods $\Pi_{nl}$ is characterized by the relation:

$$\Pi_{nl} = \frac{1}{\nu_{nl}} \simeq \Delta\Pi_{\mathrm{g}_l} \left( n + \varepsilon_{\mathrm{g}} \right), \tag{2.77}$$

where $\varepsilon_{\mathrm{g}}$ is a phase and $\Delta\Pi_l$ is the **Period Spacing**. Thus, similarly to the p-modes, the frequencies $\nu_{nl}$ of g-modes are related by an asymptotic relation where their periods are equally spaced by $\Delta\Pi_l$. The period spacing is proportional to the inverse of the integral of the Brunt-Väisälä frequency inside the trapping cavity:

$$\Delta\Pi_{\mathrm{g}_l} = \frac{2\pi^2}{\sqrt{l(l+1)}} \left( \int_{r_1}^{r_2} \frac{N}{r} \mathrm{d}r \right)^{-1}, \tag{2.78}$$

where $r_1$ and $r_2$ are the turning points that limit the cavity.

### 2.4.5 Mode inertia

An important property of the oscillation modes is the **inertia**. This quantity is related to the kinetic energy of the mode of frequency $\omega$ by the expression:

$$E_{\rm k} = \frac{1}{2}\int_V |\boldsymbol{v}|^2 \rho_0 {\rm d}V = \frac{1}{2} E\, M v_{\rm rms}^2, \tag{2.79}$$

where $M$ is the total mass, $v_{\rm rms}$ the mean square speed (averaged over the spherical surface and the time), and $E$ is the normalized inertia (hereafter simply inertia). The inertia is defined as the integral of the second moment of the density over the volume, normalized by its value at the surface:

$$E = \frac{\displaystyle\int_V \rho_0 \left|\boldsymbol{\delta r}\right|^2 {\rm d}V}{M\left|\boldsymbol{\delta r}_{\rm surf}\right|^2}. \tag{2.80}$$

It is useful here to introduce the mean square components of $\boldsymbol{\delta r}$, calculated taking the average over the spherical surface and time:

$$\begin{cases} \delta r_{\rm rms}^2 = \left\langle \left|\boldsymbol{\delta r}\cdot\boldsymbol{u_r}\right|^2 \right\rangle = \dfrac{1}{2}\left|\tilde{\xi}_r(r)\right|^2 & \text{radial} \\ \delta h_{\rm rms}^2 = \left\langle \left|\boldsymbol{\delta h}\right|^2 \right\rangle = \dfrac{1}{2} l(l+1)\left|\tilde{\xi}_h(r)\right|^2 & \text{horizontal} \end{cases} \tag{2.81}$$

Inserting these terms in eq.2.80, we finally find:

$$E = \frac{4\pi\displaystyle\int_0^R \left[\left|\tilde{\xi}_r(r)\right|^2 + l(l+1)\left|\tilde{\xi}_h(r)\right|^2\right]\rho_0 r^2 {\rm d}r}{M\left[\left|\tilde{\xi}_r(R)\right|^2 + l(l+1)\left|\tilde{\xi}_h(R)\right|^2\right]}, \tag{2.82}$$

with $R$ being the total radius. Pressure modes have in general a lower value of $E$ than gravity modes. This is due to the term $\rho_0 r^2$ in eq. 2.82 that has a maximum in the near-centre region, where g modes have the largest amplitudes of their eigenfunction $\boldsymbol{\xi}$, differently from p modes that have larger amplitudes near the surface. This characteristic will become useful in section 3.4.3, in which we will be dealing with stars that show rather complicated spectra with modes of mixed pressure and gravity character.

## 2.5 Global properties of solar-like oscillation spectra

The Fourier analysis of stellar light curves can reveal their detailed oscillation spectra, it is however useful at this point to introduce few global properties of such a spectrum. An example of an observed oscillation spectrum is shown in figure 2.3, where the power spectral density (PSD) of the star KIC 6442183, a SGB star observed by *Kepler* is presented as a function of frequency.
It can be observed that the amplitude of the frequencies are distributed consistently with a Gaussian-like envelope. The centre of the Gaussian envelope corresponds to the frequency of the maximum oscillation power, also called $\nu_{\max}$. It can be noticed that the closer an observed frequency is to $\nu_{\max}$, the easier it is to detect it. The behaviour of $\nu_{\max}$ as a function of stellar properties has yet no a solid theoretical base but has been observed to scale – to a first approximation – with the acoustic cut off $\omega_{\rm ac}$ (Brown et al., 1991). Kjeldsen & Bedding (1995) proposed a scaling relation to estimate $\nu_{\max}$ as:

$$\nu_{\max} \propto \omega_{\rm ac} \propto M R^{-2} {T_{\rm eff}}^{-1/2}. \tag{2.83}$$

An estimate of the width of the Gaussian envelope was instead given by Mosser et al. (2012a) who provided an empirical equation for the standard deviation $\sigma$, as function only of $\nu_{\max}$:

$$\sigma = 0.66 \cdot \nu_{\max}^{0.88}. \tag{2.84}$$

In addition, frequencies in the power spectra often show a regular pattern in frequency which is due to the near-constant large separation $\Delta\nu$. $\Delta\nu$ scales to a very good approximation with the square of the mean density of the star:

$$\Delta\nu \simeq \sqrt{\overline{\rho}}\,\Delta\nu_\odot = \sqrt{\frac{M/\mathrm{M}_\odot}{R/\mathrm{R}_\odot}}\Delta\nu_\odot, \tag{2.85}$$

where $\Delta\nu_\odot$ is the large frequency separation of the Sun.
The relation 2.85 and 2.83 are known as **seismic scaling relations**. Their importance is fundamental since, in combination with the $T_{\rm eff}$ and/or the luminosity, they are able to provide us a direct measure of the mass, and radius of the stars:

$$L = \left(\frac{\Delta\nu}{\Delta\nu_\odot}\right)^{-4} \left(\frac{\nu_{\max}}{\nu_{\max\odot}}\right)^{2} \left(\frac{T_{\rm eff}}{\mathrm{T}_{\rm eff,\odot}}\right)^{5}, \tag{2.86}$$

$$M = \left(\frac{\Delta\nu}{\Delta\nu_\odot}\right)^{-4} \left(\frac{\nu_{\max}}{\nu_{\max\odot}}\right)^{3} \left(\frac{T_{\rm eff}}{\mathrm{T}_{\rm eff,\odot}}\right)^{\frac{3}{2}}, \tag{2.87}$$

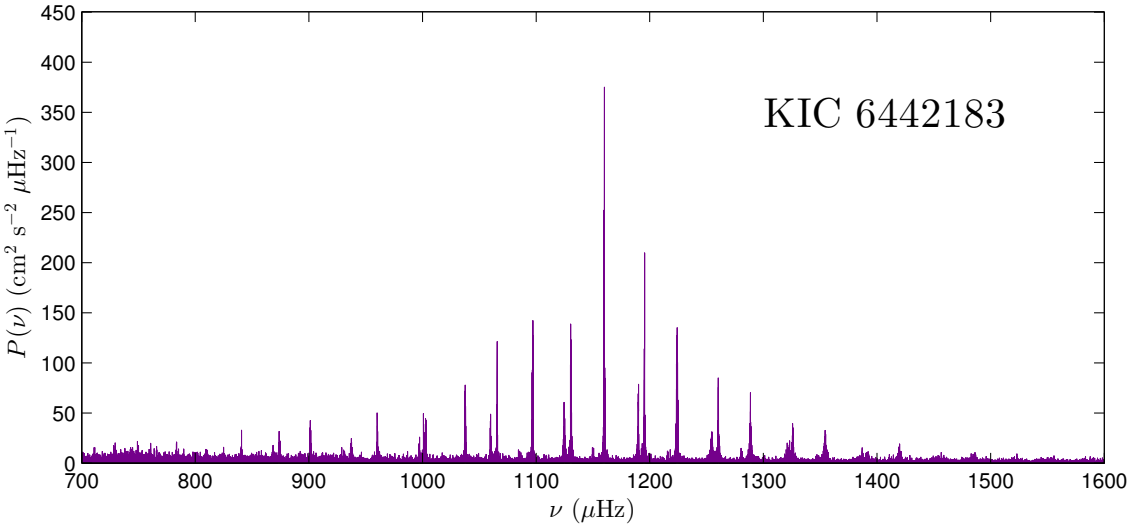


**Figure 2.3:** Power spectrum of a SGB star observed by *Kepler*

$$R = \left(\frac{\Delta\nu}{\Delta\nu_\odot}\right)^{-2} \left(\frac{\nu_{\max}}{\nu_{\max\odot}}\right) \left(\frac{T_{\rm eff}}{\rm T_{eff,\odot}}\right)^{\frac{1}{2}}. \tag{2.88}$$

Testing the accuracy of the $\Delta\nu$ scaling is therefore key to making accurate inferences on stellar properties, and will be addressed in chapter 3.

## 2.6 Mixed Modes in Red Giants

As the central density increases the Brunt-Väisälä frequency reaches high values in the central regions. The frequency range of the g-modes and p-modes start to overlap, generating a new peculiar set of modes called **mixed modes**. The eigenfunctions of this class of modes are characterised by a p-like behaviour in the envelope and a g-like behaviour near the centre. Since by definition pure g-modes have no radial solutions (no $l = 0$), the mixed mode are possible only for modes with angular degree $l > 0$.

### 2.6.1 Evolution of the modes

I will now present how the frequencies change along the evolution of a Sun-like star(1.0 $\rm M_\odot$ , [Fe/H] = 0). For the purpose of the discussion, I use here stellar models that will described in more detail in section 4.2. As introduced previously in this chapter, the behaviour of the modes depend on two fundamental frequencies, the Lamb and the Brunt-Väisälä frequency. However, other factors are involved in the modes properties and in their detectability, like $\nu_{\max}$ and the inertia.

**Main sequence** Starting from the main sequence, the distinction between p-modes and g-modes is obvious (figure 2.4a). In stars like the Sun, the only modes that appear in the power spectrum are p-modes, since $\nu_{\max}$ assumes very high values (e.g. $\nu_{\max\odot} = 3100\ \mu$Hz). On the contrary, g-modes are confined to a very low frequency range, making their detection a hard – and still open – challenge for helioseismology (Christensen-Dalsgaard, 2002), This is due to the external convective zone which damps the oscillations.

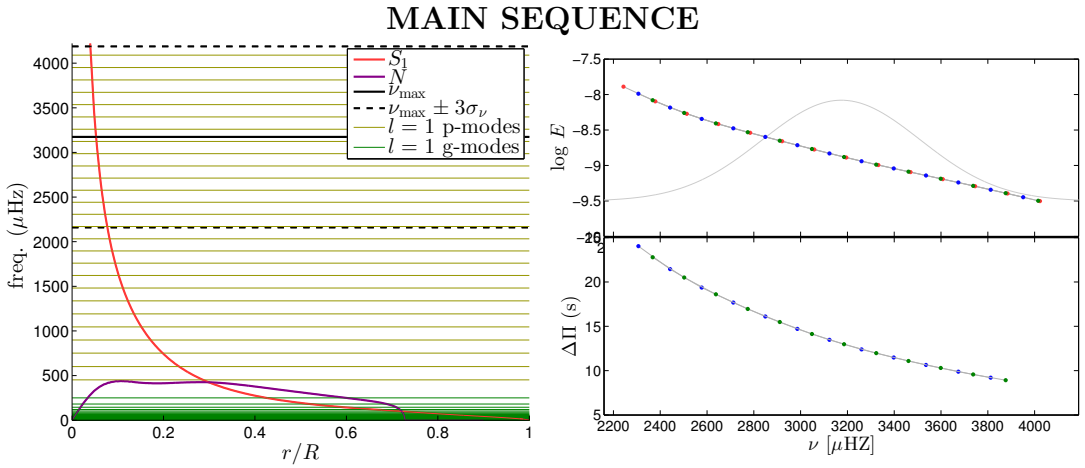


**Figure 2.4:** ***Left.*** Propagation diagram for a MS 1.0 $M_\odot$star. The violet line is the Brunt-Väisälä frequency, the red line the Lamb frequency for $l = 1$, the green and gold horizontal lines indicate respectively the g-modes, and p-modes for $l = 1$, the black lines give an indication of the range of detectability of the oscillations ($\nu_{\max} \pm 3\sigma$, where $\sigma$ is given by eq. 2.84).
***Right.*** $l = 0, 1, 2$, frequencies for 5 models along the evolution of a 1.0$M_\odot$track. *top panel.* Mode Inertia against frequencies. *bottom panel.* period spacing against frequencies.

**Sub Giant Branch** The situation changes after the end of the central hydrogen burning and the contraction of the core. The Brunt-Väisälä frequency rises and the first mixed modes appear (figure 2.5).

**Red Giant Branch** Red Giants are excellent laboratories to study the properties of mixed modes. From an observational point of view, all the modes that we can detect (with the exception of radial modes) belong to the mixed mode class. Along the red-giant branch, the core becomes more and more compact while the envelope expands. With the dependence of $\nu_{\max}$ on radius (eq. 2.83), the range of detectability of the modes shifts to low frequencies, while the growing central density increases the Brunt-Väisälä frequency, increasing the frequencies of g-modes. The number of detected modes in the power spectrum is therefore increasing along the RGB (figures 2.6-2.7). Figure 2.7 is an excellent example of a typical power spectrum of a red-giant star. This model is calculated just after the RGB bump. It can be noticed

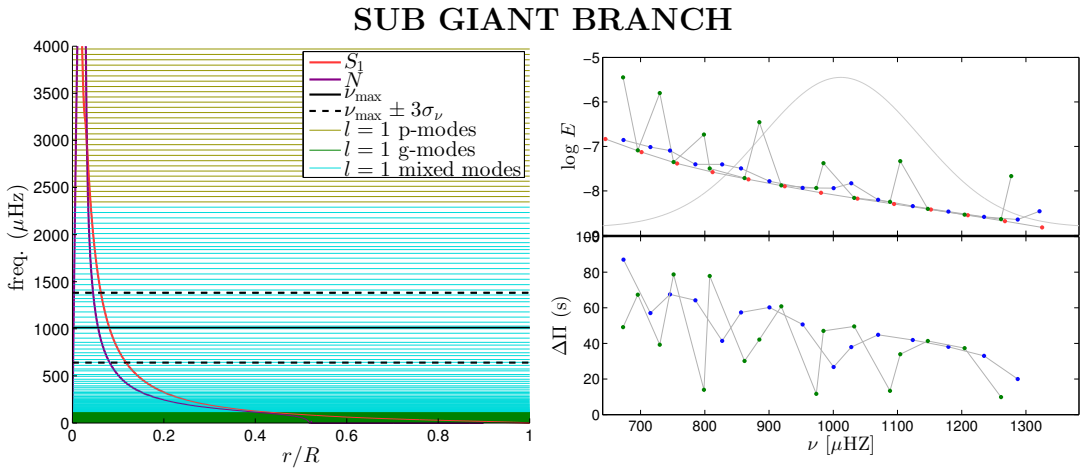


**Figure 2.5:** Propagation diagram and f$l = 0, 1, 2$, frequencies for a SGB 1.0M$_\odot$star (see caption figure 2.4)

that all the $l = 1$ frequencies around $\nu_{\max}$ are mixed modes. Looking at the top-right, we can see how the inertia of the $l = 0, 1, 2$ vary with the frequency and with the angular degree. Focusing on the $l = 1$ modes, the inertia describes a series of "arches" as a function of $\nu$. Within each arch we can identify a mode with low inertia with respect to the others and a numerous number of modes with high and similar inertia (around the centre of each arch). The modes with the lower inertia have characteristics more similar to a p-mode then a g-modes and are therefore called **p-like modes**. We can in fact see that they are almost equally spaced in frequency, as expected from the asymptotic expression for the p-mode, eq. 2.74. On the other hand, the modes with higher inertia appear to be regularly spaced in period (figure 2.7, bottom-right panel). These modes have more **g-like** characteristics, and they tend to follow a law similar to eq. 2.77.

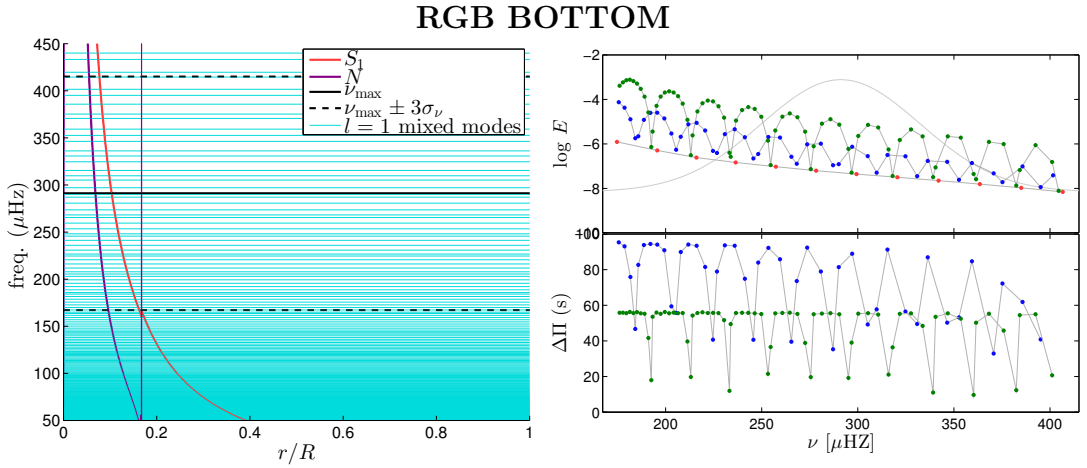


**Figure 2.6:** Propagation diagram and f$l = 0, 1, 2$, frequencies for a 1.0M$_\odot$star at the bottom of the RGB (see caption figure 2.4)

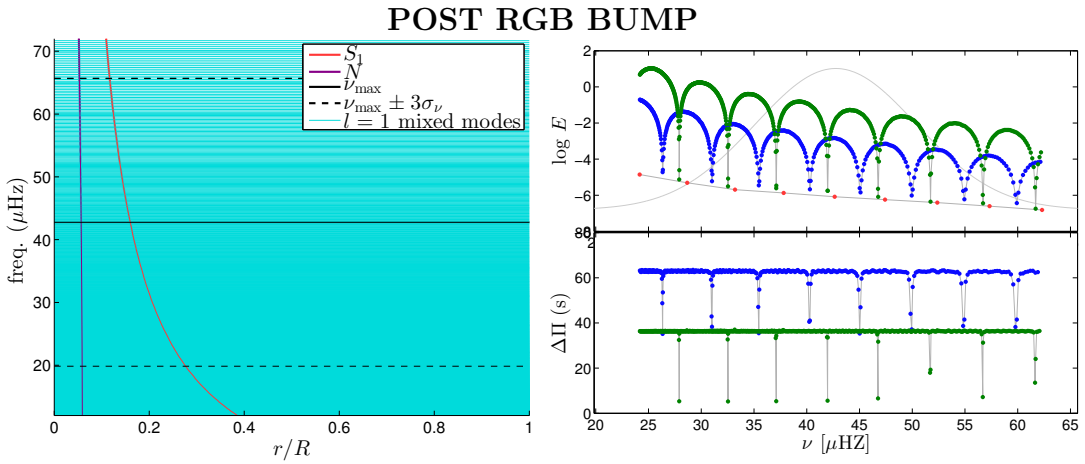


**Figure 2.7:** Propagation diagram and f$l = 0, 1, 2$, frequencies for a 1.0M$_\odot$star after the RGB bump (see caption figure 2.4)

**Helium Flash** At the tip of the RGB, the stars reach the temperature to ignite the helium nuclear reactions in the near-core region. As I introduced in Chapter 1, the presence of those reactions is coupled with convection, due to their high energy generation rate. In additiction, stars along the RGB are affected by neutrino energy loss that moves the maximum of temperature ($T_{\rm max}$) outside the centre. As consequence , stars during the helium flash develop a convective shell in their He-rich core, that forms an extra internal g-cavities and makes their power spectrum extremely complex.

**Helium-Core Burning** Helium-core-burning stars are the main subject of chapter 4, I therefore just anticipate some of their characteristics. Similarly to RGB, these stars have a spectrum rich of mixed modes (figure 2.8). However, since the core is convective, the extension of the g-cavity is reduced, increasing their period spacing (in agreement with equations 2.78 and 2.35). Moreover, the chemical composition discontinuity of the core might, in some particular models (like overshooting models, see chapter 4 and Bossini et al. 2015), create glitches in the power spectrum, introducing an extra periodicity for the period spacing of the g-like modes.

**Post Helium-Core Burning** Despite for the additional burning shell, the AGB stars have internal properties similar to RGB stars: a compact core and a single g-cavity.

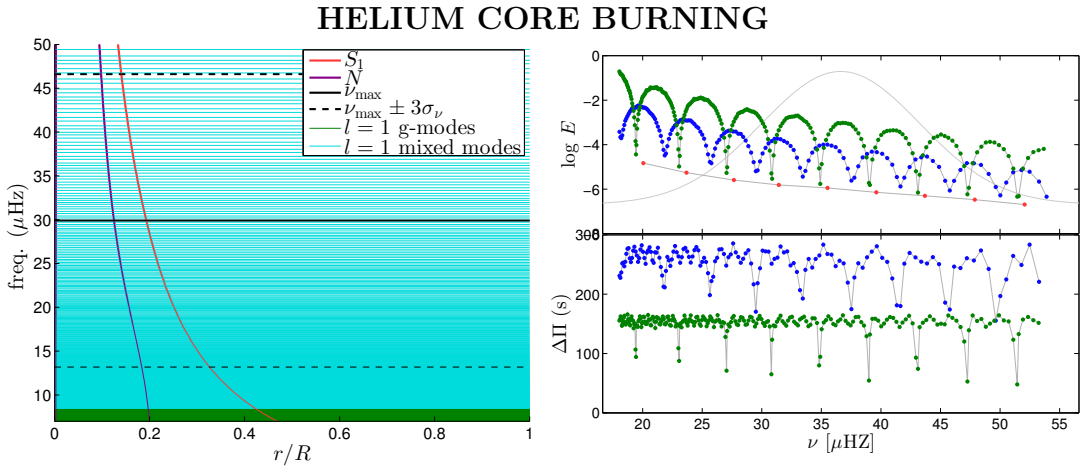


**Figure 2.8:** Propagation diagram and f$l = 0, 1, 2$, frequencies for a 1.0M$_\odot$star during the He-core Burning (see caption figure 2.4)

# Part II

# Computations for Asteroseismology: Problems in Theoretical Predictions

# Chapter 3

# Stellar Model Computations: Evolutionary Tracks and Seismic Predictions

## 3.1 Evolutionary Tracks Computations

A stellar evolution code is a program designed to solve numerically the set of fundamental differential equations introduced in chapter 1. It outputs a series of "snapshots" of the stellar interior at consecutive timesteps of varying duration, allowing to track the evolution of a star from its formation to the more advanced stages. In this work, I make extensive use of evolution codes, especially the *Modules for Experiments in Stellar Astrophysics* (MESA) code (Paxton et al., 2011, 2013, 2015). In this section I describe the basic physical inputs I adopted in the majority of the models presented in this work. From now on, I will refer to these settings with the abbreviation "IP1", specifying any possible variation case by case. IP1 was adopted in the papers by Bossini et al. (2015), Rodrigues & Bossini et al. (in preparation), and Handberg et al. (submitted, see appendix).

### 3.1.1 Chemical Elements.

One of the main input parameters in a stellar evolution code is the initial chemical composition. It is defined by the mass fraction of hydrogen ($X$), helium ($Y$), and the rest of the elements (metals, $Z$), so that

$$1 = X + Y + Z. \tag{3.1}$$

However, in order to track the abundances of the single elements (like C, O, etc...), it is necessary to know their relative initial distribution in $Z$. Usually their relative abundances are assumed to scale as in the Sun. In our case, the initial partition of heavy elements chosen is the one described in Grevesse & Noels (1993). In some special scenarios, like for instance very-metal-poor stars, it important to take into account deviations from the solar partition, enhancing the $\alpha$ elements. I refer to these cases with the term **$\alpha$-enhancement** and the abundance of the $\alpha$ elements is given by [$\alpha$/Fe]:

$$[\alpha/\mathrm{Fe}] = \log\left(\frac{X_\alpha}{X_{\mathrm{Fe}}}\right)_{\mathrm{star}} - \log\left(\frac{X_\alpha}{X_{\mathrm{Fe}}}\right)_{\odot}, \tag{3.2}$$

where $X_\alpha$ and $X_{\mathrm{Fe}}$ are the mass fractions of the $\alpha$ elements and of Fe.

### 3.1.2 Nuclear Reactions

Another important ingredient in stellar models are nuclear reaction rates. In IP1 I adopted the rates given by Angulo et al. (1999). They provide a large number of tabulated nuclear cross sections relevant to the main nuclear-burning stages in stellar evolution (e.g. hydrogen and helium burning). These values are measured by extrapolation from laboratory experiments. Once we move from laboratory conditions to the astrophysical environment, such as the stellar interior, the uncertainties on the nuclear cross section become relevant (e.g. Imbriani et al., 2001; degl'Innocenti et al., 2004), changing the efficiency of the nuclear reactions which affects also the lifetimes of the burning phases and the chemical abundances of the stellar interiors. One major source of uncertainty is, for instance, the nuclear cross section of the $^{12}\mathrm{C}(\alpha,\gamma)^{16}\mathrm{O}$ (see e.g. Metcalfe, Salaris & Winget, 2002; Straniero et al., 2003; Cassisi, Salaris & Irwin, 2003) reaction. Its effect on the helium-core burning and the subsequent phases will be presented in Chapter 5.

### 3.1.3 Opacity

The value of the local opacity inside the stellar structure is estimated by interpolating in pre-compiled tables. In IP1 I used the tables produced by the OPAL group (Iglesias & Rogers, 1996). They use a code that determines the opacity for a given chemical composition (including the initial partition of heavy elements), the temperature and density. They make available two types of opacity tables:

**Type 1 (TO1):** These tables are meant to be used in the regions where there is no nuclear burning that affects the relative distribution of metals in Z. The opacity

is given by the interpolation in 4 variables: $X$, $Z$, $\log T$, and $\log R$. The latter is defined as:

$$\log R = \log \rho - 3 \cdot \log T. \tag{3.3}$$

An example of these tables is given in figure 3.1, where the opacity is plotted as a function of $\log T$ and $\log R$ at fixed $X$ (0.35) and for 2 values of Z (0.004, and 0.1)

**Type 2 (TO2):** During the He-burning stage one has to properly account for the C and O abundance changes in the stellar matter and their effect on radiative opacities. Therefore the final interpolation will be made in 6 variables: $X$, $Z_{\rm ini}$, C, O, $\log T$, and $\log R$.
While the TO1 can be adopted only when the metallicity is not significantly changed from the initial value, TO2 can in principle cover both pre and post He-burning events. However, it must be underlined that TO1 have usually a better resolution than TO2, improving the accuracy of the interpolation. In order to test and compare how MESA and other codes estimate the opacity, I created a program that integrates MESA opacity module and recalculates $\kappa$ taking as input a previously computed structure. I will give here an simple example of the functionality of the code applied to two RG models in the RGB and HeCB phase. The two models have equal mass ($M = 1.6$ M$_\odot$) and metallicity ($Z = $ Z$_\odot$), and similar luminosity ($\log L/$L$_\odot \sim 1.76$). I tested the opacity under different conditions:

1. type 1 opacity table with current $Z$ (standard MESA);
2. type 1 opacity table with initial $Z$;
3. type 2 opacity table.

The effects can be seen in figure 3.2, which shows the near-core opacity profile in the two red giants. No difference in the RGB model can be noticed [1], suggesting that all the three methods achieve similar precision. The situation in HeCB star is however different. It is possible to divide the model in three main areas: the convective core (from the centre to about mass coordinate $\sim 0.2$ M$_\odot$), the rest of the He-rich core (from the convective border to mass $\sim 0.48$), and the H-rich region above. Without any extra input, MESA uses the TO1 as default in all the three areas, interpolating on the local $Z$ (blue line). However, this may lead to inaccurate opacities in the central area for two main reasons. First of all, the upper limit for $Z$ in OPAL table is $Z = 0.2$, therefore the program cannot interpolate when the metallicity grows over

[1] except for a small variation near the centre between the original model and the program output, due to different numerical precision.

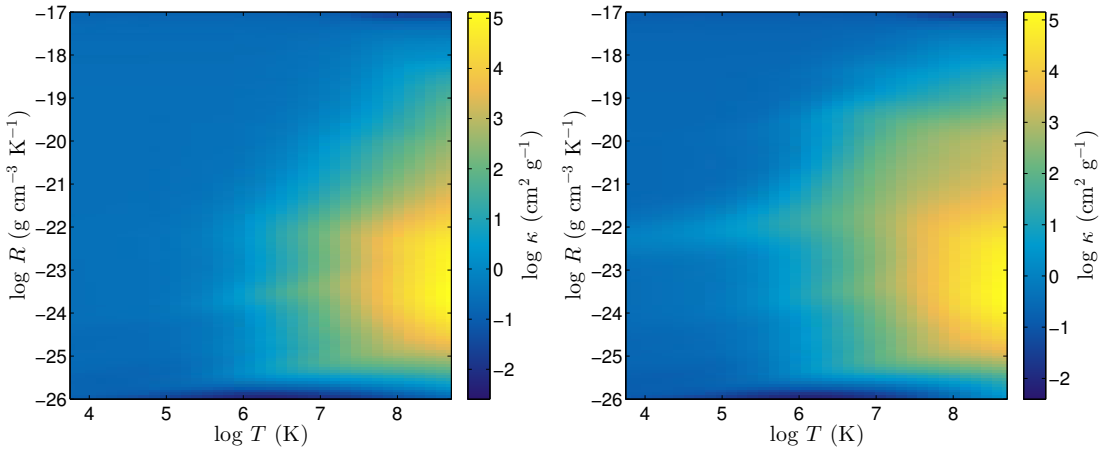


**Figure 3.1:** An example of tables produced by OPAL group (Iglesias & Rogers, 1996). Opacity is plotted as function of $\log T$ and $\log R$ at fixed $X$ (0.35) and for $Z = 0.004$ (left), and $Z = 0.100$ (right).

this threshold, preventing the opacity to increase –as expected– in the convective core. Second, during the helium burning the metallicity increases only due to the contribution of the carbon and oxygen, changing their mass partition in $Z$. If the C/O enhancement is not taken in account, a simple increment of $Z$ will increase also the mass fractions of heavier metals (like e.g. Fe) that introduce a large contribution to the opacity, especially in the initial phases of the HeCB and in the He-rich region (since the helium flash has slightly increased by $\sim 0.2$ the C+O mass fraction in this region). As a consequence this set-up tends to overestimate the opacity in the convective core at the beginning of the HeCB, while $\kappa$ is underestimated in the later phases of the central burning. Considering the initial $Z$ instead of the current value, prevents only the overestimation of $\kappa$ in the He-rich core, but does not solve the issue in the centre. The latter case (TO2 only) is able to better reproduce the condition of the entire core. In order to compute models from the pre-main sequence to the first AGB thermal pulse, I set up MESA to maintain the standard TO1 interpolation (case 1) above the H-shell only and to use TO2 below it. This is done also considering a blending region in which the two solutions are linearly composed between the $10^{-10} < X < 10^{-6}$.

The OPAL opacities were used complemented by low-temperature opacities from Ferguson et al. (2005) in the range $30000 - 500$ K.

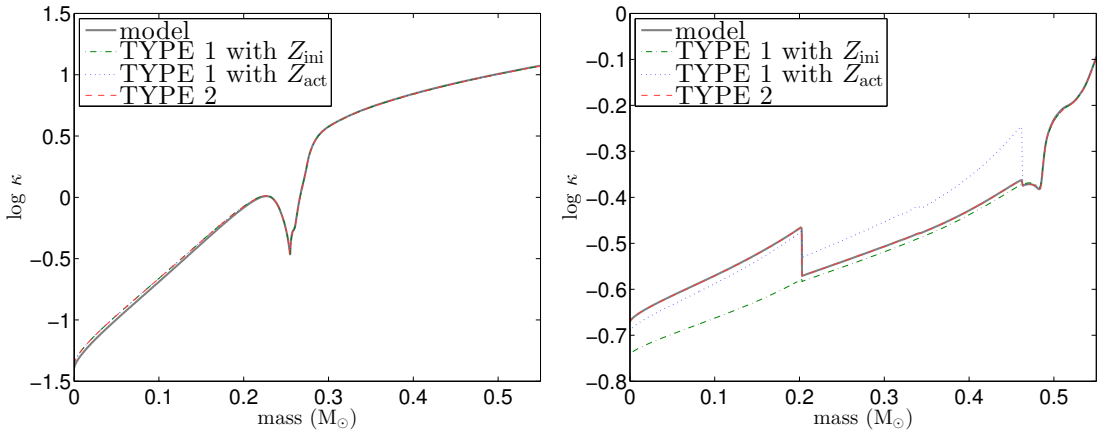


**Figure 3.2:** An example of tables produced by OPAL group (Iglesias & Rogers, 1996). Opacity is plotted as function of log $T$ and log $R$ at fixed $X$ (0.35) and for $Z = 0.004$ (left), and $Z = 0.100$ (right).

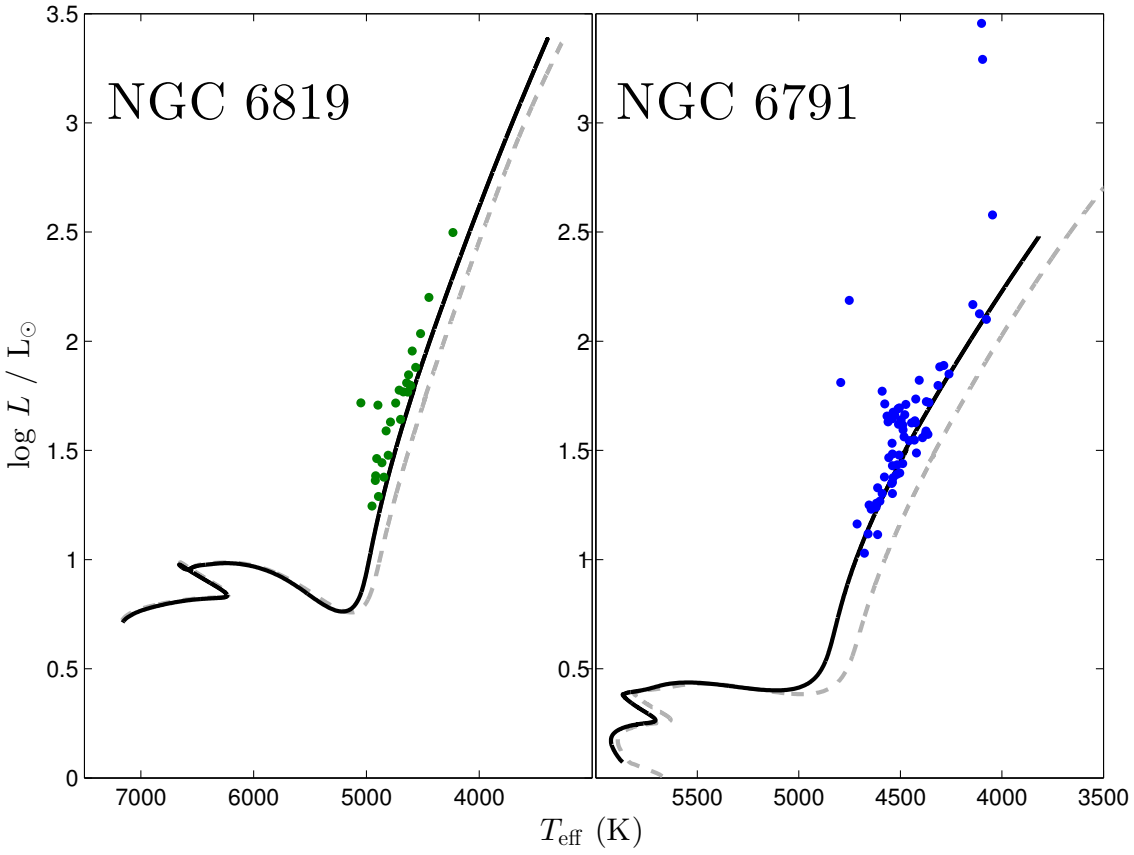


**Figure 3.3:** HRD of the clusters NGC 6819 (left panel) and NGC 6791 (right panel). The lines are evolutionary tracks corresponding to the typical mass star on the RGB and metallicity of the clusters (respectively $M = 1.60$ M$_\odot$ and $Z = 0.01756$ for NGC 6819 and $M = 1.15$ M$_\odot$ and $Z = 0.0350$ for NGC 6791). In black the tracks computed with Krishna Swamy (1966) atmosphere model while in grey with an Eddington-grey atmosphere model. It can be noticed that the black lines fit better the RGB stars of the clusters.

| Atmosphere model | $\alpha_{\mathrm{MLT}}$ | $\mathrm{Z}_{\odot}$ | $Y_{\odot}$ | $\log L/\ \mathrm{L}_{\odot}$ | $\log R/\ \mathrm{R}_{\odot}$ |
|---|---|---|---|---|---|
| Eddinton-grey | 1.692784 | 0.01756 | 0.26556 | $0.246360 \cdot 10^{-7}$ | $0.103382 \cdot 10^{-6}$ |
| Krishna Swamy (1966) | 1.965719 | 0.01756 | 0.26618 | $0.364275 \cdot 10^{-5}$ | $-0.421175 \cdot 10^{-6}$ |

**Table 3.1:** Result of the solar calibration for the physical inputs IP1 end two different atmosphere models.

### 3.1.4 Atmosphere

### 3.1.5 Convective Core on the Main Sequence

In convective cores, extra mixing (overshooting) is considered. Our standard prescription for main-sequence stars is the one described in Maeder (1975), which consists in an instantaneous mixing of the region above the classical border. The size of the extra-mixing region is assumed to be $0.2H_p$, where $H_p$ is the pressure scale at the border of the convective core. An exhaustive description of the mixing schemes will be presented later in the section 3.2. The value 0.2 is compatible with the results presented in Aerts (2015) for OB stars.

### 3.1.6 Solar Calibration

Once the physical inputs are fixed, the output of the computation must be calibrated on a real star. The most logical choice is the Sun, since is a typical and well known low-mass star. This means that the 1.0 $\mathrm{M}_{\odot}$ solar-abundance track must reproduce the solar proprieties at the age equal to the age of the Sun. I performed an iterative algorithm in which I search for a combination of the mixing length parameter ($\alpha_{\mathrm{MLT}}$), the initial metallicity, and the initial helium mass fraction that reproduces the solar radius and luminosity at the age of 4.57 Gyr with a precision of $\delta \log R, \delta \log L < 10^{-5}$. The algorithm is based the minimization method "Nelder-Mead"(Nelder & Mead, 1965) applied to $\chi^2$:

$$\chi^2 = \left( \frac{\log R_{\mathrm{mod}} - \log \mathrm{R}_{\odot}}{\delta \log R} \right)^2 + \left( \frac{\log L_{\mathrm{mod}} - \log \mathrm{L}_{\odot}}{\delta \log L} \right)^2 . \tag{3.4}$$

The results of the solar calibration for are listed in Tabel 3.1.

## 3.2 Mixing Schemes

During the main sequence and the helium-core-burning phase, stars may develop convective cores. However, the treatment of the core convection is still matter of discussion (especially in the HeCB, Straniero et al. 2003), and the different assump-

tions, which usually affect the size of the mixed region, have a direct impact of various aspects of the current and subsequent phases. For example, the duration of the HeCB phase: a larger core increases the helium available for the nuclear reactions, and more time is required to burn it all. The effect of the different mixing schemes is the main topic of the chapters 4, 5, and 6. In this section I will simply introduce their main characteristics. Sections 3.2.1 and 3.2.2 are reported as written in (Bossini et al., 2015).

### 3.2.1 Bare-Schwarzschild

This mixing scheme considers no extra mixing involved. The border of the convective core is imposed in accordance with the Schwarzschild criterion. In the case of HeCB stars, the convective core is not allowed to grow (in mass), leading to a discontinuity in the chemical composition (hence in the radiative gradient) at its border. The discontinuity becomes more pronounced as well as the evolution proceeds (Figure 3.4 panel a).

### 3.2.2 Induced Overshooting and He-Semiconvection

A recent paper by Gabriel et al. (2014) showed how this implementation of the Schwarzschild criterion in HeCB stars leads to an inconsistent location of the convective border, as the convective luminosity is non-zero there ($\nabla_{\rm rad} > \nabla_{\rm ad}$ at the inner side of the convective boundary). The book of Schwarzschild (1958) and the analysis presented in Castellani, Giannone & Renzini (1971a) also led to similar conclusions. The latter consider the BS convective border as in an unstable equilibrium, in the sense that by extending outwards the convective core by an arbitrarily small quantity, $\nabla_{\rm rad}$ at the new border may be larger than $\nabla_{\rm ad}$, hence, the region is convectively unstable according to the Schwarzschild criterion. To find a stable border, the convective core must be extended until the radiative and adiabatic gradient become equal (**induced overshooting**). However, as the HeCB proceeds ($Y_{\rm c} \sim 0.69$) this scheme generates a local minimum in $\nabla_{\rm rad}$ within the mixed core. The addition of radiative layers surrounding the increasingly larger convective core will decrease $\nabla_{\rm rad}$ to the value of $\nabla_{\rm ad}$ at the location of the minimum. This creates a separate convective region in layers beyond the location of this minimum, where $\nabla_{\rm rad}$ is still larger than $\nabla_{\rm ad}$. The treatment of this external convective region is problematic. Full mixing between layers inside the minimum of $\nabla_{\rm rad}$ and the external convective shell cannot happen, because otherwise the minimum of $\nabla_{\rm rad}$ would decrease below the local value of $\nabla_{\rm ad}$ and the layer would end up being convectively stable. A so-

lution to this problem is the formation of a partially mixed –*semiconvective*– region between the minimum of $\nabla_{\rm rad}$ and the outer radiative zone (Castellani, Giannone & Renzini, 1971b). This is usually treated with dedicated algorithms that allow for partial chemical mixing to satisfy $\nabla_{\rm rad} = \nabla_{\rm ad}$ in this region, with the consequence of creating a smooth gradient of chemical composition before the sharp discontinuity due to the HeCB.
I include in MESA a special routine in order to implement a similar prescription. This routine consists in the following steps:

1. at the beginning of each timestep I set the position of the convective-core boundary and fully mix the convective region according to the Schwarzschild criterion as implemented in MESA.

2. I let the code calculate the burning during the timestep.

3. at the end of the timestep, I check whether the radiative gradient (with the new composition determined by the burning) at the convective border is higher than the adiabatic gradient.

4a. if this is the case, I restart the timestep from point 1, but extending the core boundary by one mesh.

4b. if not, the equality of the gradients has been achieved and the code can continue to the next timestep (point 1).

As a result of this algorithm, the convective core extends naturally (Fig. 3.4 panel b). However, a routine to treat He-semiconvection is still to be developed in MESA, limiting the evolution of this treatment until $Y_{\rm c} \sim 0.69$.

### 3.2.3 Step Function Overshooting

One of the possible treatments that extends the mixing beyond the classical border is the convective **overshooting**. It is based on the hypothesis that the convective elements that reach the point where $\nabla_{\rm rad} = \nabla_{\rm ad}$ still have a residual kinetic energy. Therefore they can penetrate into the surrounding radiative zone, increasing the region affected by convective mixing. This phenomenon is not limited to HeCB phase but can be applied also to MS stars and any other phases that require convection. The **Step Function** is a type of possible mixing scheme that goes under the name overshooting. It follows the description given by Maeder (1975) and consists in extending the mixed region above the classical border by a fixed fraction of the

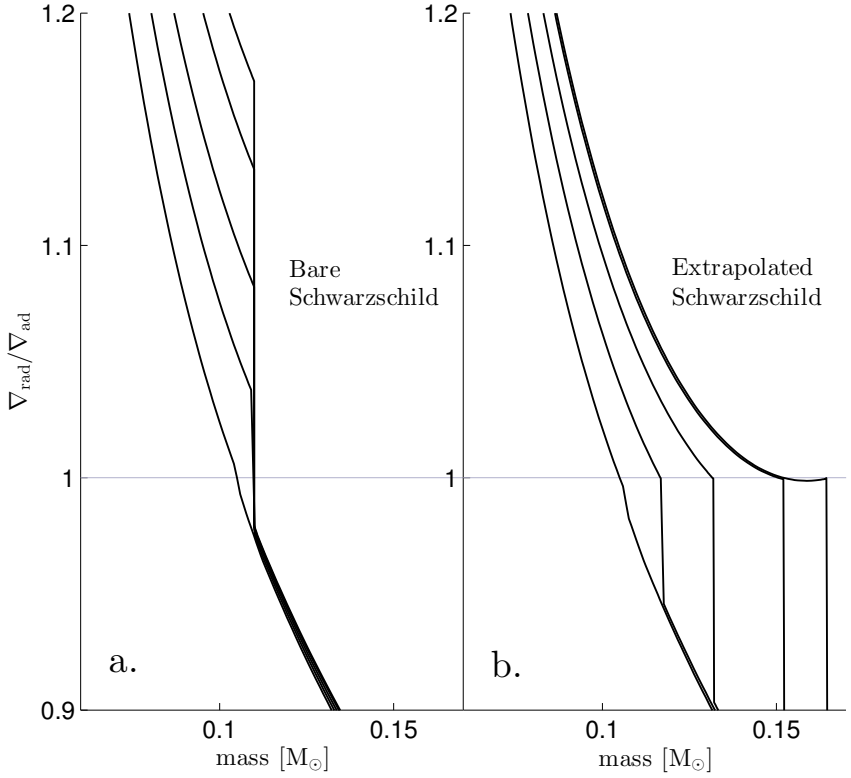


**Figure 3.4:** Ratio between the radiative and adiabatic temperature gradients as a function of mass in MESA HeCB models computed using the BS (*panel a*) and ES (*panel b*) scheme. The latter leads to a self-consistent definition of the convective boundary (following the Schwarzschild criterion), as the adiabatic and radiative gradients are equal at the boundary of the core. From bottom to top the lines are for a sequence of models at the stages of $Y_c = 0.93$, 0.87, 0.81, 0.74, and 0.70.

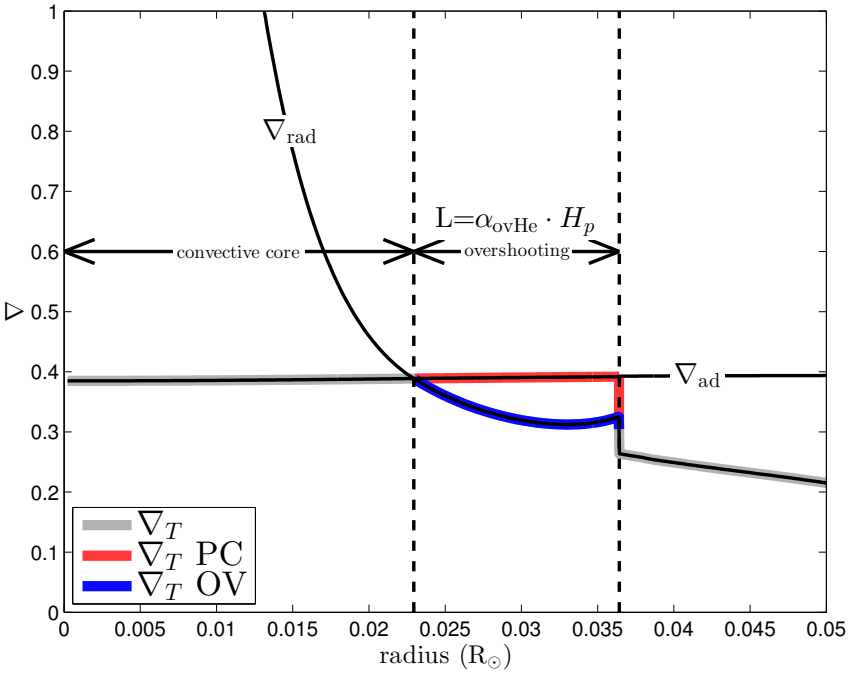


**Figure 3.5:** Schematic description of the step function overshooting (section 3.2.3).

pressure scale height, which is taken at the Schwarzschild border. This scheme is completely parametric and the value of the fraction of the pressure scale height, called **overshooting parameter**, might change from one burning type to another. I will use $\alpha_{\rm ovH}$ to refer to overshooting in the H-burning phase, while $\alpha_{\rm ovHe}$ is used for helium burning. The overshooting region is considered to be quickly mixed with respect to the typical evolutionary timesteps. In MESA a diffusive coefficient, whose value is fixed and taken just below the Schwarzschild border, is applied on the entire region. Figure 3.5 gives a schematic overview of the scheme for a star during the HeCB. However, the profile of $H_p$ as function of the radius tends to diverge to infinite for $r \to 0$, making the treatment for small core tricky. As highlight in Deheuvels et al. (2016), MESA redefines $H_p$ as $R_{\rm cc}\alpha_{\rm MLT}$ ($R_{\rm cc}$, radius of the classical core) when $l_{\rm mlt} > R_{\rm mc}$. An alternative approach is to consider the minimum between $H_p$ and the radius of the convective core (Roxburgh, 1992).

### 3.2.4 Penetrative Convection

In addition to the overshooting parameter, another source of uncertainty can be the thermal stratification ($\nabla_T$) to adopt in the extra mixed region. According to the definition given in Zahn (1991), if we impose $\nabla_{T\rm ovsh} = \nabla_{\rm rad}$ we have the classic overshooting (OV), while if $\nabla_{T\rm ovsh} = \nabla_{\rm ad}$, we have **penetrative convection** (PC, figure 3.5). In terms of their effects on global evolutionary properties (age and

location on HRD), the overshooting and the penetrative convection do not differ significantly. However, the two schemes modify differently the profile of Brunt-Väisälä frequency and, therefore, the period spacing with the effect that $\Delta\Pi_{\rm OV}$ is usually smaller than $\Delta\Pi_{\rm PC}$.

### 3.2.5 Diffusive Overshooting

Another type of overshooting is the **Diffusive Overshooting** (Herwig, 2000). In this case the overshooting parameter $f_{\rm ovsh}$ defines the diffusive coefficient $D_{\rm ovsh}$ at each point of the star above the classical border by the equation:

$$D_{\rm ovsh}(r) = D_0 \exp\left(-2\frac{r - R_{\rm cc}}{f_{\rm ovsh} H_p}\right), \tag{3.5}$$

where $D_0$ is the diffusive coefficient taken just inside the classical border. This kind of overshooting does not allow the formation of chemical discontinuities. It must be noticed that, since eq.3.5 is an exponential decay law, a jump in chemical composition for evolved HeCB stars will be present anyway, even if it will be smooth.

### 3.2.6 Modified Overshooting

The treatment of He-semiconvection is important also in overshooting (and penetrative convection) schemes, especially for low and moderate values of the $\alpha_{\rm ovHe}$. Similarly to the induced overshooting, during the HeCB evolution a local minimum in $\nabla_{\rm rad}$ is formed in the mixed region, while a local maximum is present at the extra-mixing border due to the increasing opacity (consequence of the high C+O abundance). If this local maximum becomes higher than $\nabla_{\rm ad}$, a He-semiconvection region is formed. Without a dedicated semiconvection treatment, if $\alpha_{\rm ovHe}$ is not large enough, $\nabla_{\rm rad}$ will at some point increase above $\nabla_{\rm ad}$, joining together the two convectively unstable regions (see figure 3.6). In codes like MESA this particular situation generates a numerical problem: MESA in fact is not able to distinguish the actual classical border from the overshooting region (since they are both convective and now joined) and it will attach the overshooting to the former extra-mixing region, leading to an non-physical injection of helium in the core (figure 3.6, fourth panel). To overcome this problem I implemented a new prescription named **modified overshooting**. In this scheme I define the convective border as the point where $\nabla_{\rm rad} = \nabla_{\rm ad}$, in accordance with Schwarzschild criterion, or the minimum of $\nabla_{\rm rad}$, if it has increased over $\nabla_{\rm ad}$ (figure 3.7).

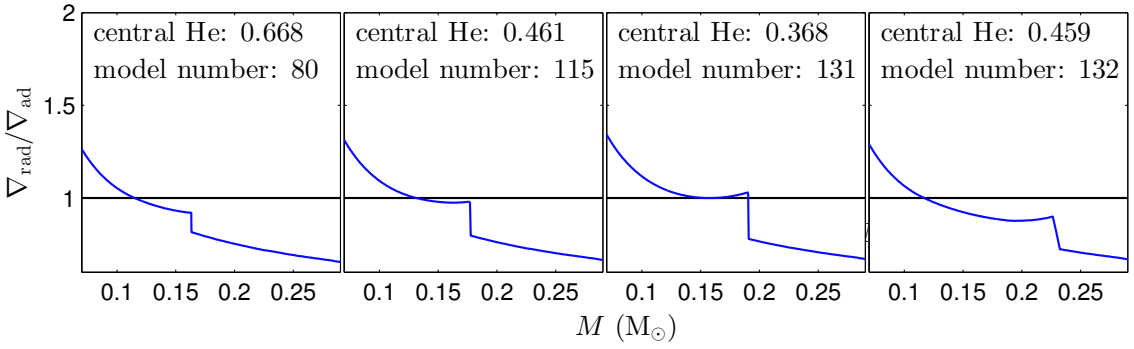


**Figure 3.6:** Temperature gradients profiles in consecutive 1.50 $M_\odot$ HeCB models when a standard $\alpha_{\rm ovHe} = 0.3$ overshooting (step function) is applied in MESA. The panels shows how the gradients evolve with time. In the fourth panel a is possible to see the effect of numerical problem generated by the missing classical border identification. This profile experienced a large injection of helium.

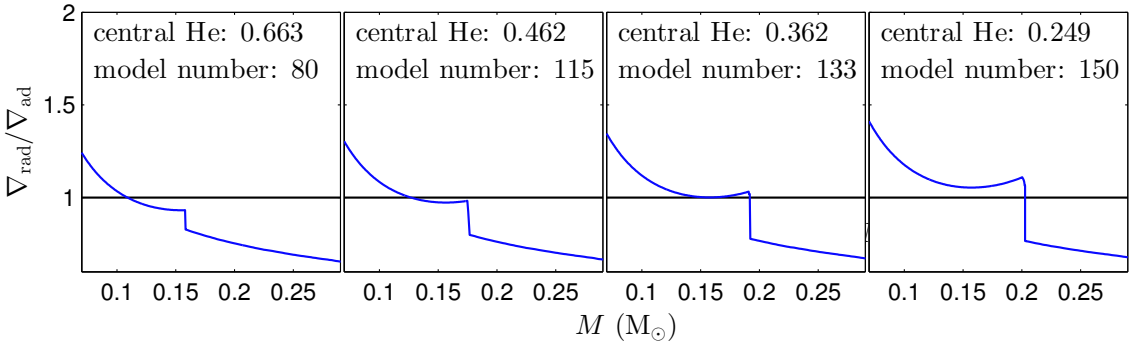


**Figure 3.7:** Temperature gradients profiles in consecutive HeCB models with the "modified overshooting" $\alpha_{\rm ovHe} = 0.3$ (step function) applied. In this scenario the classical border is taken equal to the minimum in $\nabla_{\rm rad}$ inside the convective region, when such minimum is above $\nabla_{\rm ad}$.

## 3.3 A New Grid of Models

The procedures and techniques I described in the previous sections have been used to build a new grid of models. The grid of models was computed using MESA. The physical inputs are the ones I have described as PI1 (section 4.2). The range of mass considered is $M = 0.6 - 2.5$ M$_\odot$, in combination with 7 different metallicities ([Fe/H]= $[-1.00; 0.50]$). The following points summarize the additional physical inputs used:

- The tracks were computed starting from the pre-main sequence (PMS) up to the first thermal pulse of the AGB (TP-AGB).
- The atmosphere is taken according to Krishna Swamy (1966) model.
- Overshooting was applied during the core-convective-burning. I use overshooting with a parameter of $\alpha_{\rm ovH} = 0.2H_p$ during the main sequence, while, following the and the results in Bossini et al. 2015 (see Chapter 4), I consider $\alpha_{\rm ovHe} = 0.5H_p$ penetrative convection in the HeCB phase.
- Metallicities [Fe/H] were converted in mass fractions $Z$ by the formula $Z = Z_\odot \cdot 10^{\rm [Fe/H]}$ where $Z_\odot = 0.1756$, from the solar calibration. The initial helium $Y$ depends on $Z$ and was set using a linear helium enrichment expression:

$$Y = Y_p + \frac{\Delta Y}{\Delta Z} Z, \tag{3.6}$$

  with the primordial helium abundance $Y_p = 0.2485$ and the slope $\Delta Y/\Delta Z = \frac{Y_\odot - Y_p}{Z_\odot} = 1.007$. Table 3.2 shows the relationship between metallicity [Fe/H], the mass fraction of heavy elements $Z$, and the initial helium mass fraction $Y$ for the tracks computed.

The HRD of the tracks is presented in figure 3.8. For every track I saved about 100-200 single structures along their evolution. The grid is extensively used in Chapter 5 to study the dependency of the period spacing on the mass and metallicity and in Rodrigues & Bossini et al..

## 3.4 Frequency Computations

In this work, the computation of theoretical oscillation frequencies was carried out using **GYRE** (Townsend & Teitler, 2013). GYRE is a code that calculates oscillation modes from a given stellar structure, solving the equations presented in Chapter

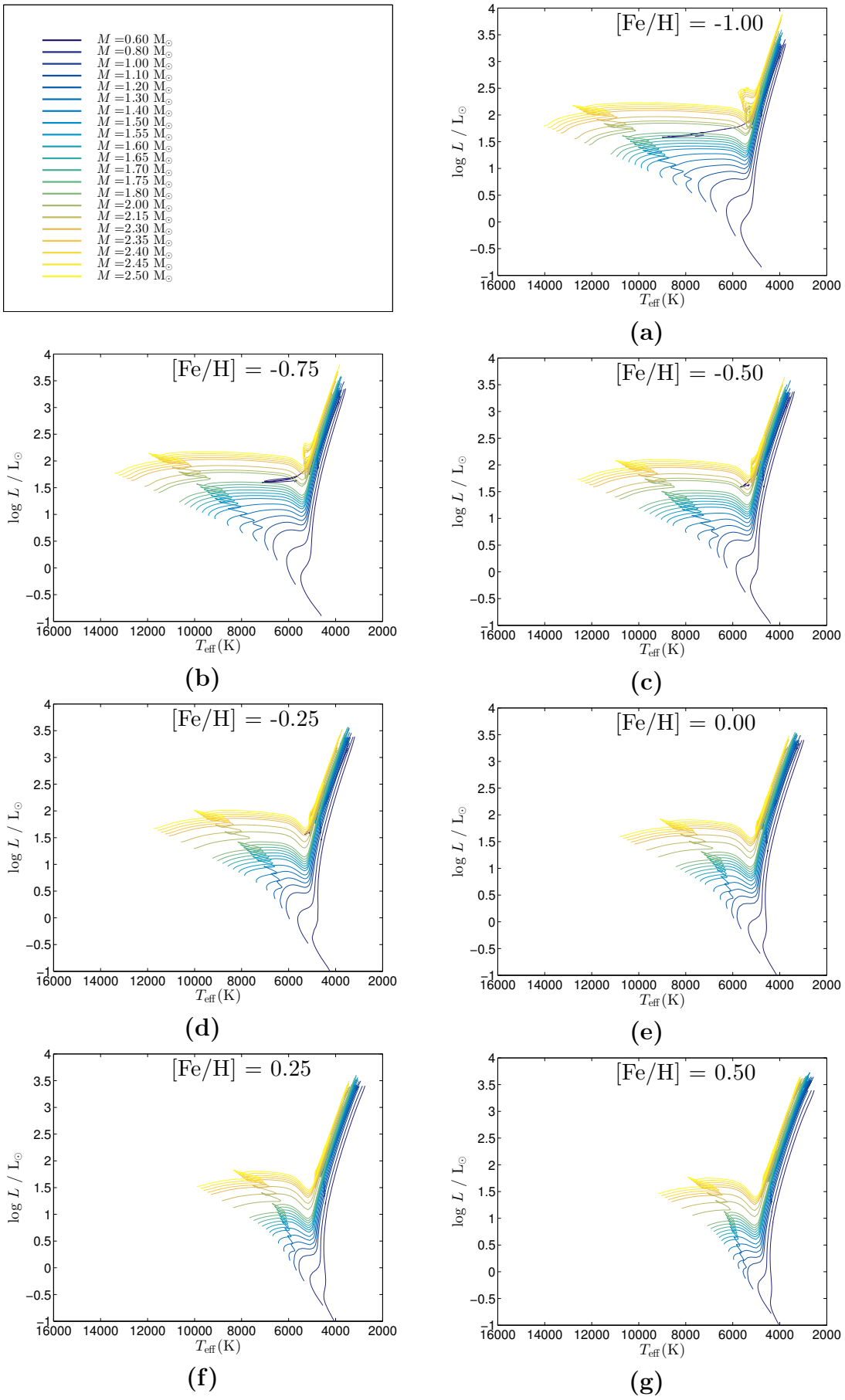


**Figure 3.8:** HRD for all the models computed

**Table 3.2:** Initial masses and chemical composition of the computed tracks

| Mass ($M_\odot$) | | |
|---|---|---|
| 0.60, 0.80, 1.00, 1.10, 1.20, 1.30, 1.40, 1.50, 1.60, 1.65, 1.70, 1.75, 1.80, 2.00, 2.15, 2.30, 2.35, 2.40, 2.45, 2.50 | | |
| [Fe/H] | $Z$ | $Y$ |
| −1.00 | 0.00176 | 0.25027 |
| −0.75 | 0.00312 | 0.25164 |
| −0.50 | 0.00555 | 0.25409 |
| −0.25 | 0.00987 | 0.25844 |
| 0.00 | 0.01756 | 0.26618 |
| 0.25 | 0.03123 | 0.27994 |
| 0.50 | 0.05553 | 0.30441 |

2. GYRE allows me to compute the oscillation spectra of the models, i.e., for instance, the adiabatic frequencies of oscillations, the mode inertias, and the radial and horizontal displacement profiles. In this section I will give an overview of the methods used in whis work in order to extract global seismic quantities from the models.

### 3.4.1 Average Large Separation

An important global property of the oscillation spectra, introduced in Chapter 2, is the large separation $\Delta\nu$. In a first approximation, $\Delta\nu$ can be estimated in the models by the equation 2.85. However, this estimate can be inaccurate, since is affected by a systematic effects which depend e.g. on the evolutionary phase and, more generally, on the how the sound speed behaves in the stellar interior. An improvement compared to using the scaling relation at face value requires to calculate the radial modes ($l = 0$) and then to average the frequency spacing between them. I refer to this quantity as the **average large separation**.

Observational measurements of the average $\Delta\nu$ are indeed limited by the frequencies around $\nu_{\rm max}$. Therefore, with the aim of a self-consistent comparison between data and models, any $<\Delta\nu>$ calculated from stellar oscillation codes must take in account the restrictions given by the observations. Handberg et al. (submitted, see appendix) estimated the quantity $\Delta\nu_{\rm fit}$ for the stars in the *Kepler*'s cluster NGC 6819. In that paper, we estimated $\Delta\nu_{\rm fit}$ by a simple linear fit of the individual frequencies (weighted on their errors) as function of the radial order. The value of the slope resulting from the fitting line gives the estimated $\Delta\nu$. However, the same method cannot be applied to theoretical models since their frequencies have no errorbars. I therefore needed to take in account the uncertainties associated to each frequency

in order to give them a consistent weight. Observational errors depend primarily on the frequency distance between a given oscillation mode and $\nu_{\max}$, with a trend that follows approximatively the inverse of a Gaussian envelope (smaller errors near $\nu_{\max}$, larger errors far away from $\nu_{\max}$, Handberg et al., submitted). For this reason I considered to use a Gaussian function described in Mosser et al. 2012a to calculate the individual weights.

$$w = e^{-\frac{(\nu-\nu_{\max})^2}{2\cdot\sigma^2}}, \tag{3.7}$$

where $w$ is the weight associated to the oscillation frequency $\nu$ and $\sigma$ is give by eq. 2.84. I then explored five alternative ways to calculate $<\Delta\nu>$ using Gaussian weights. The methods, here described, are visually explained in figure 3.9:

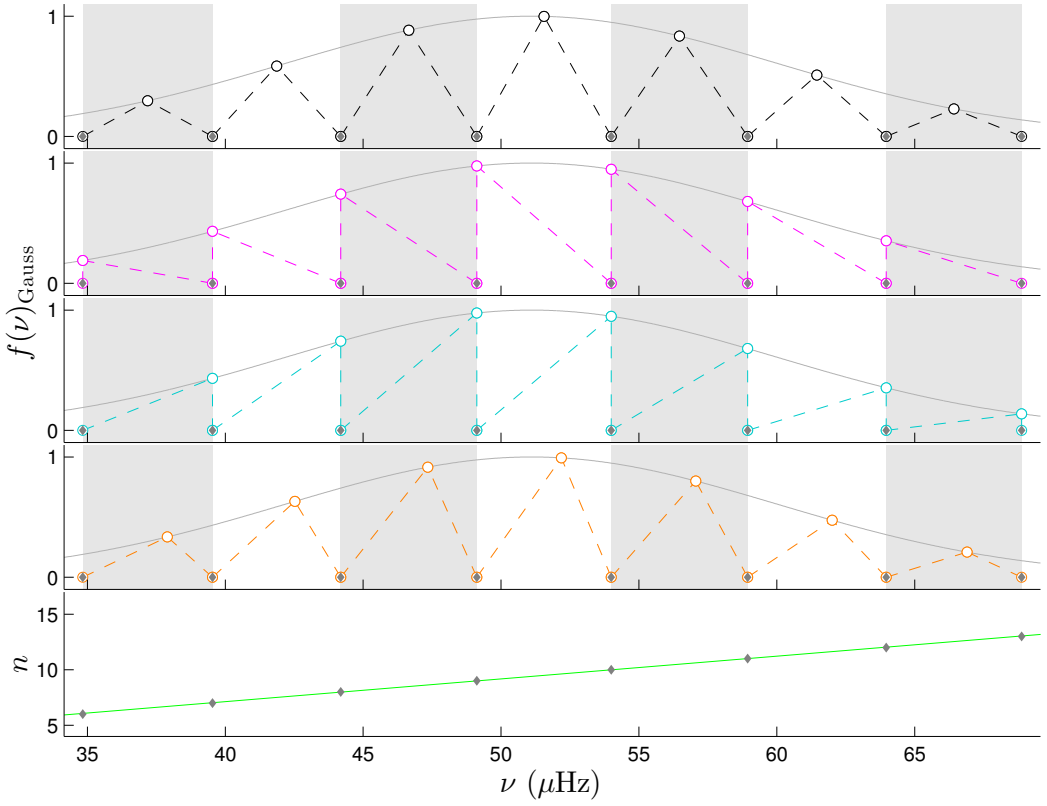


**Figure 3.9:** Schematic overview of the method proposed to calculate the average large separation in the models. From the top to the bottom, the five panels correspond to the methods described in section 3.4.1 and presented in the same order.

1. Mean of $\Delta\nu_{(n,n+1),0}$ $(\nu_{n+1,0} - \nu_{n,0})$, taking the weight at the middle point of every $l = 0$ interval (figure 3.9, panel 1).

2. Mean of $\Delta\nu_{(n,n+1),0}$, taking the weight at the start of every $l = 0$ interval (figure 3.9, panel 2).

**3.** Mean of $\Delta\nu_{(n,n+1),0}$, taking the weight at the end of every $l = 0$ interval (figure 3.9, panel 3).

**4.** Mean of $\Delta\nu_{(n,n+1),0}$, taking the weight as the mean value of the Gaussian function in every $l = 0$ interval (figure 3.9, panel 4).

**5.** linear fitting of $\nu_{n,0}$ as function of the radial order $n$, with the weights taken at each $\nu_{n,0}$ frequency (figure 3.9, panel 5).

In order to test my estimations I use the observed frequencies in Handberg et al. (submitted) simulating their errors using the Gaussian weight function in eq. 3.7. Figure 3.10 summarizes the comparison between $<\Delta\nu_{\rm gauss}>$, determined from the methods above, with $<\Delta\nu_{\rm fit}>$ estimated in the paper using the actual errors. The most compatible method (lower $\chi^2$) is **method 5** (linear fitting, green dots), which has also been used in the paper to calculate $<\Delta\nu_{\rm fit}>$. Nevertheless, all the methods estimate $<\Delta\nu_{\rm gauss}>$ with relative differences within the errorbars for the majority of the stars.
Although the definition of $<\Delta\nu>$ may seem a minor technical issue, it plays an important role in avoiding systematic effects on e.g. the mass and age estimates.

### Correction to the Scaling Relations

In Miglio et al. (2013b) the seismic quantities $\Delta\nu$ and $\nu_{\rm max}$ were introduced in the grid-based Bayesian tool PARAM (da Silva et al., 2006) to estimate global stellar properties of giants obserevd by CoRoT in two regions of the Galaxy. Rodrigues et al. (2014) used PARAM to calculate distances and extinction in the APOKASC sample (Pinsonneault et al. 2014). However, the asteroseismic quantities were calculated in the models by asteroseismic scaling relations, and are therefore affected by systematic uncertainties which may lead to inaccurate estimates of stellar properties. In order to improve on this issue, I worked to map the deviation between the scaling $\Delta\nu$ and the value calculated from individual frequencies (by the method described in section 3.4.1), extending the preliminary results presented in White et al. (2011) and, for red giants, in Miglio et al. (2012) and Miglio et al. (2013a). These papers have shown that corrections to $\Delta\nu$ scaling are evolutionary-state dependent and can affect the seismic estimation of mass to a level of $\sim 10\%$. It is therefore crucial to use $\Delta\nu$ from theoretical predicted frequencies to avoid (known) systematic biases in the mass and age estimation. To do so I used my grid of models in which I computed individual radial modes for each structure. Figures 3.11 and 3.12 show

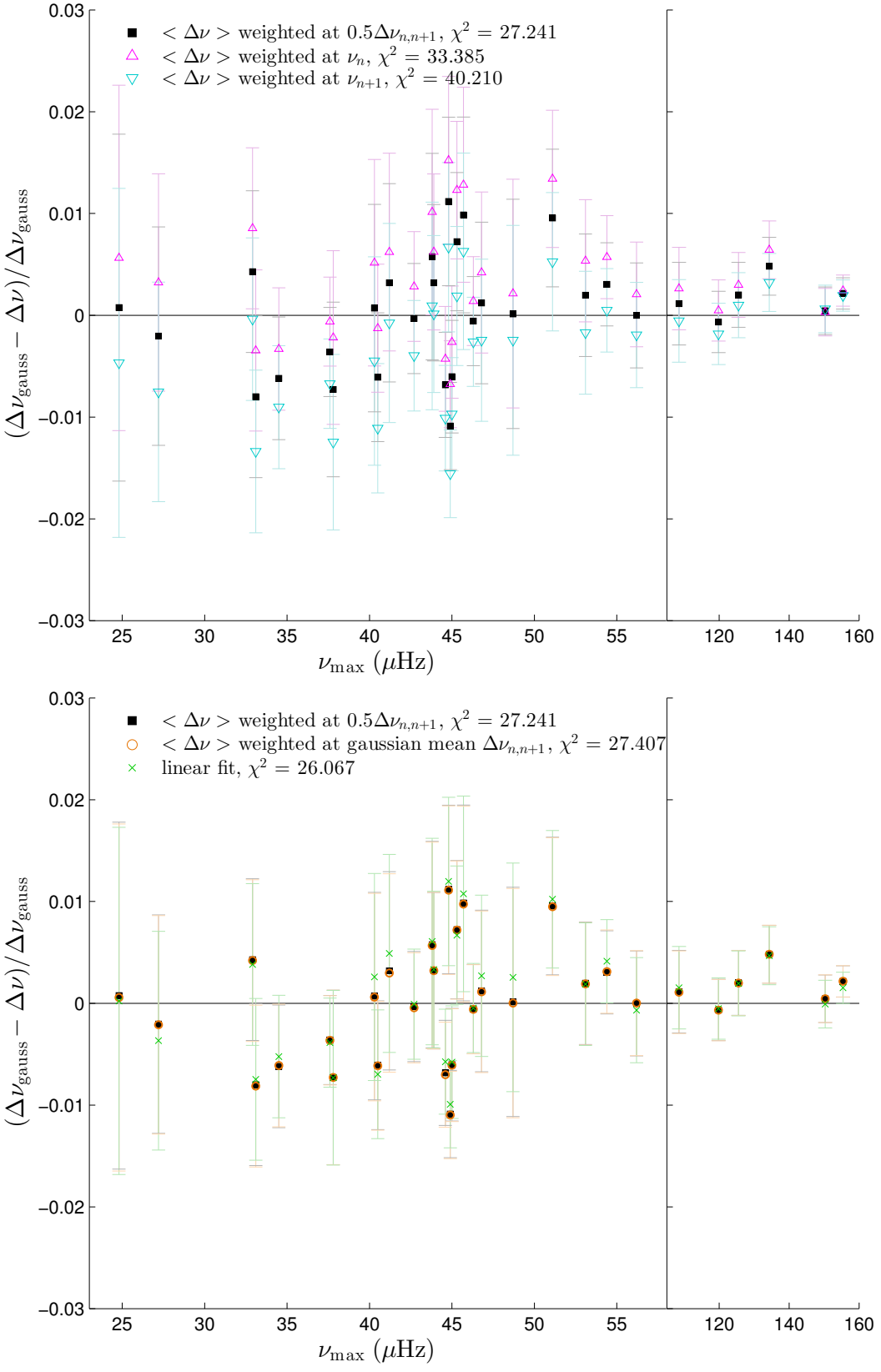


**Figure 3.10:** Comparison between the average large separation $<\Delta\nu_{\rm fit}>$ of the star in NGC 6819, estimated by linear fitting with the actual error, and the output of the five methods, described in section 3.4.1, for which the actual errors were substituted by a Gaussian function centred in $\nu_{\rm max}$.

the ratio between $\Delta\nu_{\rm scal.}$ and $<\Delta\nu>$ as a function of the effective temperature and $\nu_{\rm max}$ for a large number of tracks in the grid.

As is well known current models suffer from an inaccurate description of near-surface layers leading to a mismatch between theoretically predicted and observed oscillation frequencies. These so-called surface effects have a sizeable impact also on the large frequency separation, and on its average value. When utilising model-predicted $\Delta\nu$ it is therefore needed to correct for such effects. As usually done, a first attempt at correcting is to use the Sun as a reference, hence by normalising the $\Delta\nu$ of a solar-calibrated model with the observed one.

A comparison between the large frequency separation of the calibrated solar model belonging to the grid ($M$ = 1.0 $\rm M_{\odot}$, [Fe/H] = 0 at $\tau_{\odot}$ = 4.57 Gyr) and that from solar oscillation frequencies (Broomhall et al., 2014) is shown in Fig. 3.13. The predicted average large separation ($\Delta\nu_{\rm mod}$ = 136.1 $\mu$Hz) is 0.8 % larger than the observed one ($\Delta\nu_{\rm obs}$ = 135.0 $\mu$Hz). Tracks shown in figure 3.11 and 3.12 have been already corrected by surface effects.

### 3.4.2 Examples of scaling relation correction

Two examples of the relevance of the corrections to scaling relations are given in Handberg et al. (submitted, in appendix) and Miglio et al. (2016, in appendix).

In both papers we proceeded as in Miglio et al. (2012) and estimated stellar masses by using several combinations of the available seismic and non-seismic constraints by scaling relations in these four forms:

$$\frac{M}{\rm M_{\odot}} \simeq \left(\frac{\nu_{\rm max}}{\nu_{\rm max,\odot}}\right)^{3}\left(\frac{\Delta\nu}{\Delta\nu_{\odot}}\right)^{-4}\left(\frac{T_{\rm eff}}{\rm T_{eff,\odot}}\right)^{3/2}, \tag{3.8}$$

$$\frac{M}{\rm M_{\odot}} \simeq \left(\frac{\Delta\nu}{\Delta\nu_{\odot}}\right)^{2}\left(\frac{L}{\rm L_{\odot}}\right)^{3/2}\left(\frac{T_{\rm eff}}{\rm T_{eff,\odot}}\right)^{-6}, \tag{3.9}$$

$$\frac{M}{\rm M_{\odot}} \simeq \left(\frac{\nu_{\rm max}}{\nu_{\rm max,\odot}}\right)\left(\frac{L}{\rm L_{\odot}}\right)\left(\frac{T_{\rm eff}}{\rm T_{eff,\odot}}\right)^{-7/2}, \tag{3.10}$$

$$\frac{M}{\rm M_{\odot}} \simeq \left(\frac{\nu_{\rm max}}{\nu_{\rm max,\odot}}\right)^{12/5}\left(\frac{\Delta\nu}{\Delta\nu_{\odot}}\right)^{-14/5}\left(\frac{T_{\rm eff}}{\rm T_{eff,\odot}}\right)^{3/10}. \tag{3.11}$$

In the first paper we applied the theoretical corrections to the scaling relation on the RGB stars and RC stars in NGC 6819 and we compared them to empirical ones calculated from our measurements by assuming the distance modulus to be $(m - M)_V$ = 12.42 and on a star-by-star basis adjusting $\Delta\nu$ until mass eq.3.10 and 3.11 (and therefore all four mass equations) yield the same mass (figure 3.14). The mean

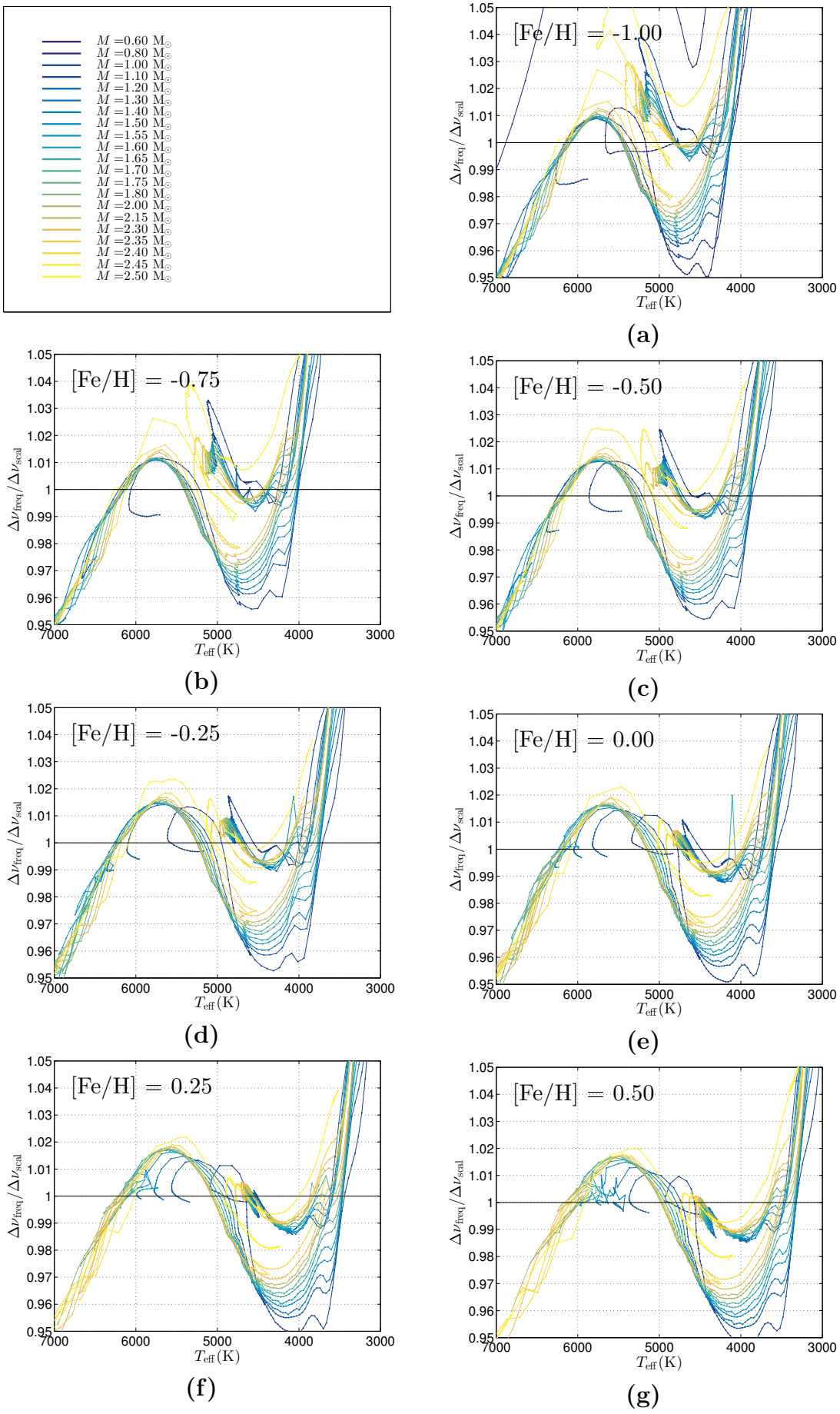


**Figure 3.11:** Correction of scaling relation in function of $T_{\rm eff}$

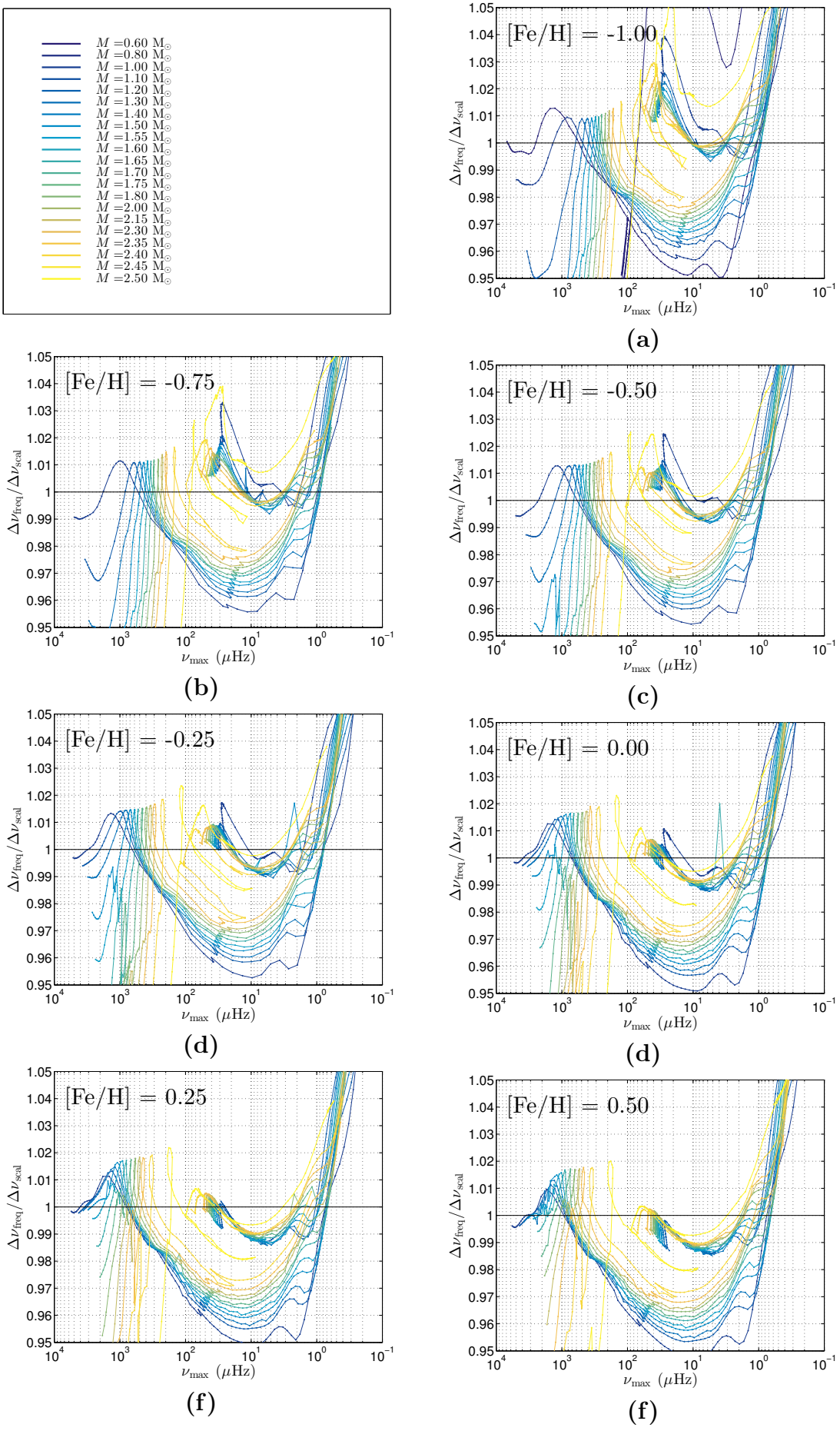


**Figure 3.12:** correction of $\Delta\nu$ in function of $\nu_{\rm max}$

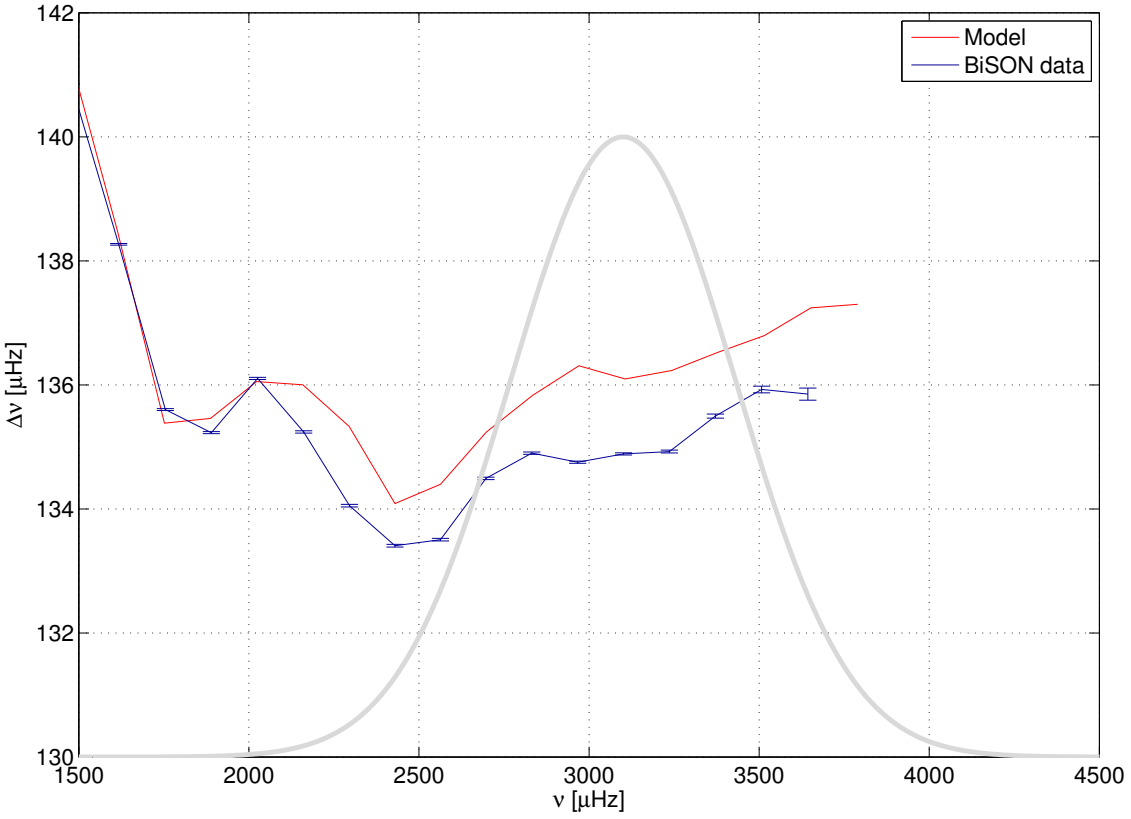


**Figure 3.13:** Comparison between calibrated solar model (red line) and that from solar oscillation frequencies (blue line, Broomhall et al., 2014). In grey the Gaussian function used to weight the frequencies of the solar model in order to calculate $<\Delta\nu>$.

mass of the red giants in NGC 6819 found to be $1.61 \pm 0.02\,M_\odot$ and $1.64 \pm 0.02\,M_\odot$, respectively, independent of whether empirical or theoretical corrections to $\Delta\nu$ were used. As seen, there is in general very good agreement between the theoretical and empirical correction with a scatter caused by errors in the measurements of $\Delta\nu$, $\nu_{\rm max}$, and $T_{\rm eff}$. The agreement strongly supports the theoretical corrections to $\Delta\nu$. This also suggests that no correction is needed for the other global parameter $\nu_{\rm max}$ (at least not at this metallicity). The fact that we are able, for the first time, to observationally confirm that the size of the $\Delta\nu$ correction changes with evolution up the RGB also shows that there is no significant evolutionary state dependent correction to $\nu_{\rm max}$ on the RGB. The agreement on the $\Delta\nu$ correction for both the RGB and RC phases also confirms that $\nu_{\rm max}$ should remain uncorrected, also for the RC phase of evolution. This confirms the result of Miglio et al. (2012) for $\Delta M$ between RGB and RC, but now with much higher confidence.

In the second paper we studied eight red giants (7 RGB and 1 HeCB stars) belonging to the globular cluster M4, observed by *Kepler* during the K2 campaign. The masses calculated for each star and for each scaling equation are shown in figure 3.15 (upper panel). To estimate a set of corrections we computed stellar models using MESA, taking an initial mass $M = 0.85\,M_\odot$ and heavy element abundance $Z = 0.003$ (obtained using the expression in Salaris, Chieffi & Straniero 1993, and the spectroscopically determined metallicity and alpha-enhancement from Marino et al. 2008). A Reimers' mass-loss efficiency parameter of $\eta = 0.2$ was also assumed. Our results suggest that the seven RGB stars with detected oscillations are in a $\nu_{\rm max}$ range where the mean density will be underestimated by 8% when strict adherence of the classic $\Delta\nu$ scaling is assumed. For the HeCB star (S8) the comparison suggests an overestimation of the mean density by $\sim 4\%$. If we apply these corrections to the mass determinations, we end up with a significantly lower scatter in the results (see 3.15, lower panel) for all RGB stars.

It can be noticed that the four measurements are scattered along the $M$ axis and present a systematic shift based on which equation was used. For example eq. 3.8 gives highest mass estimation, while than eq. 3.9 the lowest. We then apply the model predicted correction on the large separation, based on the difference between $\Delta\nu$ from scaling relation (eq. 2.85) and $< \Delta\nu >$ from computed frequencies (as described in section 3.4.1). The track taken in account for estimate the correction was a $M = 0.85\ M_\odot$ $Z = 0.003$. The results are shown in figure 3.15 (lower panel), where the scatter is substantially reduced.

For more details, both papers are presented in the appendix.

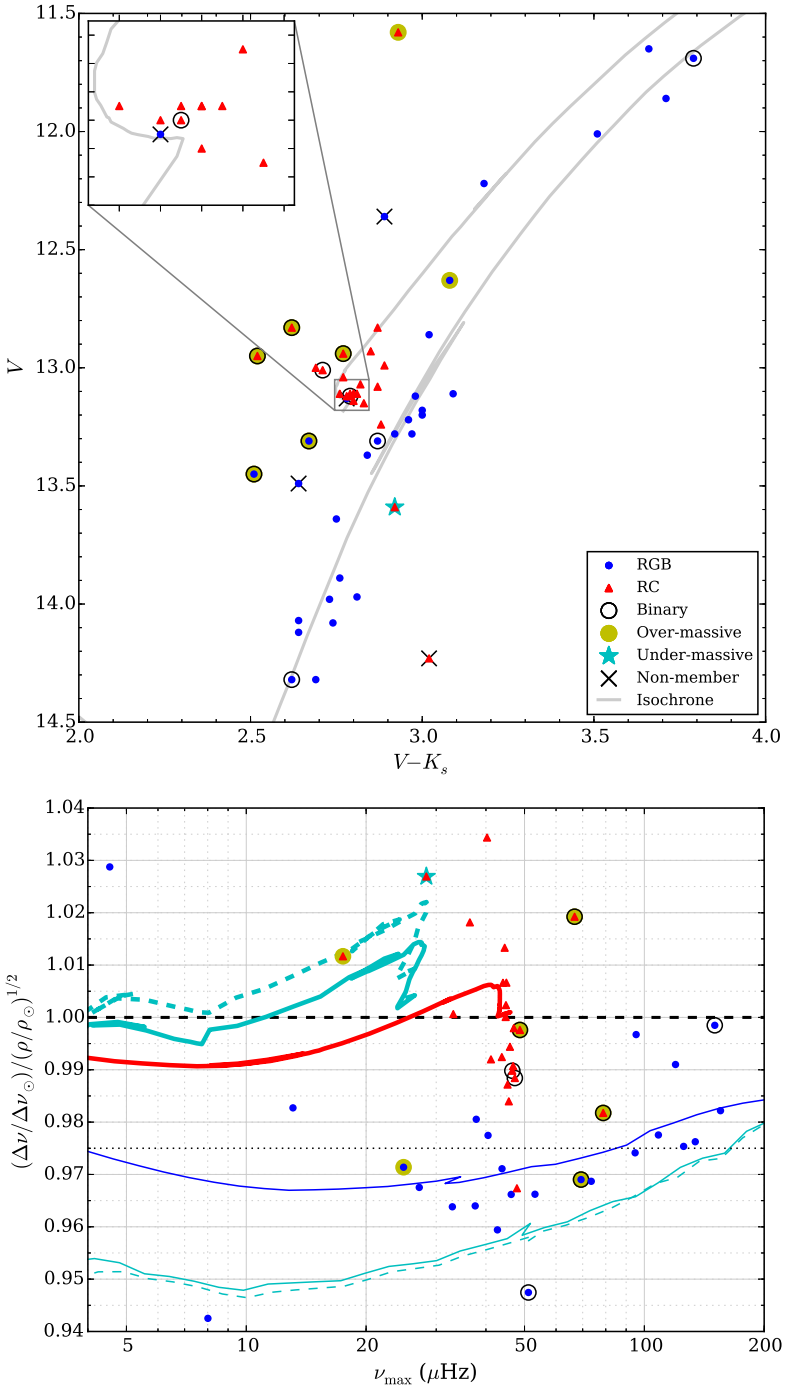


**Figure 3.14:** *Upper panel:* colour-magnitude diagram of the observed giants in NGC 6819. *Lower panel:* comparison between theoretical and empirical corrections to the scaling relation on the same giants.

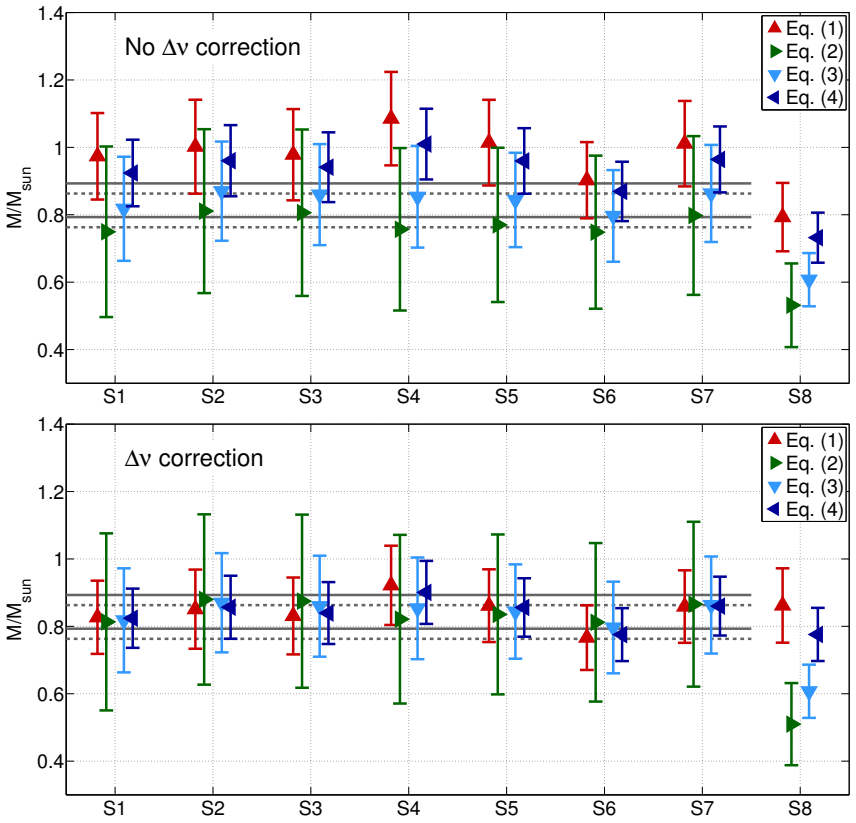


**Figure 3.15:** Mass of M4 giants as inferred from Eq. 3.8 to 3.11 (in order, Eq. 1 to Eq. 4) with (lower panel) and without (upper panel) applying a model-predicted correction to the $\Delta\nu$ scaling relation. The last star to the right (S8) is a HeCB star.

### 3.4.3 Small Separations

The small separation $\delta\nu_{01}$ and $\delta\nu_{02}$ are quantities that describe how the p-mode frequencies $l = 1$ and $l = 2$ differ from the first order asymptotic approximation. These quantities are defined as follows:

- $\delta\nu_{01}$ is the distance between the middle point of two consecutive radial $l = 0$ modes and the nominal $l = 1$ p-mode within the interval.
- $\delta\nu_{02}$ is the distance between the nominal $l = 2$ p-mode and the next $l = 0$ mode.

A visual illustration of $\delta\nu_{01}$ and $\delta\nu_{02}$ is presented in figure 3.16.
Estimating small separations does not require particular efforts in MS, since only p-modes show up in the spectra. On the other hand, models present many mixed modes along the RGB and simply selecting the modes at lower inertia (in $\Delta\nu$ interval) is not necessarily the best solution. Therefore, I need to design a specific method to extract from a spectrum of mixed modes the frequency locations that pure $l = 1$ and $l = 2$ p modes would have. Since the final goal is compare theoretical models

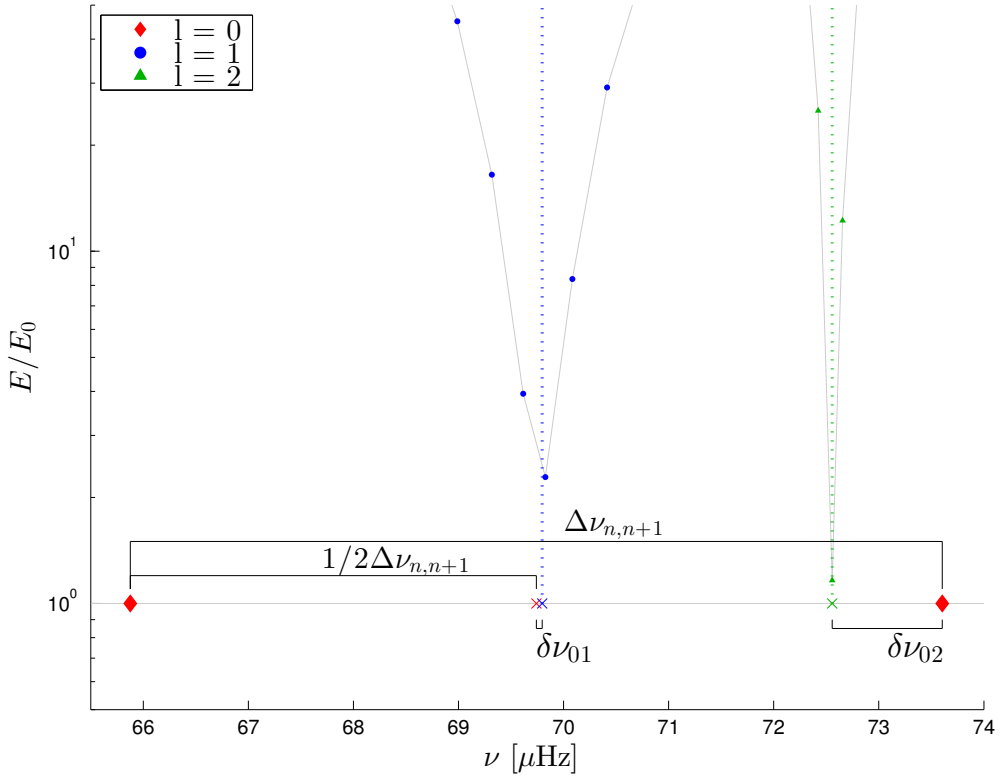


**Figure 3.16:** Definition of $\delta\nu_{01}$ and $\delta\nu_{02}$Ṅormalised inertia is shown as a funtion of the frequenies

with observational data, I limit the interval of frequencies around $\nu_{\max} \pm 3\sigma$, where $\sigma$ indicates the estimated size of the Gaussian envelope as described in Mosser et al. (2012a) and eq. 2.84.

The stellar track I use in this test is a $1.6 M_\odot$, solar composition from the ZAMS to the TP-AGB, for which I calculate the individual frequencies for several models (Figure 3.17). For the sake of simplicity, I focus on $l = 2$ frequencies of model number 41 (figure 3.18 ). The discussion can be easily transferred to other models and angular degrees. The first step is to normalize the inertia of the $l = 2$ modes with the inertia of the $l = 0$ modes. I fit the $l = 0$ mode inertia with a spline, then I use the function found to normalize the inertia of the $l = 2$ ($E_{20}$).

**method 0: minimum of inertia** I consider all the $l = 2$ frequencies in interval between two consecutive $l = 0$ modes ($\Delta I_i$). For each interval I just pick the mode with the lowest inertia.

**method 1: local weighted mean around the minimum of inertia** I re-define the interval $\Delta I_i$ taking the minimum of inertia $\pm\frac{1}{4}\Delta\nu$ and I calculate the

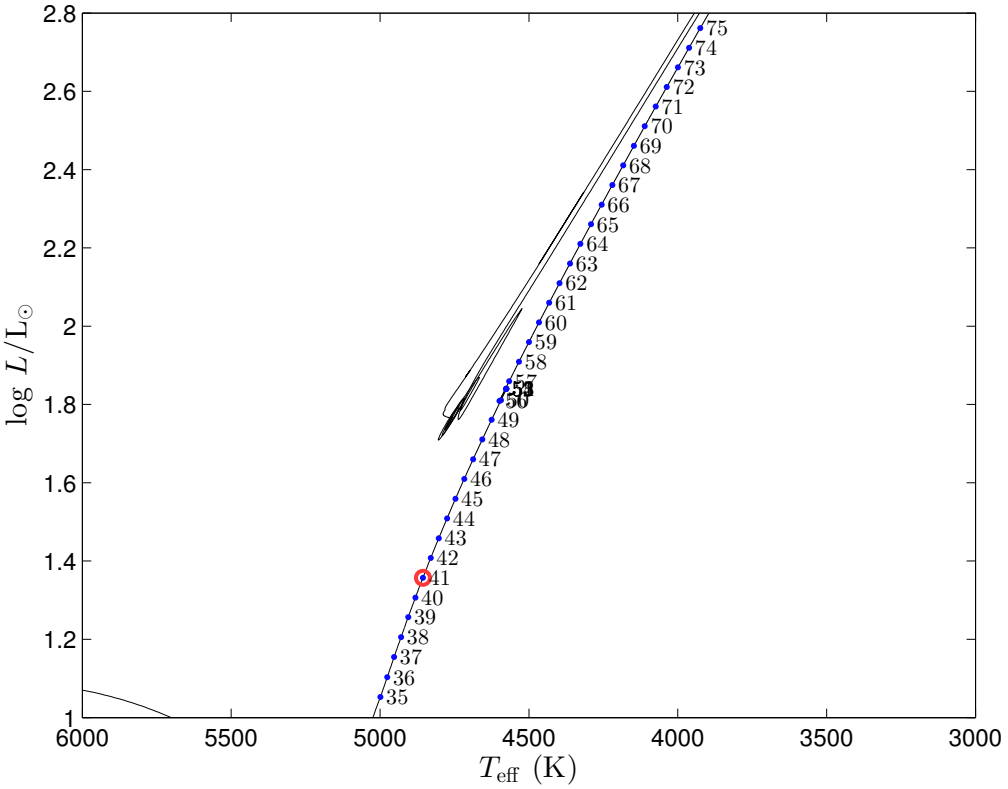


**Figure 3.17:** RGB of 1.6 $M_\odot$ solar composition on the HRD. The red dot indicates the test model used in the main text with the purpose of estimating $\delta_{02}$.

mean frequency weighted on the inverse of the normalized inertia:

$$\overline{\nu} = \frac{\sum \nu \cdot (E_{10})^{-1}}{\sum (E_{10})^{-1}}. \tag{3.12}$$

**method 2: local Lorentzian fitting around the minimum of inertia** According with Unno et al. (1989), the inertia of the mixed mode $l = 1, 2$ as a function of the mode frequency can be described by a Lorentzian function:

$$f_{\rm Lorentz} = \frac{a}{1 + \frac{4}{b^2} \cdot (x - c)^2}, \tag{3.13}$$

with $a$, $b$, and $c$ free parameters. Using the same intervals as in the previous method I fit $f_{\rm Lorentz}$ to the frequencies and the inverse of inertia. The nominal p-mode will be the central value of the function.

Figure 3.19 shows results of using the three methods on model 41, applied order by order. The dashed lines indicate the solutions of method 0 (blue) and 1 (red), while the green lines are the Lorentzian fits and their central peaks (method 2). The fourth panel of figure 3.18 summarizes the results found as a function of the

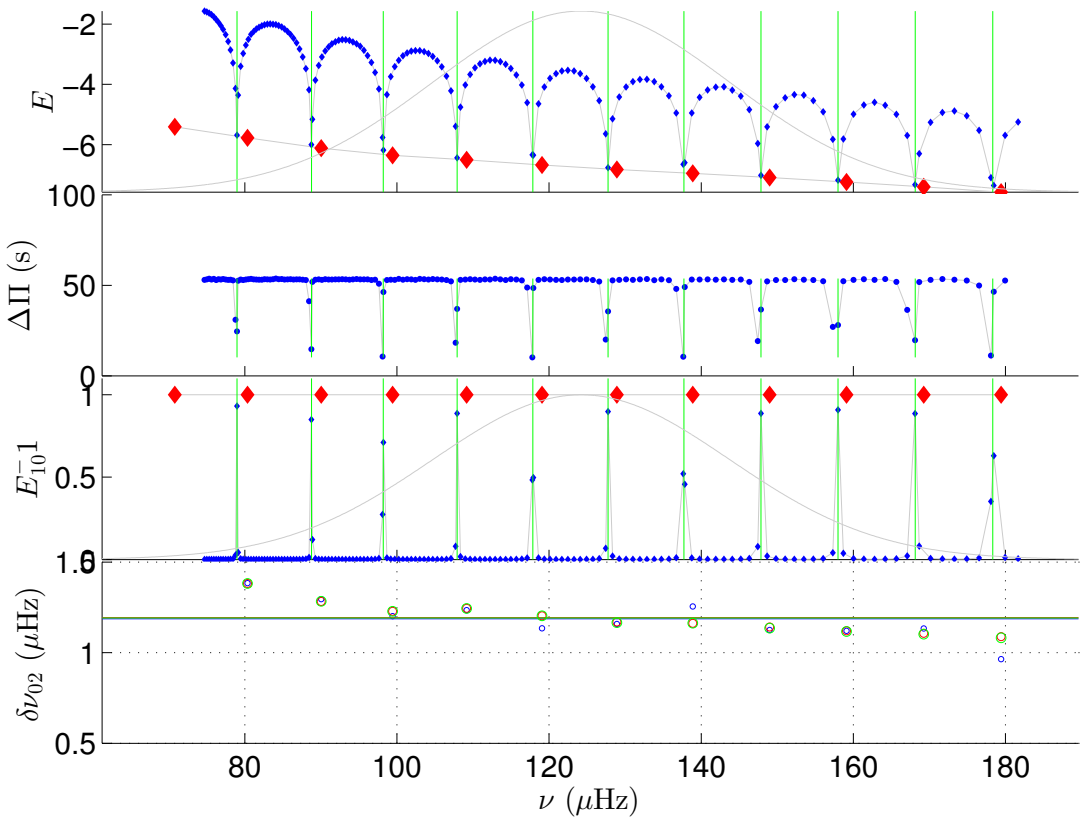


**Figure 3.18:** l=2 frequencies of model 41. *top panel:* log inertia against frequency. *second panel:* period spacing against frequency. *second panel:* period spacing against frequency. *third panel:* $l = 0$-normalized inertia against frequency. *bottom panel:* $\delta_{02}$ of the individual orders against the radial modes. The green vertical lines indicate the location of the nominal $l = 2$ p-like modes estimated by the method 2 described in the main text.

frequency of modes $l = 0$ (the solid lines represent the mean value found for each method). As a side note, it is important to point out the case of SGB stars, where the first mixed modes start to appear but are relatively few, typically less than 4 per order. In this case, fitting the inertia with functions having many parameters, like the Lorentzian function, is not possible and we therefore preferred to use the mean value with a weight that depends on the inertia of the modes. Alternative approaches like Benomar et al. (2015) are better suited in these cases.

Finally, to estimate the average small separation, it is not possible to adopt a linear fit as for $\Delta\nu$. The proposed method here simply consists in calculating the differences radial order by radial order and to define $<\delta\nu_{02}>$ as the average $\delta\nu_{02}(n)$ weighted by a Gaussian function taken at the $l = 2$ p-like modes. These weights have also been determined by comparison with typical observational uncertainties as derived in Handberg et al. (submitted).

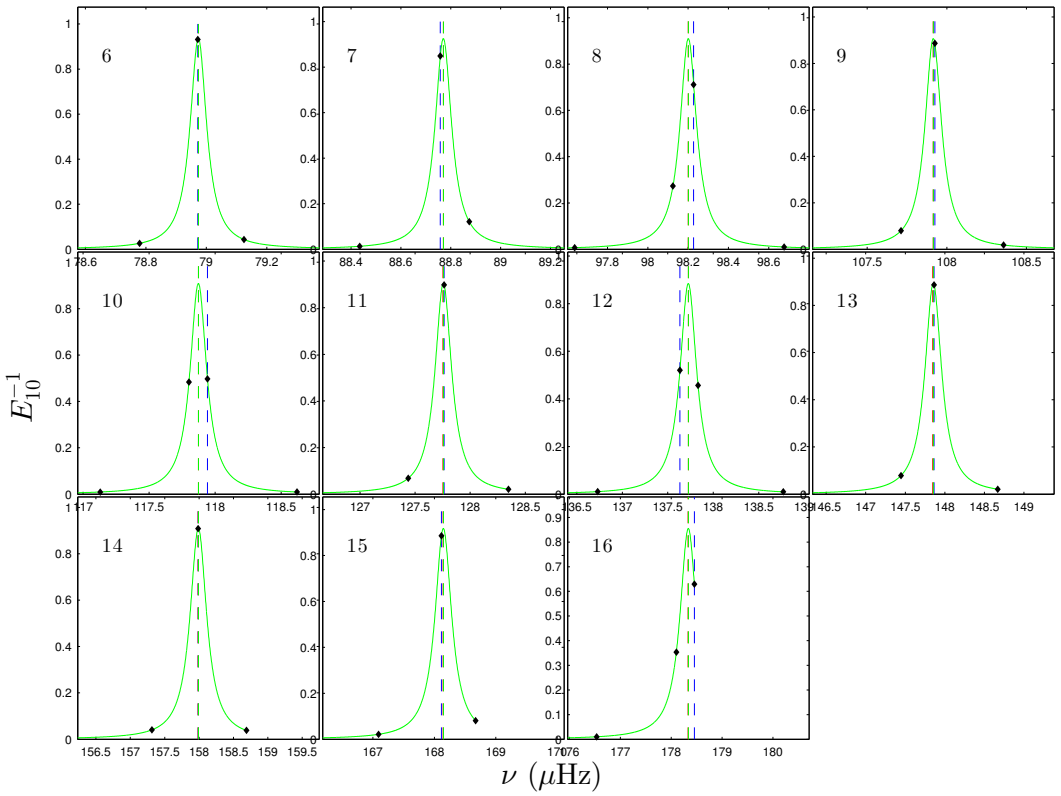


**Figure 3.19:** Identification of the nominal $l = 2$ p modes of different radial orders. The dashed lines indicate the solutions of method 0 (blue) and 1 (red), while the green lines show the Lorentzian fit and the location of their central peak (method 2). For the model considered, many orders have the three solutions very close together.

### 3.4.4 Small separations in NGC 6819

As an example of an application of the work presented in the previous section, I show here the preliminary results of the model-data comparison performed in Handberg et al. (submitted). In this paper we extracted the individual frequencies from the power spectra of about 50 NGC 6819 red giants. The stars were observed by *Kepler* in a timespan of 3.5 years. These frequencies were then used to estimate the average large and small separations for each star. In this context I contributed to generating the stellar models specific for the cluster. One of my evolutionary tracks has been already presented in figure 3.17 ($M = 1.60$ M$_\odot$, [Fe/H] $= 0$). I then estimated $\Delta\nu$ (using the linear fitting, method 5 section 3.4.1) and $\delta\nu_{02}$ (using the Lorentzian fitting, method 2 section 3.4.3 ) for a series of models along the RGB and in the RC phase, in order to reconstruct the track on the $\Delta\nu$-$\delta\nu_{02}$ plane. Figure 3.20 shows the comparison between my model and the observations. It can be noticed that the majority of the stars observed are compatible within $1\sigma$ to the stellar track, showing an excellent agreement also in the red clump.

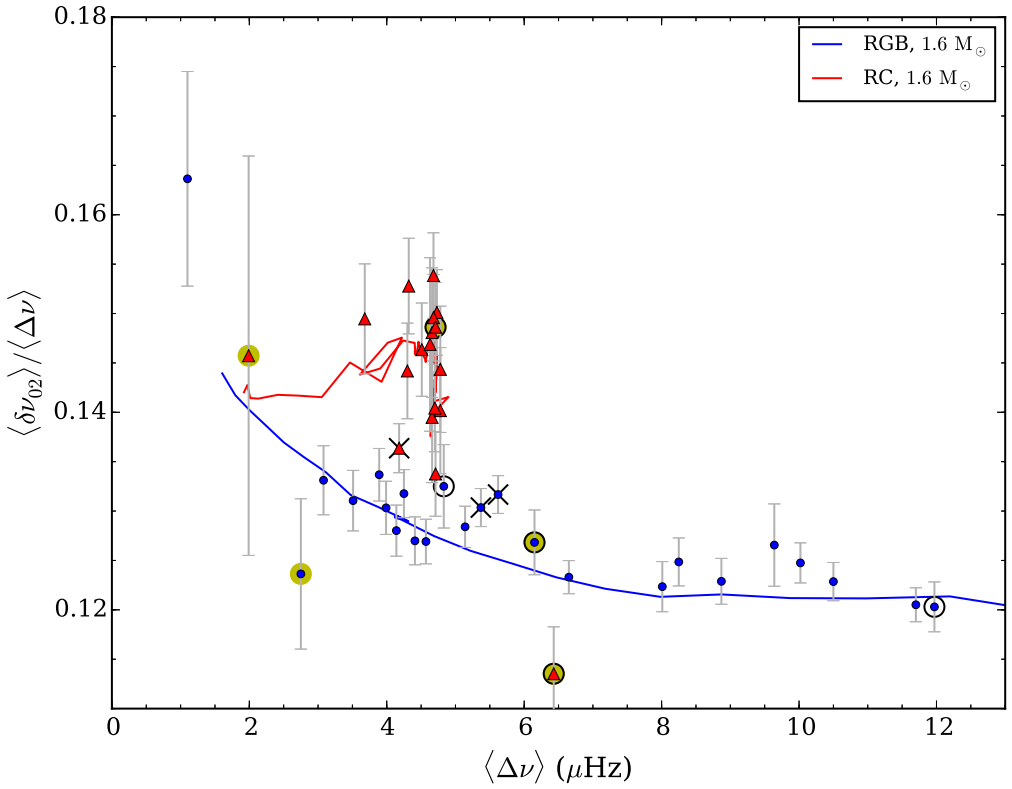


**Figure 3.20:** Small separation $\delta\nu_{02}$ against large separation of red giants in NGC 6819 cluster. The lines correspond to a $M = 1.60$ $M_\odot$, [Fe/H] $= 0$ evolutionary track. The stars observed are compatible within $1\sigma$ to the stellar track.

# Chapter 4

# Uncertainties on Near-Core Mixing in Red-Clump Stars

This chapter will report the effects of different mixing schemes during the HeCB phase on classical and seismic observables. The text presented here is taken from Bossini et al. (2015).
In the context of the paper, I computed various stellar models with different mixing treatments during the HeCB phase and I studied how they affect the predictions of observable parameters, such as the luminosity of the AGB bump and the period spacing of gravity modes. I then compared my theoretical models with observed stars in order to outline the characteristics of a mixing scheme able to describe both the parameters. Teramo and Padova stellar groups gave a large contribution providing me additional models to analyse from their evolutionary codes (BaSTI and PARSEC).

## 4.1 Observational constraints on helium-core-burning models

One of the main observables used to constrain the mass of the fully mixed core during the HeCB phase is the $R_2$ ratio (Buonanno, Corsi & Fusi Pecci, 1985). $R_2$ is defined as the ratio between the number of early Asymptotic Giant Branch (eAGB) Horizontal Branch (HB) stars in simple stellar populations (chemically homogeneous and coeval stars) and is directly connected to the lifetime of the two phases ($R_2 \sim \tau_{\rm AGB}/\tau_{\rm HB}$). The value of $R_2$ is affected by the core mixing during the HeCB phase, as discussed in, e.g., Bressan, Bertelli & Chiosi (1986), Caputo et al. (1989). The use of $R_2$ has hitherto been limited to stars in clusters, due to the small number of

field stars with accurate distance available, and due to the inherent complication of dealing with an ensemble of stars with a spread in age and chemical composition (which also hampers robust inferences on their evolutionary state).

Another important observable related to the HeCB and AGB evolution of low- and intermediate-mass stars is the luminosity of the AGB bump (AGBb, see e.g. the review by Catelan 2007). Similarly to the bump in RGB, the AGBb is a feature of the eAGB that consists in three passages of the evolutionary track in a small interval of luminosity and causes a local increment of stars in the luminosity distribution of a stellar population. The occurrence of the AGB bump is connected to the formation of the helium-burning shell (see e.g. Cassisi & Salaris 2013, paragraph 5.2). The luminosity at which it occurs depends on the location in mass of the He shell at its ignition, hence it is determined by the maximum extension of the mixed core during the HeCB phase. While the AGB bump had been highlighted in stellar evolutionary tracks a few decades ago (see, for instance Caputo, Castellani & Wood, 1978), its first identification as a distinct observational feature in galaxies was reported by Gallart (1998). The AGBb is nowadays observed in a large number clusters and nearby galaxies (e.g., see Alcock et al., 1997; Ferraro et al., 1999; Beccari et al., 2006; Dalcanton et al., 2012). A further important property of the AGBb is the weak dependence of the luminosity ratio between the RC and the AGBb on the metallicity and initial helium abundance (Castellani, Chieffi & Pulone 1991; Bono et al. 1995).

Asteroseismology of white dwarfs may also provide us with observational constraints to test models in the HeCB and AGB phase. The C/O profile of a white dwarf at the beginning of the cooling sequence corresponds to that of the stellar core at the end of the AGB, hence it is largely determined by the combined action of chemical mixing and nuclear burning during the HeCB phase. Using pulsation modes detected in WDs, Metcalfe, Salaris & Winget (2002) found a discrepancy in the central oxygen-to-carbon ratio between stellar models and the value inferred from seismic data. They ascribed this difference to an underestimation of $^{12}C(\alpha,\gamma)^{16}O$ cross section, however, as pointed out by Straniero et al. (2003), the final C/O ratio in models also depends on the amount of mixing applied in the convective regions beyond the Schwarzschild border, and on the adopted definition of such boundaries.

While providing valuable information, currently available tests cannot be used to discriminate competing models. In this chapter I propose a way forward, which is based on the combination of said constraints and the more direct diagnostics of the conditions in the core provided by non-radial modes observed in HeCB stars.

## 4.2 Stellar models

In my exploratory analysis I consider models with $M = 1.5$ $M_{\odot}$and solar chemical composition. This set of parameters are both typical of the sample of RC giants observed by *Kepler* (see e.g. Pinsonneault et al., 2014; Mosser et al., 2014), and similar to those of giants in the cluster NGC6819 (see Basu et al., 2011; Miglio et al., 2012; Sandquist et al., 2013). Models in HeCB phase are computed using three different stellar structure and evolution codes (MESA, BaSTI, and PARSEC) and several assumptions about near-core mixing.
A first set of models presented in this study is computed using the MESA. The choice of parameters and of the relevant physics is the one described in chaper 3: IP1 with Eddington-grey atmosphere.
I compute the following MESA models with different schemes for convective mixing:

**BS** The "bare Schwarzschild" model (BS, to follow the notation in Straniero et al. 2003).

**HOV** Step function overshooting model with high parameter value $\alpha_{\rm ovHe} = 1$ (HOV).

**HPC** Penetrative Convection model with a high overshooting parameter $\alpha_{\rm ovHe} = 1$ (HPC).
For low and moderate values of $\alpha_{\rm ovHe}$, overshooting models (as well as penetrative convection) might develop a semiconvective region similar to the case presented by Castellani, Giannone & Renzini (1971b). For high values of the overshooting parameter (e.g HOV and HPC) the extra mixed region becomes large enough to prevent the formation of a semiconvective region (see e.g. Bressan, Bertelli & Chiosi, 1986; Straniero et al., 2003). Moreover, in these cases the determination of the fully mixed region requires the application of the Schwarzschild criterion in layers where there is no chemical composition gradient/discontinuity, which greatly simplifies the numerical implementation of the convective-instability criterion.
In order to extend my study of the mixing-schemes commonly adopted, I also consider stellar models from other evolution codes (BaSTI and PARSEC). To compute those models I used, where possible, the same physical inputs adopted in MESA.

**BaSTI-SC** Collaborators provided me models computed with the BaSTI code (A Bag of Stellar Tracks and Isochrones, Pietrinferni et al., 2004, 2006, 2013). The BaSTI model has $M = 1.5$ $M_{\odot}$, computed for $Z = 0.0176$, $Y = 0.266$, and

$\alpha_{\rm MLT}$ = 1.69 with Grevesse & Noels (1993) heavy element partition. The input physics relevant to this analysis is the same as in the MESA calculations but for the $^{12}C(\alpha,\gamma)^{16}O$ reaction rate that comes from Kunz et al. (2002). Core mixing during the HeCB stage, induced overshooting and semiconvection have been taken into account by adopting the numerical scheme firstly introduced by Castellani et al. (1985) and previously described. Indeed, a semiconvective region starts to appear when the central abundance by mass of He is $\sim 0.7$. The occurrence of breathing pulses - which appear when the central abundance of He drops below of 0.12 - is inhibited by imposing that the abundance of Helium in the core is not allowed to increase at each time step. The evolution starts from the pre-main sequence to the RGB-tip, and is resumed at the start of the HeCB after the core electron degeneracy has been removed (the helium-flash evolution is not computed), and 3% of carbon has been produced during the He-flash. No core convective overshoot during the central H-burning stage and no mass loss during the RGB phase are taken in account.

**PARSEC-LOV** Models computed using PARSEC (PAdova & TRieste Stellar Evolution Code, Bressan et al., 2012, 2013) are also considered for $M$ = 1.5 $M_\odot$, $Z$ = 0.017, and $Y$ = 0.279. I briefly summarize below the main input physics adopted for the current models. The nuclear reaction rates and corresponding $Q$-values are the recommended values in the JINA reaclib database (Cyburt et al., 2010). The high-temperature opacities, $4.2 \leq \log(T/\mathrm{K}) \leq 8.7$, are provided by the Opacity Project At Livermore (OPAL) team (Iglesias & Rogers, 1996, and references therein) and the low-temperature opacities, $3.2 \leq \log(T/\mathrm{K}) \leq 4.1$, are from ÆSOPUS[1] tool (Marigo & Aringer, 2009). The equation of state is computed with the FreeEOS code (A.W. Irwin[2]). The heavy element partition is from Caffau et al. (2011). The MLT parameter, $\alpha_{\rm MLT} = 1.74$, is calibrated on the solar model accounting for element diffusion. The standard mixing scheme in PARSEC considers an overshooting parameter of $\Lambda_c = 0.5$ across the formal Schwarzschild border, which means about $0.25H_p$ above it, and a radiative thermal stratification of the extra-mixed region. Similar to BaSTI, the evolution starts from the pre-main sequence, stops at the helium flash and restarts after the core electron degeneracy has been removed after the flash. The amount of carbon consumed to remove the electron degeneracy is computed from the variation of the gravitational binding energy of the core during the flash. During the HeCB phase, besides accounting for core over-

[1] http://stev.oapd.inaf.it/aesopus
[2] http://freeeos.sourceforge.net/

shooting, the code may deal with residual semi-convective instabilities using the Schwarzschild criterion, and suppresses possible breathing pulses of convection.

**PARSEC-MPC** PARSEC developers also provided me a modified track in which the mixed He core is extended by penetrative convection (adiabatic stratification) with a moderate value of overshooting ($\Lambda_c = 1.0$, i.e. $\alpha_{\rm ovHe} \sim 0.5$).

**ES** Finally, I include in the analysis a model obtained with MESA computed with an external routine to implement a similar prescription as in BaSTI-SC (see section 3.2.2)

## 4.3 Predicted stellar properties of models in the HeCB and AGB phase

I now compare the properties of the series of models presented in Section 4.2, with particular emphasis on those which can be tested via a direct comparisons to observations. I start by comparing predictions of non-seismic observables (see Sec. 4.1), while in Sec. 4.3.3 I focus on seismic diagnostics.

The main consequence of applying different mixing schemes in the HeCB phase is to vary the core mass undergoing convective mixing. I refer to **convective-core mass** ($M_{\rm cc}$) as the core mass in which $\nabla_{\rm rad} \geq \nabla_{\rm ad}$ (formal Schwarzschild core), while the **mixed-core mass** ($M_{\rm mc}$) includes also the extra-mixing region (e.g convective core + overshooting and/or semiconvection). The mixed-core mass also indicates the location in the stellar structure of the discontinuity in the chemical composition due to HeCB. In the ES models (in the domain I was able to explore) and BS models, $M_{\rm cc}$ corresponds to $M_{\rm mc}$ since no extra mixing is introduced. This is also true for the BaSTI-SC model when $Y_c > 0.7$, i.e. where semiconvection has not appeared yet, and during the last stages of the HeCB, where the convective core grows rapidly and the size of the semiconvective region is reduced (see Figure 4.1, upper panel). In HOV, HPC, PARSEC-LOV, and PARSEC-MPC, $M_{\rm cc}$ and $M_{\rm mc}$ are distinct from the beginning to the end of the HeCB phase (Figure 4.1, upper and middle panels). Although penetrative convection models are expected to have smaller $M_{\rm cc}$ and $M_{\rm mc}$ than overshooting models (see Godart, 2007; Noels et al., 2010, in the case of massive main-sequence stars), $\max(M_{\rm mc})$ in HOV and HPC is very similar, providing a similar $L_{\rm AGBb}$ (see Figure 4.1, upper and lower panels).

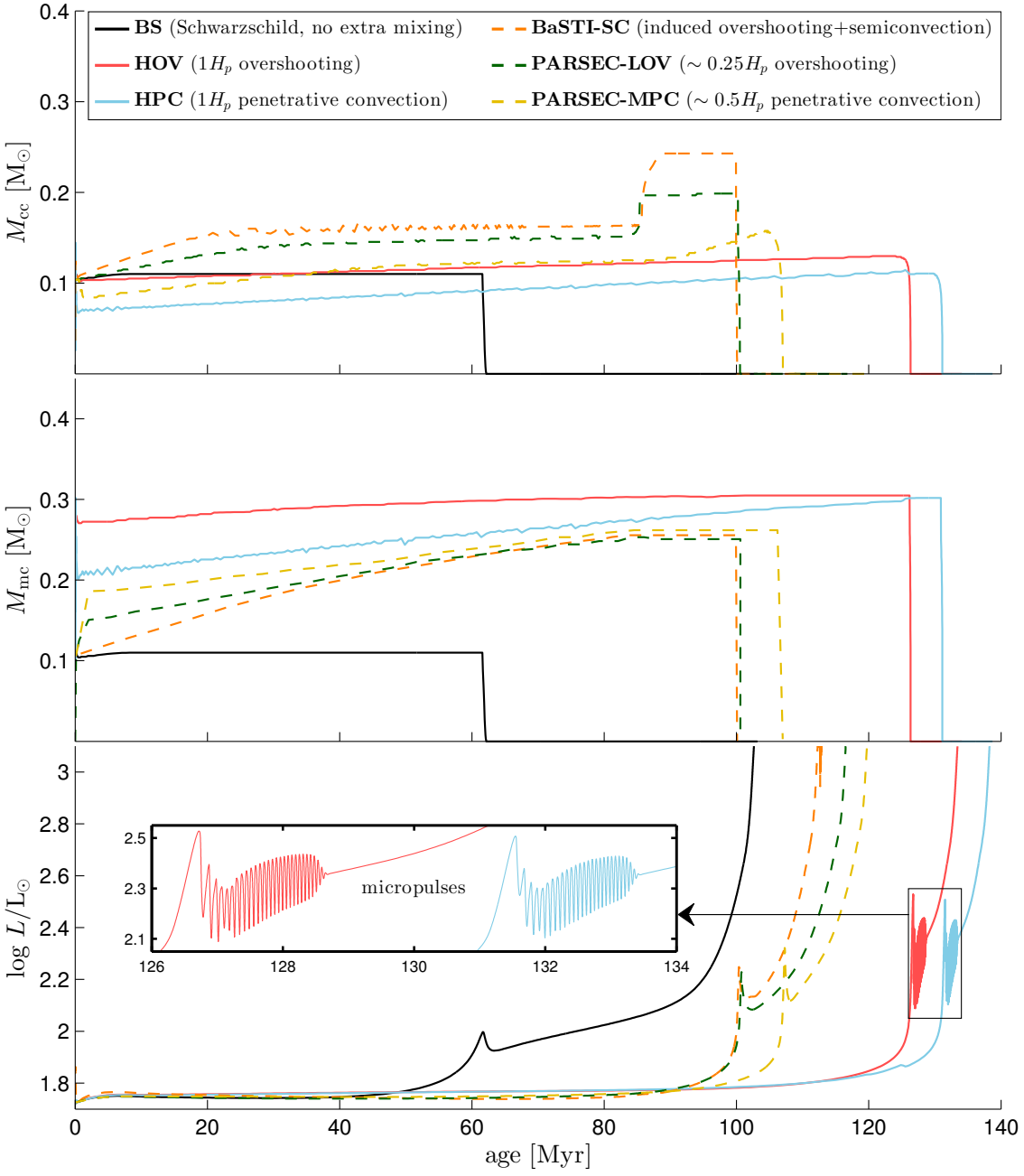


**Figure 4.1:** Convective-core (upper panel), mixed-core mass (middle panel) and total luminosity (lower panel) as a function of time for the BS, HOV, HPC, BaSTI-SC, PARSEC-LOV, and PARSEC-MPC models from the start of the HeCB phase up to the first AGB-TP. Both HPC and HOV models show micropulses.

### 4.3.1 Luminosity and duration of the HeCB and eAGB phases

An obvious effect of increasing $M_{\rm mc}$ is to increase the duration of the HeCB phase ($\tau_{\rm HeCB}$). In models with larger $M_{\rm mc}$ more fuel is available for the triple-$\alpha$ and $^{12}$C($\alpha$,$\gamma$)$^{16}$O nuclear reactions, increasing the time necessary to deplete all the helium in the core, i.e. the lifetime of the HeCB phase. In HOV and HPC models, the HeCB lifetime increases by about 40% compared to the BS model, while in BaSTI-SC and PARSEC-LOV by about 20%. However, if we look at the lifespans of the single phases, the increase in duration of the HeCB phase corresponds to a (non-linearly proportional) decrease of the duration of the AGB phase, since the formation of the He shell takes place closer to the H shell. The BS model has shorter lifetime with respect to the HPC and HOV models, however, it has a longer AGB phase. The BaSTI-SC, PARSEC-LOV, and PARSEC-MPC tracks have a behaviour which is in between the BS and the HPC/HOV models. In general we expect that models with increasing $M_{\rm mc}$ produce a longer HeCB phase and a less populated early-AGB, combined with a decreasing $R_2$ factor from BS models to the HOV and HPC models. These results are reported in Table 4.1.

The stellar luminosity is also affected by the mixing scheme adopted during HeCB (Figure 4.1, lower panel), and $L_{\rm AGBb}$ increases when extra mixing is added, while it remains almost unchanged when comparing HOV and HPC tracks (Table 4.1). The maximum extension of $M_{\rm mc}$ (which is very similar in HOV and HPC models) corresponds to the inner border of the He-shell at its ignition and it determines the $L_{\rm AGBb}$.

Models with larger cores (HOV and HPC) show *micropulses* (Mazzitelli & D'Antona, 1986), i.e. a series of secular instabilities that may occur during the formation of the He-burning shell. Micropulses appear after the maximum in luminosity of the AGB bump if the nuclear reactions in the core stop before the shell is ignited in "thin" conditions (see Schwarzschild & Härm 1965). To support this statement I have looked at the central helium abundance and the nuclear energy generation rate at the start of the AGB bump. The values found indicate that in the HPC and HOV models the contribution of HeCB to the luminosity is negligible, since helium is almost completely depleted. On the other hand, in the BS model core-He burning still contributes significantly to the luminosity. I note that for micropulses to be resolved by a stellar evolution code, a small timestep is needed in the numerical simulations: each pulse lasts for about $5 \cdot 10^4$ yr and the duration of the entire phenomenon is about 2 million years.

The study of micropulses goes beyond the purpose of this thesis and for detailed

| | MESA BS | MESA HOV | MESA HPC | MESA ES | BaSTI SC | PARSEC LOV | PARSEC MPC |
|---|---|---|---|---|---|---|---|
| timespan HeCB phase ($\tau_{\rm HeCB}$) (Myr) | 60.4 | 126.2 | 131.1 | — | 100.2 | 100.6 | 107.0 |
| $R_2$ ratio ($\frac{\tau_{\rm AGB}}{\tau_{\rm HeCB}}$) | 0.71 | 0.06 | 0.06 | — | 0.12 | 0.15 | 0.12 |
| $M_{\rm cc}$ at $Y_c \sim 0.7$ ($M_\odot$) | 0.100 | 0.113 | 0.084 | 0.162 | 0.165 | 0.140 | 0.107 |
| $M_{\rm mc}$ at $Y_c \sim 0.7$ ($M_\odot$) | 0.100 | 0.292 | 0.242 | 0.162 | 0.165 | 0.187 | 0.206 |
| maximum extension $M_{\rm cc}$ ($M_\odot$) | 0.100 | 0.130 | 0.114 | — | 0.243 | 0.199 | 0.158 |
| maximum extension $M_{\rm mc}$ ($M_\odot$) | 0.100 | 0.305 | 0.302 | — | 0.243 | 0.251 | 0.262 |

**Table 4.1:** Non-seismic properties of 1.5 $M_\odot$ models computed adopting different mixing schemes. the empty enters

explanations I refer the reader to Mazzitelli & D'Antona (1986) and the more recent work by Gautschy & Althaus (2007). Also notable of citation are the papers by Bono et al. (1997) and Sweigart et al. (2000) where the connection between *"gravonuclear instabilities"* and micropulses is investigated.

### 4.3.2 Asymptotic gravity-mode period spacing

I have shown that there are no significant differences between models with similar $M_{\rm mc}$ when considering the luminosity as a function of time (see e.g. HOV and HPC in Fig. 4.1). These models, however, have very distinct seismic properties. Montalbán et al. (2013) showed that extending the adiabatically stratified central region leads to a larger value of the gravity-mode period spacing. The reason why the asymptotic period spacing of gravity modes ($\Delta\Pi_{\rm g}$) during the HeCB phase is a sensitive probe of the temperature stratification of near-core regions is directly related to the behaviour of the Brunt-Väisälä frequency $N$, and its relation with $\Delta\Pi_{\rm g}$.

In the stellar interior, $N$ depends on the local temperature and chemical composition gradients (eq. 2.35). In a fully mixed region, $\nabla_\mu$ is null, therefore the $N^2$ profile is directly proportional to the difference between $\nabla_T$ and $\nabla_{\rm ad}$ (Figure 4.3a).

In the extra-mixed region of models with overshooting (e.g. HOV and PARSEC-LOV) $\nabla_{\rm rad} < \nabla_{\rm ad}$, therefore

$$N^2 \propto \nabla_{\rm ad} - \nabla_T = \nabla_{\rm ad} - \nabla_{\rm rad} > 0,$$

while in the corresponding region of a penetrative convection model (e.g. HPC and PARSEC-MPC) $\nabla_T = \nabla_{\rm ad}$, hence

$$N^2 \propto \nabla_{\rm ad} - \nabla_T = 0.$$

The asymptotic period spacing of gravity modes is related to the Brunt-Väisälä fre-

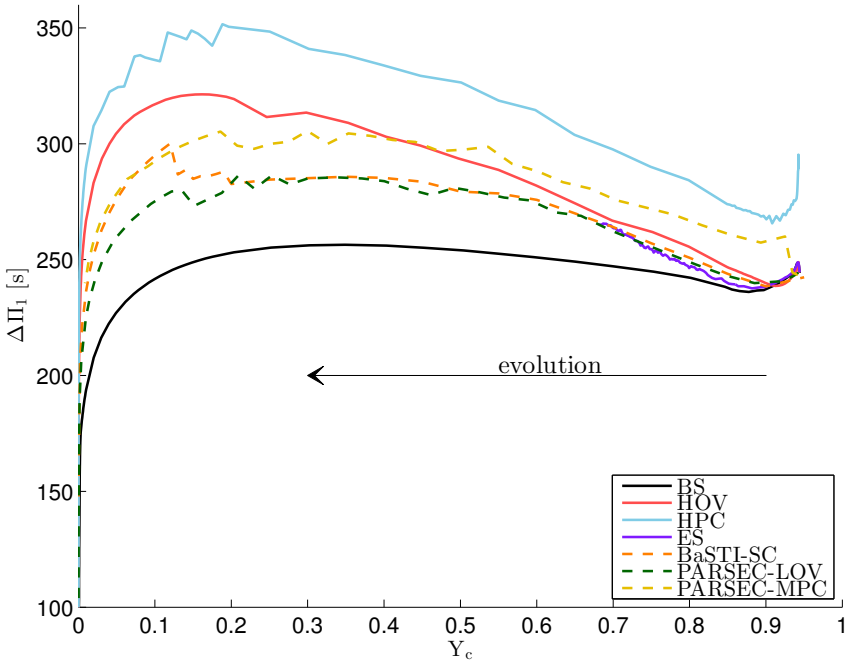


**Figure 4.2:** Period spacing against the central helium mass fraction during the HeCB phase for the model computed. Bare-Schwarzschild models present the smallest period spacing, while the penetrative convection models have the largest values. Moreover penetrative convective models start with larger period spacing.

quency according to the relation 2.78. Consequently, HeCB penetrative-convection models have higher values of $\Delta\Pi_g$ compared to overshooting models (Figure 4.2).

A similar effect can be found if I compare models with increased mixed-core size. Bare-Schwarzschild models, in fact, have lower $\Delta\Pi_g$ compared all other models, followed by models with induced overshooting (BaSTI-SC and ES), then high overshooting model, and finally high penetrative convection models (see Fig. 4.3a).

Independently from the convective-mixing scheme adopted (BS, HOV and HPC), the period spacing of models in the HeCB is higher compared to that on the RGB at the same luminosity ($\Delta\Pi_{g_{RGB}} \sim 60-50$ s), while after the early-AGB phase $\Delta\Pi_g$ decreases to similar or smaller values (Montalbán & Noels, 2013).

It is interesting to notice that if models present multiple gravity-mode cavities, we do not expect them to show a regular period spacing. This is the case of HOV and HPC models in the in the post-HeCB phase during the micropulses. In fact, the He shell can experience convection within each pulse, in conjunction with the maximum of the nuclear energy generation. Stars presenting this scenario (if any at all exist) may be missed by analysis based upon looking for a simple pattern in $\Delta\Pi_g$ (e.g. Mosser et al., 2012b).

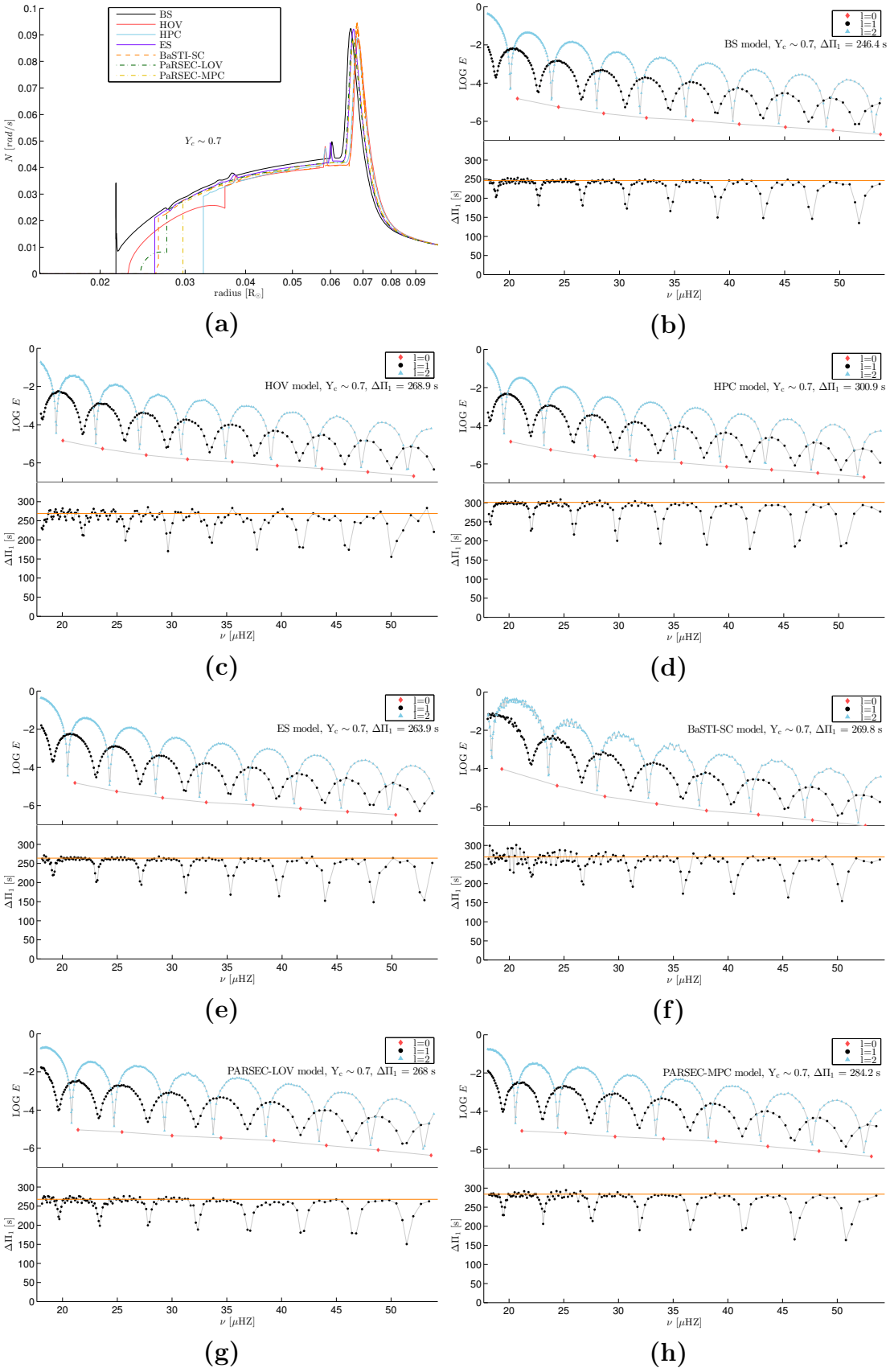


**Figure 4.3:** (a): Brunt-Väisälä frequency in the stellar interior of models with $Y_c \simeq 0.7$ and different convective-mixing scheme. Figures (b-h): Oscillation modes properties for the different convective schemes. *Upper panel:* mode inertia as a function of the frequency for modes with angular degree $\ell = 0, 1, 2$. *Lower panel:* period spacing of numerically computed dipolar-mode frequencies (dots) compared with the asymptotic value (solid orange line).

### 4.3.3 Period spacing of numerically computed adiabatic frequencies

From the observed frequency spectra we can estimate $\Delta\Pi_g$ based on the detection of modes that have relatively small inertias, i.e. gravity modes that have a significant coupling with the low-inertia acoustic modes (see e.g. Christensen-Dalsgaard 2012 and reference therein). The frequencies of these mixed gravito-acoustic modes are expected from theory to follow a relatively simple pattern (see e.g. Unno et al., 1989; Mosser et al., 2012b), which can be fitted to the observation to estimate $\Delta\Pi_g$, provided that a sufficient number of modes are detected, and that the analytical approximation for the expected pattern of mixed modes is accurate (see e.g. Beck et al., 2011; Montalbán et al., 2013; Mosser et al., 2012b; Jiang & Christensen-Dalsgaard, 2014; Cunha et al., 2015).

It is thus crucial not only to make predictions of RC $\Delta\Pi_g$ using the approximated expression in eq. 2.78, but also to compute the spectrum of individual modes, which may show interesting departures from the expected approximated relation/pattern, and that eventually can be compared with the detailed observed frequency spectrum. In Figures 4.3b−f I present the properties of adiabatic pulsation modes computed with GYRE (Townsend & Teitler, 2013), and compare frequency spectra of models with the same central helium abundance ($Y_c \simeq 0.7$), but computed with different convective-mixing schemes. In the upper panel of each figure it is possible to see how the inertia ($E$) of each mode varies in a frequency interval around the frequency of maximum oscillations power ($\nu_{max}$). Figures 4.3b−f also show that the characteristic asymptotic behaviour of the modes (the constant frequency separation for the low-inertia, pressure-dominated modes and the constant period spacing for the high-inertia, gravity-dominated modes) is a good representation of the detailed, numerically computed frequency spectrum. Moreover, the asymptotic value of the period spacing clearly reflects the differences in the Brunt-Väisälä frequency near the core (Fig. 4.3a and eq. 2.78), with the BS model having the lowest $\Delta\Pi_g$, and the HPC model the highest.

### 4.3.4 Signatures of sharp-structure variations in the period spacing

As evinced from Fig. 4.3a and, more clearly, from Fig. 4.4, $N$ may have sharp changes due e.g. to chemical composition gradients and/or in the temperature gradient in radiative regions. Whether such glitches have a significant impact of the

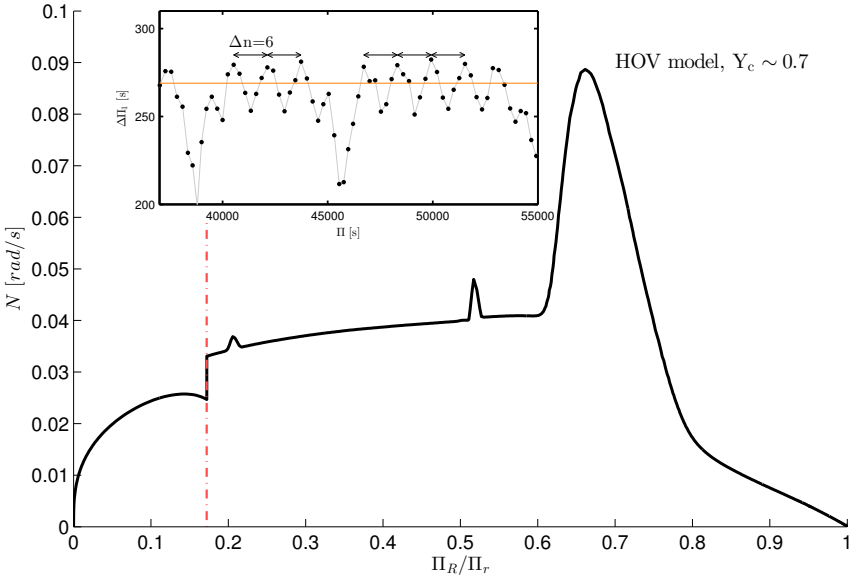


**Figure 4.4:** Brunt-Väisälä frequency as a function of the normalised buoyancy radius $\Pi_r/\Pi_R$ (see text) in a HOV model with $Y_c \simeq 0.7$. In the rectangle, $\ell = 1$ period spacing as a function of period for the same model. The period spacing of high-order g modes (e.g. in the period range $4.7 - 5.3\ 10^4$ s) is well described by the superposition of the asymptotic $\Delta\Pi_g$ (orange line) and a component with periodicity $\Delta n \simeq 6$. This periodicity indicates (see Eq. 4.1) a sharp-structure variation located at $\Pi_R/\Pi_r \simeq 1/\Delta n \simeq 0.17$, which corresponds well with the position of glitch in $N$.

period spacing depends on their location, their sharpness, and to the typical local wavelength of the gravity modes of interest.

As described in the literature (see e.g. Brassard et al., 1992; Miglio et al., 2008; Berthomieu & Provost, 1988), the signature of a sharp feature in the Brunt-Väisälä frequency is a periodic component in the periods of oscillations, and therefore in the period spacing, with a periodicity in terms of the radial order $n$ given by:

$$\Delta n \simeq \frac{\Pi_R}{\Pi_{\rm glitch}} \ , \tag{4.1}$$

where the total buoyancy radius is defined as:

$$\Pi_R^{-1} = \int_{r_0}^{R} \frac{N}{r'} dr' \ , \tag{4.2}$$

and local buoyancy radius is

$$\Pi_r^{-1} = \int_{r_0}^{r} \frac{N}{r'} dr' \ , \tag{4.3}$$

with $r_0$ and $R$ being the inner and outer boundary of the g-mode propagation region. The periodicity of the components in terms of radial order is therefore an indicator

of the location of the glitch, expressed in terms of its normalised buoyancy radius ($\Pi_R/\Pi_{\rm glitch}$).

In the models I am focusing on, I notice two main glitches. A prominent, yet smooth, glitch due to the H-burning shell and associated with $\nabla_\mu$ (see e.g. the glitch located at $\Pi_R/\Pi_r \simeq 0.7$ in Fig. 4.4). In models at the beginning of the HeCB phase, in which the H-burning shell is still very thin, this glitch is sharper and may give rise to significant departures from a smooth g-mode period spacing (see Bildsten et al. in preparation). In models during most of the HeCB phase, however, this glitch does not appear to give rise to significant deviations from the asymptotic $\Delta\Pi_{\rm g}$ expected for high-order g modes.

More interestingly, in the HOV model (see Fig. 4.3c and 4.4) I notice a sharp variation in $N$ which can be well described by a step function[3]. Given the location of this glitch $\Pi_R/\Pi_r \simeq 0.17$ (see Fig. 4.4) we expect a periodic deviation from the asymptotic $\Delta\Pi_{\rm g}$ with a periodicity of $\Delta n \simeq 6$, where $n$ is the radial order of gravity modes (see e.g. Miglio et al. 2008). This corresponds well (at least in the regions of pure g modes, e.g. in the range $4.7 - 5.3\ 10^4$ s) to the periodicity of the component (see inset of Fig. 4.4).

While the full description of these glitches is beyond the scope of the present work, I note that departures from the simple description of $\Delta\Pi_{\rm g}$ expected from the interaction between high-order g modes and an acoustic mode (Unno et al., 1989; Mosser et al., 2012b; Jiang & Christensen-Dalsgaard, 2014, e.g., see) provide additional, potentially very sensitive, probes of sharp-structure variations in near-core regions during the HeCB phase.

## 4.4 First comparison with observations: AGB bump and period spacing

### 4.4.1 The AGB bump in *Kepler* red giants

A catalogue of seismic ($\Delta\nu$ and $\nu_{\rm max}$) and spectroscopic ([M/H] and $T_{\rm eff}$) constraints for $\sim$ 1600 *Kepler* giants was recently published by the APOKASC collaboration (Pinsonneault et al., 2014).

I estimate stellar masses, and luminosities of these stars by using the so-called direct method, i.e. by combining $T_{\rm eff}$ with the seismic radii (estimated using $\Delta\nu$ and $\nu_{\rm max}$

[3] At the boundary of the fully mixed radiative (overshoot) region, the discontinuity in opacity, due to the difference between carbon rich mixed layers and He rich surrounding layers, leads to a discontinuity in $\nabla_T$ and thus in $N$.

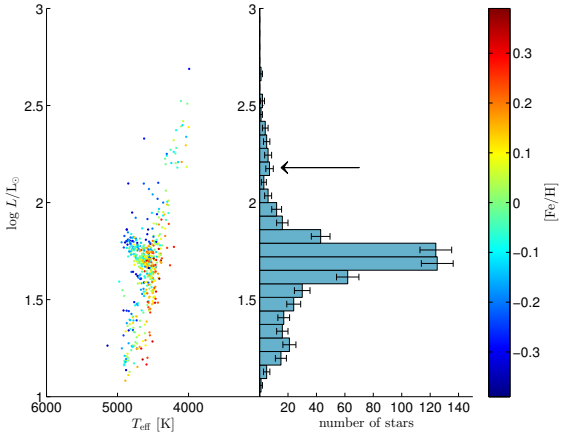


**Figure 4.5:** Hertzsprung-Russell diagram and luminosity distribution of the APOKASC catalogue (Pinsonneault et al., 2014). The sample is selected in a range of mass $M$ =1.3–1.7M$_\odot$ and metallicity [M/H] =-0.4–0.4. The AGB bump can be identified in the right the panel at around $\log L/\mathrm{L}_\odot \sim 2.2$ (black arrow) while the major peak correspond to the RC.

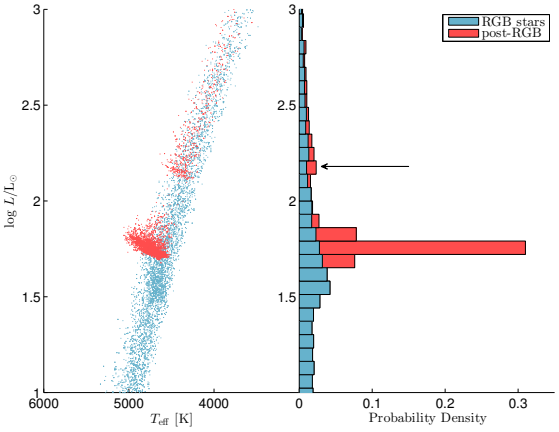


**Figure 4.6:** Hertzsprung-Russell diagram (left panel) and luminosity density distribution (stacked histogram, right panel) of stars in the TRILEGAL simulation of the *Kepler* field for the same masses and metallicities as in Figure 4.5. The AGB bump is visible in the right panel around $\log L/\mathrm{L}_\odot \sim 2.2$ (black arrow).

through scaling relations). This method is known to lead to less precise estimates of $M$ and $R$ than so-called "grid-based" approaches, yet it is less dependent on stellar evolutionary tracks (e.g. see Chaplin & Miglio, 2013, and references therein) and completely independent of bolometric corrections. I select stars from the APOKASC catalogue in a range of mass $M$ =1.3–1.7 M$_\odot$ and metallicity [M/H] =-0.4–0.4. The luminosity function of such stars displays a peak that is spread over about 4 bins and a has maximum at $\log L/\mathrm{L}_\odot \sim 2.2$: I interpret this peak as a strong candidate for the AGB bump (Figure 4.5). This statement is supported by the fact that 97.5% of the stars have errors smaller than the bin size. I also calculated 1000 realisations of the observed sample, assuming gaussian errors on $\Delta\nu$, $\nu_{\rm max}$, $T_{\rm eff}$ (taken from the APOKASC catalogue) and found that the properties of the peak in the luminosity function are not significantly affected.

As a word of caution I would like to stress that the APOKASC catalogue may, however, be affected by target selection biases (Pinsonneault et al., 2014). Although the maximum in the observed luminosity distribution does not appear to be significantly affected by widening the metallicity range, I notice that, if I extend the range of masses down to 1 M$_\odot$, the position of the peak is lowered by 1 bin (0.07 dex).

To check whether the AGBb is a feature we expect to be able to detect in a composite stellar population I use the TRILEGAL code (Girardi et al., 2012) to simulate the galactic population expected in *Kepler* field. The stellar models used are based on

Padova tracks (Bressan et al., 2012), with an overshooting parameter of $\Lambda_c = 0.5$ (i.e. $0.25H_p$, same mixing scheme adopted for PARSEC-LOV model). I apply to the synthetic sample the same selection in mass and metallicity as in the observed sample. The synthetic population also displays a well defined peak with a luminosity compatible with that of the candidate AGBb in the APOKASC catalogue (Figure 4.6).

From the simulations I estimate that about half of the red-giant stars in that peak belong to the RGB. This means that in the case of the full APOKASC catalogue (considering the entire range of mass and metallicity) I expect about $20-40$ AGBb stars.

In order to make a first comparison between my models and the observations, I generate histograms of the luminosity based on each of my tracks. Results of this comparison are shown in Figure 4.7. For the sake of clarity in the figure I have omitted RGB models. All the models are able to reproduce reasonably well the position of the RC, taking into account also the fact that my models are representative of a single-mass, single-metallicity population only, and that I have not added the effect of observational uncertainties when building the synthetic luminosity function.

The luminosity of the AGB-bump predicted by BaSTI-SC, and PARSEC-MPC are remarkably similar, and in good agreement with the candidate AGB-bump luminosity as detected in the observations. While PARSEC-LOV is another acceptable model, interestingly, the AGBb predicted by the BS, HOV, and HPC models is in clear disagreement with the observations, being either too faint (BS) or too bright (HOV, HPC).

### 4.4.2 Period spacing of *Kepler* RC stars

Mosser et al. (2014) recently published a catalogue that contains a large sample of red giants in the *Kepler* field for which g-mode asymptotic period spacings were inferred by modelling the interaction between pressure and gravity modes (see Unno et al., 1989; Mosser et al., 2012b). Thanks to this catalogue I am able to compare the observed period spacing with theoretical predictions. Iselect RC stars (i.e. stars with $\Delta\Pi_g > 175$ s) in a range of mass between 1.3 $M_\odot$ and 1.7 $M_\odot$, and compare the distribution of observed $\Delta\Pi_g$ with predictions from my models (see Fig. 4.8).

None of the models considered seems to describe satisfactorily the entire observed distribution. The BS model can be ruled out, since max $\Delta\Pi_g$ is $80-90$ s smaller than the maximum in the observed data. BASTI-SC, which was one of my best candidate models based on the comparison with the AGBb luminosity, shows a main peak in

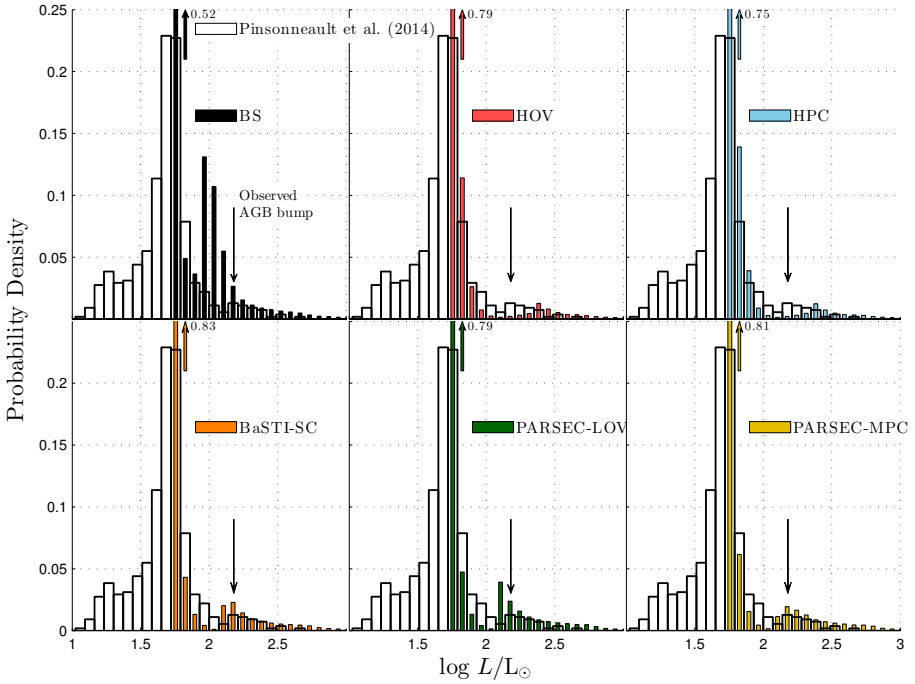


**Figure 4.7:** Comparison between the observed luminosity density distribution of stars in APOKASC public catalogue selected with the same criteria as in Figure 4.5, and the predictions from the models described in the main text. In the models, RGB stars are omitted.

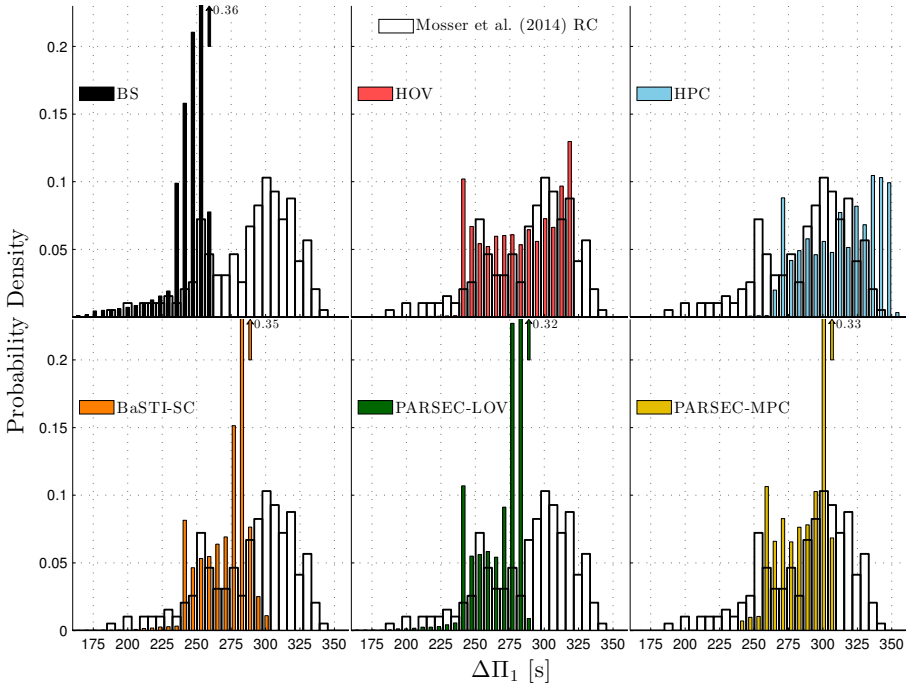


**Figure 4.8:** Comparison between the observed period-spacing distribution of stars classified by Mosser et al. (2014) as RC and AGB and the predictions from the models described in the main text. We have selected stars with mass $1.3 \leq M/M_\odot \leq 1.7$.

the $\Delta\Pi_g$ distribution about $20-30$s below the observed one and cannot describe period spacings higher than 300s . PARSEC-LOV has a very similar behaviour to BaSTI-SC and has a maximum $\Delta\Pi_g \simeq 285$ s. The HPC model is able to reproduce a large domain of the observed distribution, although its $\Delta\Pi_g$ appears shifted to higher values with respect to the observations. Finally, although PARSEC-MPC and HOV cannot reproduce the highest observed $\Delta\Pi_g$, their main peaks agrees with the observed one within 1-2 bins resolution.

In the observed distribution of $\Delta\Pi_g$(see Fig. 4.8) I notice, in addition to the main peak, a secondary peak at $\Delta\Pi_g \sim 253$ s, which still belongs to the RC population. Interestingly all my models, but BS, show the presence of this second structure. The reason behind it can be deduced simply following the theoretical tracks in the $Y_c - \Delta\Pi_g$ diagram (see Fig. 4.2). The tracks cross 3 times a narrow interval of period spacing: the first two times at the very beginning of the HeCB phase, i.e where $\Delta\Pi_g$ decreases until a local minimum and then starts to rise, while the third passage happens during the rapidly decrease that follows the absolute maximum (at the end of the HeCB). Since time and $Y_c$ are, in first approximation, linearly related during the HeCB, the third passage is very quick compared to the first and the second, therefore the peak is almost entirely populated by stars at the beginning of the phase. In the BS model the main and the second peak are not resolved since $\Delta\Pi_g$ stays nearly constant for most of the HeCB phase.

At this stage I am however limited to a qualitative comparison between observed and theoretical distributions of $\Delta\Pi_g$. Such limitation arises from the fact that observational biases at the target selection stage, and in the determination of the $\Delta\Pi_g$ from the power spectra, have not been fully explored yet. Moreover, although I have chosen models with a mass and metallicity representative of the stars observed by *Kepler* ($[M/H] = -0.07 \pm 0.24$), and selected stars according to the mass, my synthetic population is rather simplistic. As a first test of the effect of changing the mass and metallicity, I consider HOV models with different mass ($M = 1$ M$_\odot$) or metallicity ($Z = 0.007$). I find that while the $\Delta\Pi_g$ distribution depends little on the mass, the effect of reducing significantly the metallicity is to extend to the range of $\Delta\Pi_g$ by $\sim 20$ s. This effect needs to be taken into account when making quantitative comparisons between the observed and theoretically predicted distributions.

While these limitations can be partly mitigated by a more realistic synthetic population, and by a thorough examination of selection biases, it is likely that the most robust inference will be possible when applying my test to simple stellar populations, i.e. to red giants in the old-open clusters NGC6791 and NGC6819 (see chapter 5).

## 4.5 $R_2$ ratio: Comparison with the Literature

As introduced in section 4.1, the $R_2$ ratio is one of the most used observables for constraining the mass of the fully mixed core during the HeCB phase. Buonanno, Corsi & Fusi Pecci (1985), for the first time, estimated $R_2$ in three old and metal poor globular cluster (M15, M92, and NGC5466) founding an average of 0.14. In a more recent paper, Constantino et al. (2016) gave a new measurement of $R_2$ using 48 globular clusters analysed by Piotto et al. (2002) and Sarajedini et al. (2007), finding $R_2 = 0.117 \pm 0.005$. They then compared the model presented in their previous work (Constantino et al., 2015) with this new estimation (table 2 in their paper). However all the mixing schemes they proposed produce a $R_2$ smaller than observation. On the contrary, PaRSEC-MPC (and also BaSTI-SC) produces a $R_2 = 0.12$ compatible with the mean value found by Constantino et al. (2016) within the error. This positive result gives further support to the goodness of this mixing scheme.

## 4.6 Summary and future prospects

The ability to predict accurately the properties of He-core-burning stars depends on our understanding of convection, which remains one of the key-open questions in stellar modelling (e.g. see Castellani, Giannone & Renzini 1971a; Chiosi 2007; Salaris 2007; Bressan et al. 2015). Crucially, stringent tests of models have been limited so far by the lack of observational constraints specific to the internal structure of evolved stars.

In this work I propose a way forward. I argue that the combination of two observational constraints, i.e. the luminosity of the AGB bump and the RC period spacing of gravity modes, provides me with a decisive test to discriminate between competing models of HeCB low-mass stars.

I have computed a series of stellar models with various prescriptions for the transport of chemicals and for the thermal stratification of near-core regions, and using different evolution codes (MESA, BaSTI, and PARSEC). First, I used these models to make predictions about the duration of the RC and eAGB phases, the luminosity of the AGB bump, and C/O ratios in WDs. A summary of the models characteristics can be found in Table 4.1. I then focussed on the prediction of seismic observables (see Sec. 4.3.3). I found that the asymptotic period spacing of gravity modes depends strongly on the prescription adopted (with differences up to about 40%, when comparing the BS and HOV model).

I complemented this analysis by a numerical computation of adiabatic oscillation fre-

quencies. This allowed meto confirm that the asymptotic approximation (eq. 2.78) is a good representation of the period spacing of gravity-dominated modes. Moreover (see Sec. 4.3.4), the detailed behaviour of the period spacing of g modes shows the seismic signature of sharp variations in the Brunt-Väisälä frequency, which could potentially give additional information about near-core features (localised chemical composition gradients and near-discontinuities in the temperature gradient).
I then presented (Sec. 4.4) a first comparison between my predictions and the observational constraints obtained from the analysis of *Kepler* light curves (Pinsonneault et al., 2014; Mosser et al., 2014). I found evidence for the AGB-bump among *Kepler* targets, which allowed meto make a first combined analysis of classical (AGBb luminosity) and seismic (RC $\Delta\Pi_g$) constrains. my main conclusion is that, while standard models (BaSTI-SC, PARSEC-LOV) are able to reproduce the luminosity of the AGBb, they cannot describe satisfactorily the distribution of the observed period spacing of RC stars while models with high overshooting (HOV), although giving a much better description of the observed RC $\Delta\Pi_g$ distribution, fail to reproduce the AGBb luminosity. I then suggest a candidate model to describe simultaneously the two observed distributions: a model with a moderate overshooting region in which I apply an adiabatic thermal stratification. This prescription (which I have tested using PARSEC, see PARSEC-MPC model) gives indeed a better description of the observations.
At this stage of the analysis I am however prevented from drawing any further quantitative conclusions. To achieve the latter, I will follow two complementary approaches. On the one hand, I will couple my models with TRILEGAL, to generate synthetic stellar populations which can be quantitatively compared with the observed composite disk population. I will also investigate in detail possible observational biases, both in the target selection and in the detection of the period spacing from oscillations spectra. On the other hand, to limit/quantify such biases, I will test our models considering stars in the clusters NGC6791 and NGC6819, in which oscillations were detected in $\sim$ 30 HeCB giants (e.g., see Stello et al., 2011; Miglio et al., 2012; Corsaro et al., 2012).

# Chapter 5

# HeCB Period Spacing in Clusters and Field Stars

Recently, Vrard, Mosser & Samadi (2016) presented a revised catalogue of APOKASC red giants, for which they measured the gravity-mode period spacing. In addition, their data sample also contains red giants belonging to the clusters NGC 6791 and NGC 6819. This gives me the unique opportunity to study $\Delta\Pi_g$ in open clusters, reducing considerably the uncertainties given by the metallicity and mass.

## 5.1 Period Spacing of Cluster Stars: NGC6791 and NGC6819

### 5.1.1 Data and Target Selection

Differently from field stars, open clusters are formed by single stellar populations, i.e coeval and chemical homogeneous stars. Moreover, in the regime of LMS, the two RC are formed by stars with nearly the same mass. Coeval stars with slightly larger (or smaller) mass are, in fact, in later (or earlier) evolutionary stages. We can therefore test the plausibility of the "best-model" proposed in Chapter 4 (i.e. the moderate penetrative convection) in samples free of selection biases. Among all the clusters' stars by observed *Kepler*, I excluded non-clump stars and stars with mass larger than the average (Handberg et al., submitted, see appendix). The complete samples of the two clusters are shown in figure 5.1 (NGC 6791) and 5.2 (NGC 6819) in magnitude - effective temperature diagrams. In both figures the stars studied in Vrard, Mosser & Samadi (2016) are highlighted in red and marked with a cross if $\Delta\Pi_g$ is available. Targets selected for this study are circled in green.

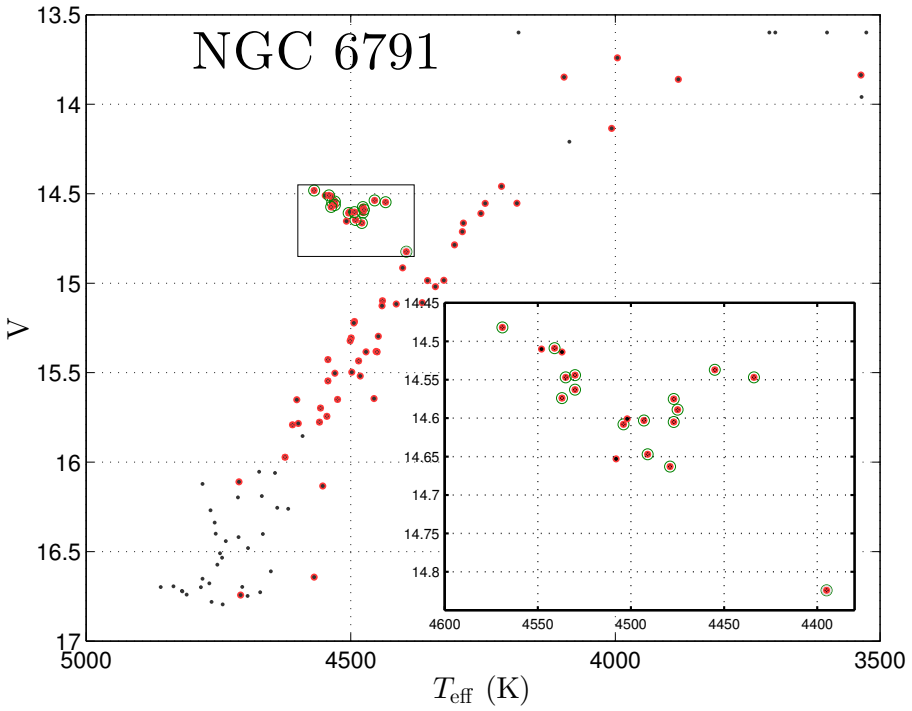


**Figure 5.1:** Target selection for NGC6791 on a magnitude-effective temperature diagram. The black dots are the stars observed by *Kepler*, the red circled dots are the RG studied in Vrard, Mosser & Samadi (2016). The red crosses indicate that $\Delta\Pi_{\rm g}$ is also provided. The red clump stars selected for my analysis are circled in green.

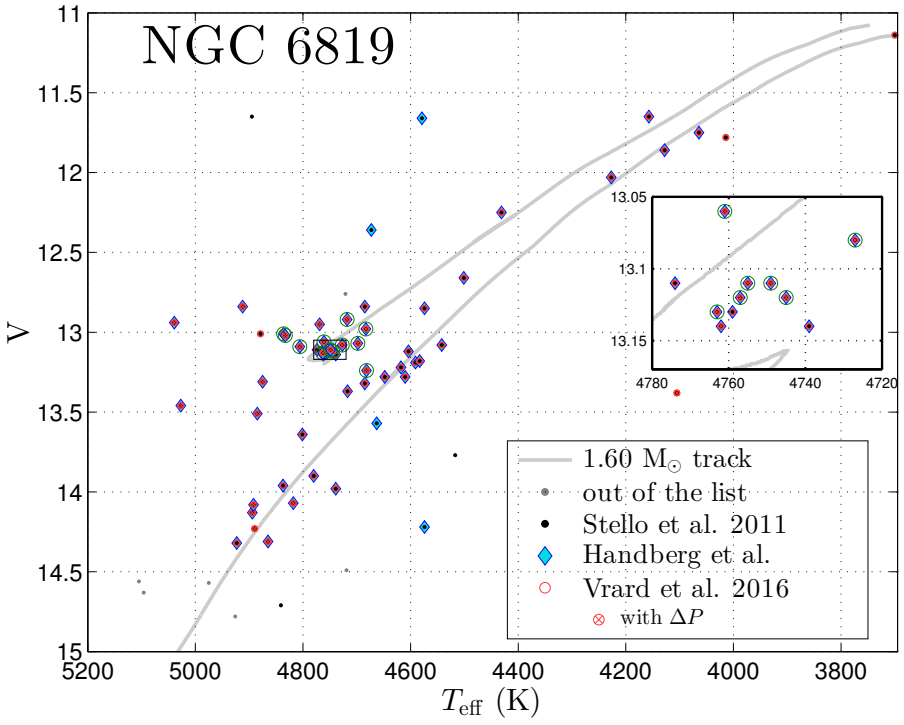


**Figure 5.2:** Target selection for NGC6819 on a magnitude-effective temperature diagram. The black dots are the stars observed by *Kepler* and reported in Stello et al. 2011, the red circled dots are the RG studied in Vrard, Mosser & Samadi (2016), crossed if also $\Delta\Pi_{\rm g}$ is provided. The red clump stars selected for my analysis are circled in green.

### 5.1.2 Stellar Models

I compute models representative of the giants in the two clusters, adopting different extra-mixing schemes: bare-Schwarzschild (BS), high overshooting (HOV), and high penetrative convection HPC (as defined in chapter 4). I also add the moderate penetrative convection (MPC) model, assuming an overshooting parameter of $\alpha_{\rm ovHe} = 0.5$ $H_p$. Despite the problems related with the He-semiconvection, the range of $\Delta\Pi_{\rm g}$ that this scheme spans during the HeCB is compatible with the observed values (see for instance figure 5.3). The physical inputs used for these tracks are IP1 (with Krishna Swamy 1966 atmosphere models). For NGC 6791 I calculate evolutionary track for which I assume $M = 1.15$ M$_\odot$, $Z = 0.0350$, and $Y = 0.300$ (Brogaard et al., 2011), while for NGC 6819 $M = 1.60$ M$_\odot$, $Z = 0.0176$, and $Y = 0.267$ (Handberg et al., submitted). For each of the tracks I create simple synthetic populations, imposing a scatter on $\Delta\Pi_{\rm g}$ in accordance with the real data. This can help us understand in which part of the RC evolution we expect to observe more stars. Figure 5.3 shows the comparison between the observed data and our models in the $\Delta\Pi_{\rm g}$-$\Delta\nu$ diagram. Large separations in the models is estimated using using individual radial frequencies (see section 3.4.1). The green lines corresponds to the moderate penetrative convection, i.e. the proposed "best-model" in chapter 4. In both cases this model appear to be compatible with the range of period spacing observed. Differences in $\Delta\nu$ between predictions and observations might be due to systematic shifts in the effective temperature related to the atmosphere model, which modifies the photospheric radius, and hence $\Delta\nu$ (eq. 2.85).

## 5.2 Period Spacing of Field stars: Mass and Metallicity Effects

In this section I explore the effects on the asymptotic period spacing in HeCB stars due to a different initial mass and metallicity. The dataset I use contains field stars and it was obtained by crossing the APOKASC catalogue (Pinsonneault et al., 2014) with the stars in Vrard, Mosser & Samadi (2016) for which $\Delta\Pi_{\rm g}$ were provided. The HeCB stars are selected looking for period spacings greater than 200s. The range of metallicity considered is [Fe/H] $\in [-0.50, 0.50]$. I limit the mass range to $M_{\rm seism} \in [1.0, 1.7]$ M$_\odot$ in order to avoid stellar masses that are approaching to the secondary clump condition. The behaviour of $\Delta\Pi_{\rm g}$ for higher masses will be discussed in chapter 6. Figure 5.4 shows the period spacing of the final selection plotted against the mass (upper panel) and metallicity (lower panel). It can be

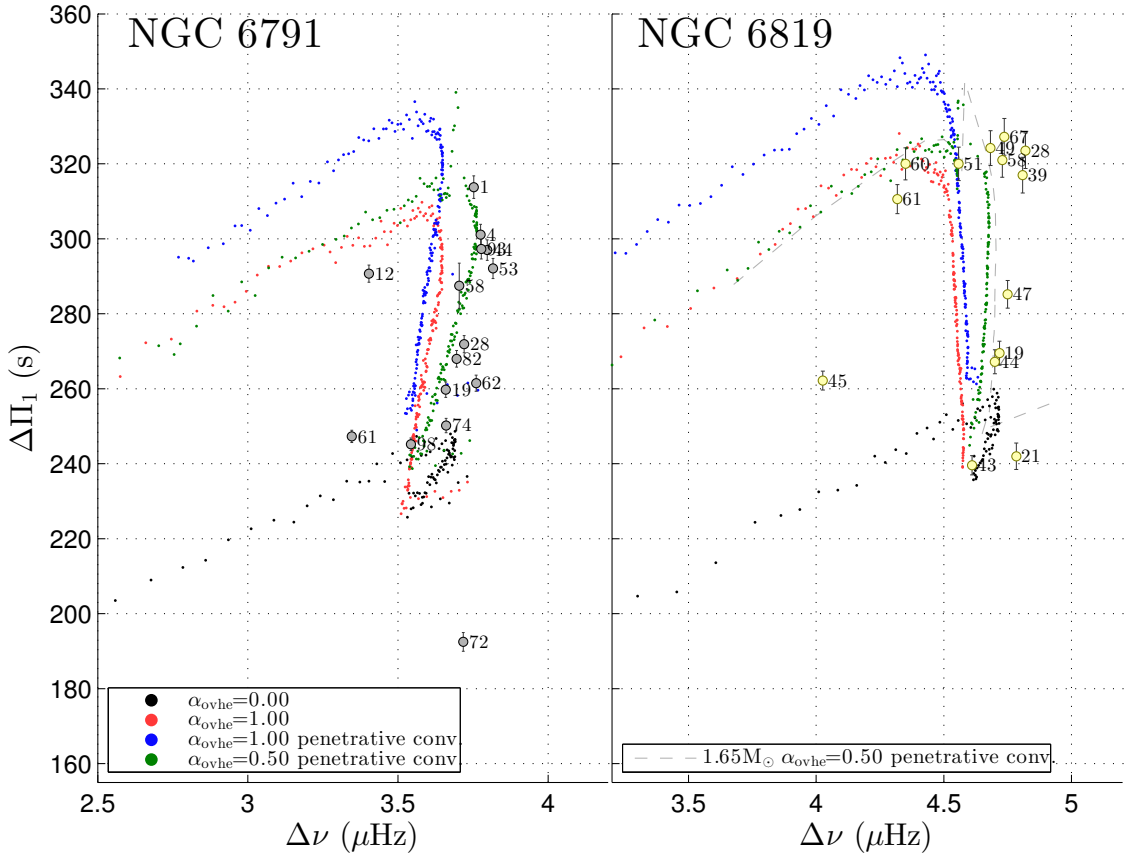


**Figure 5.3:** Red Clump stars of NGC6791 and NGC6819 clusters on a $\Delta\Pi_g$-$\Delta\nu$ diagram. Synthetic populations based on tracks computed with different mixing schemes are shown. The green points correspond to the mixing scheme MPC, proposed as "best-model".

noticed that, in the interval considered, the period spacing is limited in a "strip" between a maximum ($\Delta\Pi_{1,\max}$) and a minimum ($\Delta\Pi_{1,\min}$) value. These quantities remain constant with the mass, while they decrease as [Fe/H] increases. To quantify $\Delta\Pi_{1,\max}$ and $\Delta\Pi_{1,\min}$ I bin the dataset in mass and metallicity and for each bin I determine the 95th (representing $\Delta\Pi_{1,\max}$) and 5th percentiles ($\Delta\Pi_{1,\min}$).

In order to evaluate the uncertainties on the percentiles I use a technique called **bootstrapping**. First of all I create 1000 realisations of the observed population assuming in $\Delta\Pi_{\rm g}$ mass and [Fe/H]. I then bin the artificial samples in $M$ and [Fe/H] and measure the 95th and 5th percentiles. Finally I assemble all the 1000 iterations and calculate means and standard deviations of each 95th and 5th percentiles (see the black lines in figure 5.4). The data show an average decrease of $\Delta\Pi_{\rm g}$ with the metallicity, while it remains constant with the mass. As previously mentioned, the asymptotic period spacing is related to the inverse of the integral of the Brunt-Väisälä frequency ($N$) over the radius in the g-mode propagation cavity (Tassoul 1980 and eq. 2.78). The reason behind these variations in $\Delta\Pi_{\rm g}$ with the metallicity and mass have therefore to be searched in the differences in the $N$ profile (see figure 5.8), which, in turn, mainly depends on the physical properties of the core (e.g. pressure, density, opacity, and temperature).

To investigate the mass and metallicity effect on $N$ and $\Delta\Pi_{\rm g}$, I use the grid tracks introduced in section 3.3 that cover the entire range of mass and metallicity of the stellar catalogue, with steps respectively of 0.1 $M_\odot$ and 0.25 dex and considering a penetrative convection mixing scheme of 0.5 $H_p$. Looking at the Brunt-Väisälä frequency at the very beginning of the HeCB phase, we can notice that for a fixed metallicity all the profiles overlap, while visible differences are found by changing the metallicity (figure 5.8). The region that mostly influences $N$ is the convective core. Since $N$ is typically null in the deep fully convective regions, larger convective cores will lead to larger values of period spacings (Montalbán et al. 2013 and chapter 4). Models suggest that stars with similar masses have similar convective cores, while the latter are generally smaller at increased metallicity. The reason behind this has to be searched in the mass on the helium rich core ($M_{\rm He}$) at the He-burning ignition. $M_{\rm He}$ depends on the previous evolution and determines the initial condition of the central regions at the beginning of HeCB, such as the central temperature (larger $M_{\rm He}$, larger core temperature, see figure 5.5). Given the high dependence of the nuclear energy generation $\epsilon_{\rm nuc}$ on the temperature ($\sim T^{30-40}$ for the triple-$\alpha$ reaction), a small difference of the latter leads to large variation of $\epsilon_{3\alpha}$ with an impact on $L/M$ hence on the $\nabla_{\rm rad}$ ($\nabla_{\rm rad} \propto (L/M)\kappa\rho$), that modifies the location of the edge of the convective core. More precisely the size of the convective cores in

the HeCB phase decreases with increasing metallicity, while it remains almost equal when varying the mass. $M_{\rm He}$ is very similar to the value that the mass of the He core assumes at the RGB tip ($M_{\rm c,RGB-tip}$), i.e. the mass that a degenerate core must reach in order ignite the He burning in degenerate condition (helium flash, section 1.4.4). While the critical mass is almost independent from the initial mass, it varies with the chemical composition, i.e. [Fe/H] (but also initial helium mass fraction). As explained in detail in Cassisi & Salaris (2013), $M_{\rm c,RGB-tip}$ is mainly affected by the efficiency of the Hydrogen burning shell, which is higher in metal rich stars with respect to the metal poor ones. The dependence of the central temperature at the beginning of the HeCB on $M_{\rm He}$ is summarised in figure 5.7. A linear relation is found between $T_{\rm c}$ and $M_{\rm c,RGB-tip}$ for models with different metallicity, while $T_{\rm c}$ remains almost unchanged along the lines of constant [Fe/H]. However, this is true only for $M \lesssim 1.5 - 1.7$ M$_\odot$(depending on the metallicity). Above this value, $M_{\rm He}$ starts to decrease since we approach the secondary clump condition (stars that do not experience the Helium flash, Girardi 1999).
In Figure 5.4 I also show $\Delta\Pi_{1,\rm max}$ and $\Delta\Pi_{1,\rm min}$ for the models in the grid. In the lower panel I consider models with mass equal to 1.20 M$_\odot$ (the closest value to the average mass of the observed distribution, which is $\sim 1.25$ M$_\odot$), while for the upper panel I fixed the metallicity to [Fe/H] = 0.00 (mean observed value is [Fe/H] = $-0.034$). To better highlight the dependence of $\Delta\Pi_{1,\rm min}$ on the $M_{\rm c,RGB-tip}$, I show its variation in figure 5.6. It can be noticed that, excluding $M > 1.6$ M$_\odot$, the values of $\Delta\Pi_{1,\rm min}$ as a function of $M_{\rm c,RGB-tip}$ collapse along a line that monotonically decreases with the metallicity. Moreover, the metallicity effect is more evident in $\Delta\Pi_{1,\rm max}$ with respect to $\Delta\Pi_{1,\rm min}$. The behaviour of $\Delta\Pi_{1,\rm max}$ is also present in clusters, where it is easy to see that the period spacing of NGC6891 clump stars reaches higher values than the more metal rich NGC6791, and they are both well represented by the MPC models.

## 5.3 Sources of Uncertainties

I show here the results of a series of additional tests that we perform on models to ascertain whether the constrains on the mixing are robust.

### 5.3.1 Initial Helium Mass Fraction

An additional test is made to quantify the effect of the initial helium on the period spacing. $Y$ is in fact coupled in my grid with $Z$, by the relation eq. 3.6. I therefore compute three tracks of mass 1.50 M$_\odot$: the first and the second share the same

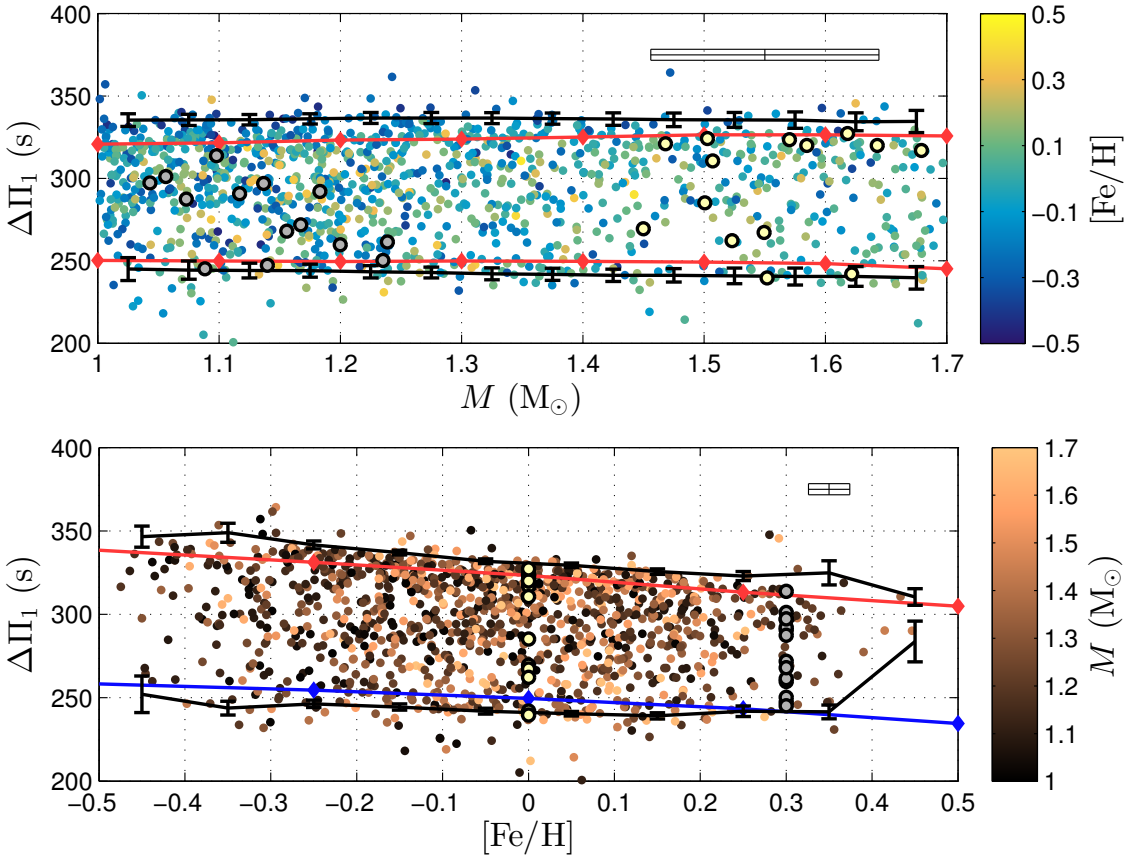


**Figure 5.4:** Period spacing of stars in APOKASC catalogue crossed with Vrard, Mosser & Samadi (2016) plotted against the mass (upper panel) and the metallicity (lower panel). Black lines correspond to the 95th and 5th percentiles of the data distribution along the period spacing. The data show an average decrease of $\Delta\Pi_g$ with the metallicity, while it remains constant with the mass. Models (red lines) also suggest this behaviour. An indication of the typical error on the data is visible in the top-right corner of each panel. NGC6791 (grey dots) and NGC6819 (yellow dots) cluster stars are also shown. Their range of period spacing is compatible with the APOKASC sample.

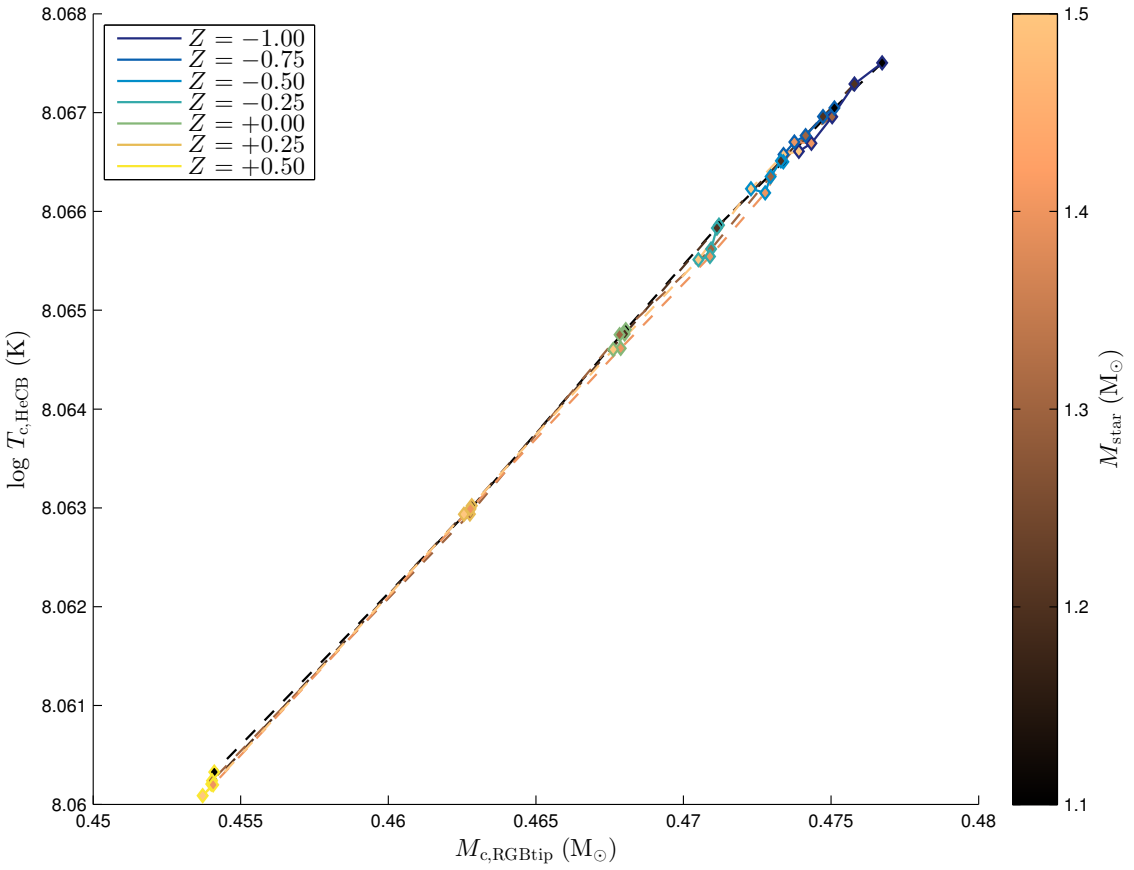


**Figure 5.5:** Relation between central temperature at the beginning of the HeCB phase and the mass of the helium core at the RGB tip. The graph shows that for increasing metallicity $T_{\mathrm{c,HeCB}}$ and $M_{\mathrm{c,RGBtip}}$, decrease linearly, while they both remain almost constant varying the stellar mass.

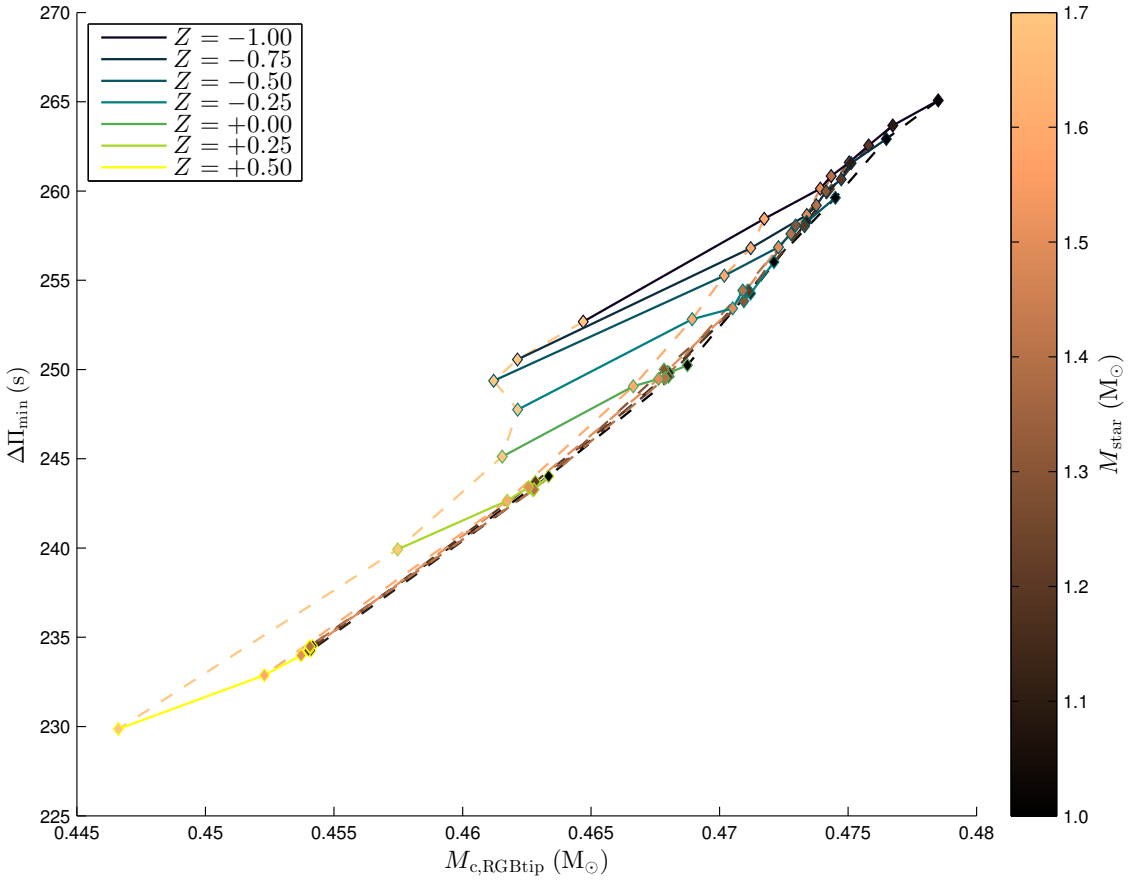


**Figure 5.6:** Predicted of $\Delta\Pi_{1,\rm min}$ in relation with the mass of the at the end of the RGB phase (RGB tip).$\Delta\Pi_{1,\rm min}$ and $M_{\rm c,RGBtip}$ are related similarly to $T_{\rm c,HeCB}$ and $M_{\rm c,RGBtip}$ in figure 5.5. The line of constant 1.7 $M_\odot$ deviates from the other lines of constant mass since it is close to the transition mass (see Chapter 6).

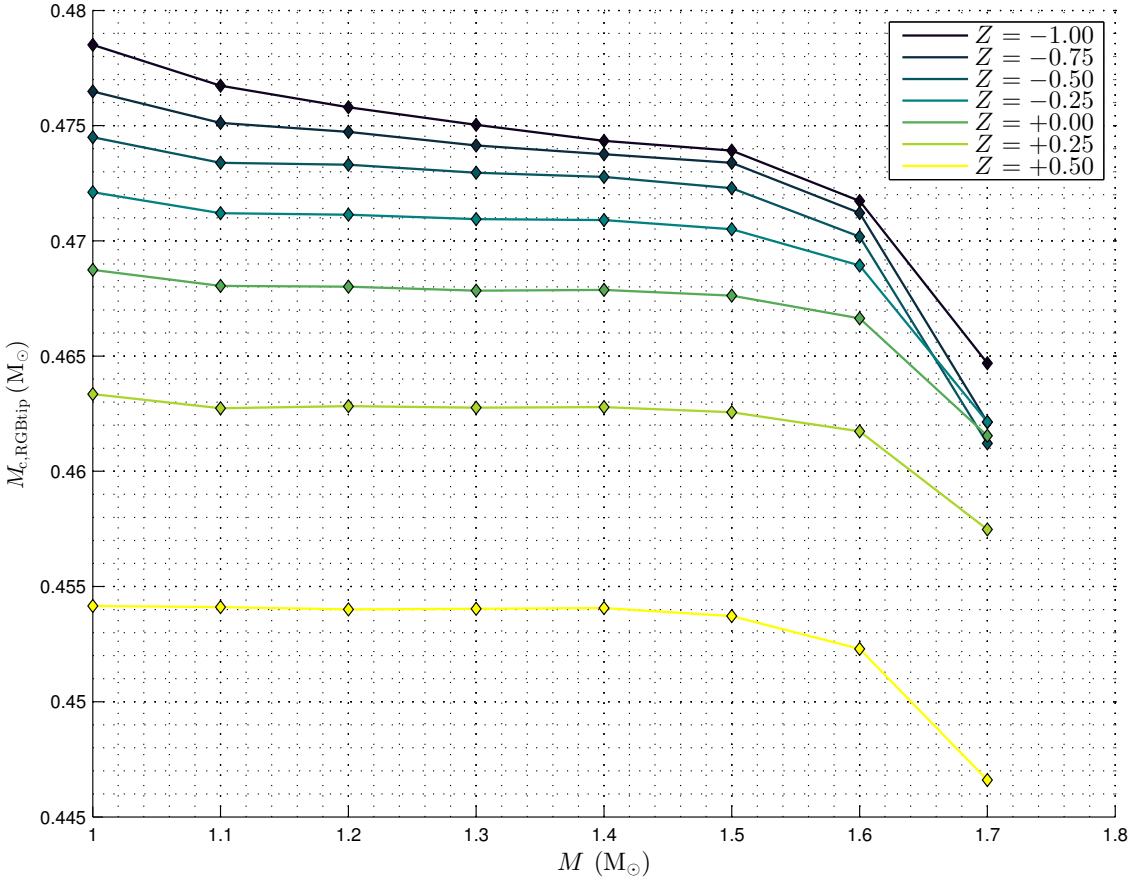


**Figure 5.7:** Relation between mass of the helium core at the RGB tip and the total mass

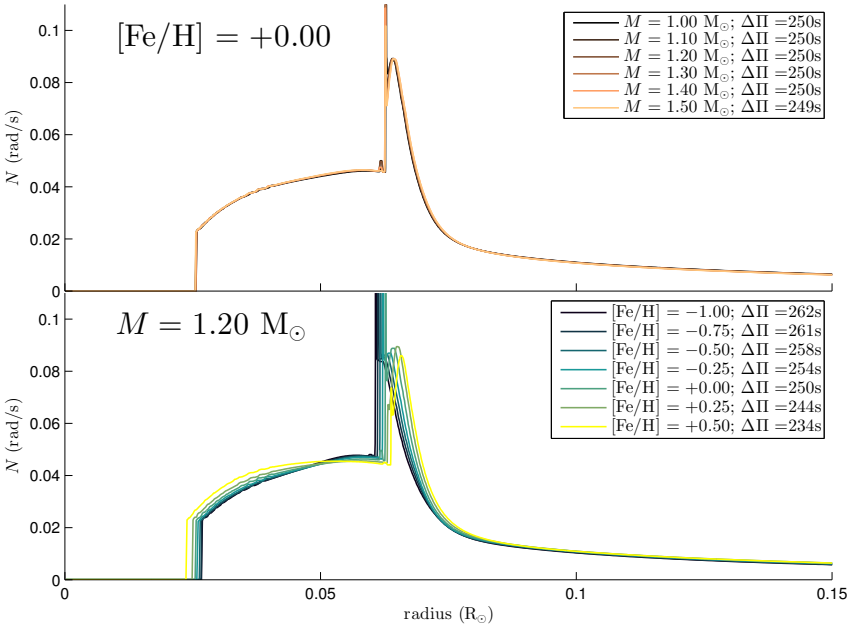


**Figure 5.8:** Brunt-Väisälä frequency in the model grid at the start of the helium burning. $N$ profiles are shown on the upper panel for models with fixed metallicity ([Fe/H] = 0.00), while in the lower panel for fixed a mass ($M = 1.20$ $M_\odot$).

metallicity $Z = 0.031$ ([Fe/H] = 0.25) but differ in initial helium ($Y = 0.25$ to $Y = 0.28$), while the third has a lower metallicity ($Z = 0.002$) but the same $Y$ (0.25) as the first track. The choice of $Z$ and $Y$ was done considering the limits of the grid. In particular the first and third tracks are located at the opposite corners of the grid, while the second track represent a sort of midpoint between the two. The right panel in figure 5.9 shows the evolution of $\Delta\Pi_{\rm g}$ with central helium for the three tracks. It can be easily noticed that the differences in $\Delta\Pi_{\rm g}$ are dominated by the metallicity (in a range of $15 - 40$ seconds). The effect of helium results to be relevant only at the very beginning of the HeCB phase with an increment of $\Delta\Pi_{\rm g}$ that can reach $\sim 10$ s. However, this difference becomes negligible immediately after the local minimum of the period spacing, with a variations of at maximum $1 - 2$ s in the rest of the phase (that could be ascribed to numerical noise).

### 5.3.2 $^{12}$C($\alpha$,$\gamma$)$^{16}$O nuclear reaction rate.

One of the major sources of uncertainty in stellar modelling are nuclear reaction rates (see e.g. Straniero et al., 2003; Cassisi, Salaris & Irwin, 2003). One of the least well-known reaction rates is indeed the $^{12}$C($\alpha$,$\gamma$)$^{16}$O reaction, that, along with triple-$\alpha$, plays a fundamental role during the HeCB. Its effects are relevant to several properties of the subsequent evolution. For instance, different values of this reaction rate can modify the duration of the HeCB phase and the central C/O abundance at the end of the core burning. However, the impact of $^{12}$C($\alpha$,$\gamma$)$^{16}$O on the period spacing is still poorly studied. A first attempt was recently done by Constantino et al. (2015). In their work, the authors tested the effect of $^{12}$C($\alpha$,$\gamma$)$^{16}$O on a 1 $M_\odot$ stellar model with 0.001 $H_p$ diffusive overshooting (exponential decay function, Herwig 2005, Campbell & Lattanzio 2008), finding a deviation of about 5 sec on the average $\Delta\Pi_{\rm g}$ if a standard uncertainty (about 40% of the reaction rate) is considered. However, the deviation can also depend on the mixing scheme adopted. I compute a series of HeCB evolutionary tracks ($M = 1.5$ $M_\odot$, solar abundance) in which I adopt four $^{12}$C($\alpha$,$\gamma$)$^{16}$O reaction rates in conjunction with 3 mixing schemes: Bare-Schwarzschild model (BS), 1.0 $H_p$ step function overshooting (HOV), and 1 $H_p$ penetrative convection (HPC). The $^{12}$C($\alpha$,$\gamma$)$^{16}$O reaction rates considered are the tabulated values given by JINA (Cyburt et al., 2007), K02 (Kunz et al., 2002), CF88 (Caughlan & Fowler, 1988), and NACRE (Angulo et al., 1999) and already made available in MESA. While no differences can be noticed at the beginning of the phase, the models suggest that the effect of the different reaction rates becomes relevant as the evolution proceeds, reaching a maximum at the end of the HeCB

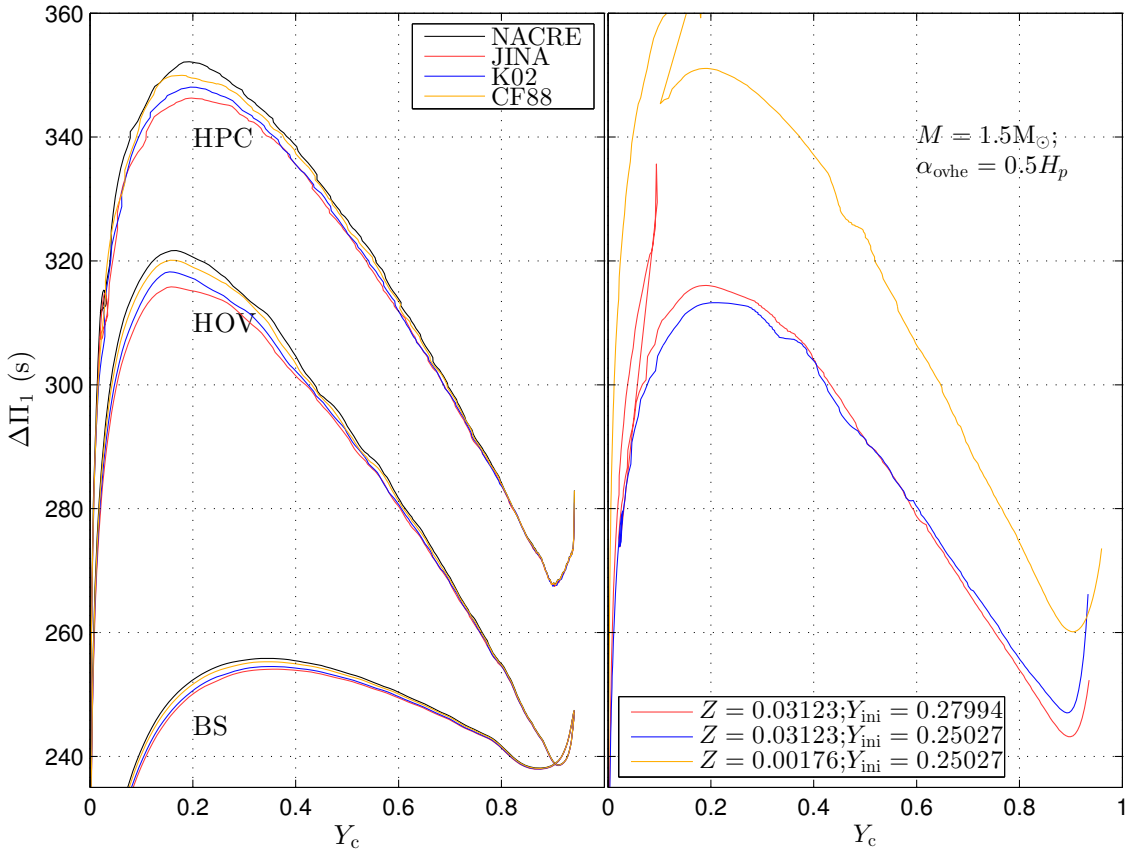


**Figure 5.9:** *left panel:* RC-$\Delta\Pi_g$ evolution as a function of central helium mass of a $M = 1.50$ $M_\odot$solar metallicity star with three different mixing schemes and four different $^{12}C(\alpha,\gamma)^{16}O$ reaction rates. *Right panel:* RC-$\Delta\Pi_g$ evolution as a function of central helium mass fraction of a $M = 1.50$ $M_\odot$star computed assuming three different combination of $Z$ and $Y$.

(Figure 5.9). This is expected, since the relative contribution of the $^{12}C(\alpha,\gamma)^{16}O$ with respect to triple-$\alpha$ becomes more and more important with the increasing $^{12}C$ abundance. The impact of the different mixing schemes is evident at the maximum period spacing where HOV tracks show a scatter of around 6-7 s between them, compared to only $\sim 2$ s for BS. I therefore expect an uncertainty contained between 6 and 2 s on the MPC model. This value is of the same order magnitude of the average $\Delta\Pi_g$ error for clump stars ($\sim 3.5$ s).

## 5.4 Final Remarks

With an exception of few stars, figure 5.3 shows a good agreement between the period spacing of NGC6819 and NGC 6791 red clump giants and the model predictions, computed adopting the mixing scheme I proposed at the end of chapter 4. The mixing scheme consists in a moderate ($\alpha_{\mathrm{ovHe}} = 0.50$) penetrative convection. I was also able to test the mixing scheme on a large number of field stars with different

masses and chemical composition, studying the effects that the metallicity and the stellar mass might introduce in the HeCB $\Delta\Pi_g$ (section 5.2). While $\Delta\Pi_g$ shows no appreciable dependence on the mass, I have found a clear dependence of $\Delta\Pi_g$ on metallicity (figure 5.4) also suggested by the models, which strengthens even further the result on the clusters (since clusters' stars are chemically homogeneous). Moreover, the limited effects found performing tests on the initial helium abundance and concerning the nuclear reactions (section 5.3.1 and 5.3.2) suggest that these two possible source of uncertainties do not have a large impact on the model prediction. However, the comparison between the data percentiles and the predicted values for $\Delta\Pi_{1,max}$ and $\Delta\Pi_{1,min}$ in figure 5.4, suggests that the models fail at fully covering the observed range of period spacing. While the maximum can be extended simply increasing the overshooting parameter, the minimum can be reduced only by changing the thermal stratification in the overshooting region from adiabatic, to radiative. The issue might also be present in figure 5.3, in which the MPC models is not able to reach the low $\Delta\Pi_g$ values of stars number 21 and 43 in NGC6819. This seems to indicate that he mixing scheme I adopted should be somehow revised, for instance by considering in the overshoot region a thermal stratification in between the radiative and the adiabatic one (see e.g. Christensen-Dalsgaard et al. 2011).

# Chapter 6

# Effect of Main-Sequence Mixing Processes on Secondary-Clump Stars

## 6.1 Introduction

In the previous chapter I focused the analysis on stars with masses lower than of $1.6 - 1.7$ $M_{\odot}$. From this value upward, stars approach the transition between LMSs and IMSs. In the interval between $1.2 - 2.5$ $M_{\odot}$, the ZAHB (zero age horizontal branch) presents a minimum in luminosity (figure 6.1). In composite stellar populations, this local minimum forms a separate feature in the HR diagram, named **secondary clump** (SC, Girardi, 1999, and references therein). The mass of stars at the luminosity minimum (transition mass, $M_{\rm tr}$) essentially separates the low-mass stars from the intermediate- and high-mass stars.

Stars belonging to the secondary clump have been also identified investigating asteroseismic quantities (see e.g. Bedding et al., 2011; Mosser et al., 2011). For instance, by analysing the observed period spacing dispersion and the large separation of HeCB stars, Mosser et al. (2011) identified at high-$\Delta\nu$ and low-$\Delta\Pi_{\rm g}$ a tail in the distribution that they ascribed to the secondary clump.

Montalbán et al. (2013) used the observed $\Delta\Pi_{\rm g}$ provided by Mosser et al. (2012b) as diagnostic for studying the central properties of secondary clump stars. They showed that at the same mass $M_{\rm tr}$, the predicted average HeCB period spacing presents a minimum as well, pointing out that in stellar models increasing MS-overshooting modifies $M_{\rm tr}$, shifting the expected minimum to lower mass values. Finally, they compared their models with the period spacing of RGs field stars with Mosser et al. (2012b) catalogue. However, their data-model comparison suffered from a few limitations, primarily related to the observed dataset used. Mosser

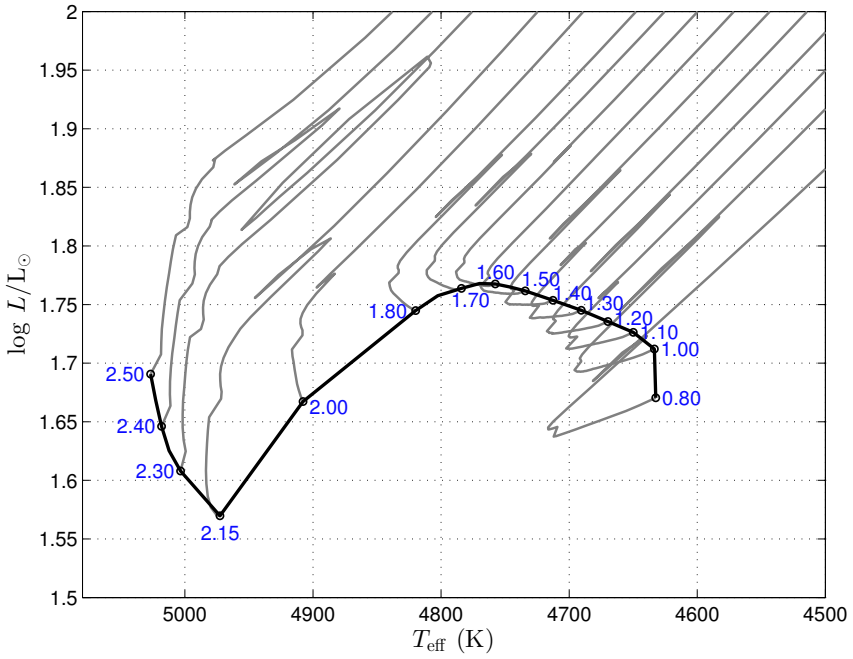


**Figure 6.1:** HRD of the Zero Age Horizontal Branch based on evolutionary tracks (in grey, from the ZAHB to the early AGB) in a mass interval between $M = 0.8$ M$_\odot$ and $M = 2.5$ M$_\odot$ and initial metallicity [Fe/H]=0.0. The tracks are computed with MESA with IP1 physical inputs.

et al. (2012b) catalogue, in fact, has a limited number of stars and, crucially, no information on the stellar metallicity. Therefore they could not take into account any biases introduced by the metallicity. Moreover, the $\Delta\Pi_{\rm g}$ provided corresponds to the observed value, defined using the period differences of observed frequencies, that is generally lower than the corresponding asymptotic period spacing (used e.g., in the my previous chapters).

In this chapter I will present my attempt to continue their work comparing the new APOKASC catalogue of red giants (Pinsonneault et al. 2014 with $\Delta\Pi_{\rm g}$ determined by with Vrard, Mosser & Samadi 2016 and the metallicity) with a series of models computed by MESA with different MS overshooting parameters, which substantially extends the models considered in Montalbán et al. (2013). Varying the overshooting parameter in MS, I will investigate how $M_{\rm tr}$ and the HeCB-$\Delta\Pi_{\rm g}$ depend on the amount of overshooting considered. Finally, I will compare my predictions with data to set constraints on the amount of extra near-core mixing on MS, which is one of the key uncertainties in stellar modelling (Chiosi, 2007).

## 6.2 Models and Data

Before looking in detail at the physical reasons behind the dependence with the mass of both luminosity and $\Delta\Pi_g$ in HeCB stars, I will introduce the models and the data used in this work.

### 6.2.1 Models

The evolutionary tracks are computed with MESA considering only the solar metallicity. The range of mass varies between 1.40 $M_\odot$ and 4.00 $M_\odot$, with a step 0.05 $M_\odot$ in the interval $1.50 - 2.5$ $M_\odot$. Differently from the works in the previous chapters, I adopted here a diffusive overshooting (Herwig 2000 and section 3.2.5) with a parameter $\alpha_{\rm ovH,diff} = 0.00$, 0.01, 0.02,0.04. The choice of changing the mixing scheme is due to the fact that MESA is not able to treat correctly receding convective cores (like in MS) if the step function overshooting is applied. In fact, it produces many discontinuities and an irregular chemical profile due to numerical problems. Nevertheless this does not affect the HeCB and it is important only during the early RGB of LMS and before the HeCB of IMS, i.e. in the phases between the end of the hydrogen-core burning and the moment when the H-shell encounters the chemical discontinuity left by the first dredge-up.
Similar problems have been also noticed at the bottom of the convective envelope along the RGB, and therefore I decided to apply here as well a very small amount of diffusive undershooting. The value of the parameter chosen (0.005) is small enough to not affect considerably the evolution of the models. For LMS, it produces a small extension in luminosity of the RGB bump. On the other hand, the mixing scheme adopted during the HeCB is kept unvaried, i.e. a step function penetrative convection of 0.5 $H_P$.
In addition to my grid of models, I have also computed a series of tracks without HeCB extra mixing (bare Schwarzschild, BS see section 3.2.1) with $\alpha_{\rm ovH,diff} = 0.00$ and $\alpha_{\rm ovH,diff} = 0.02$ in MS.

### 6.2.2 Data

The data presented here are an extension of the catalogue used in the the previous chapter. I have considered field stars in the APOKASC catalogue (Pinsonneault et al., 2014) which have period spacings determined by Vrard, Mosser & Samadi (2016) and I have expanded the mass range to values greater than 1.40 $M_\odot$. In order to compare the data with solar metallicity models, I limit the range of [Fe/H]

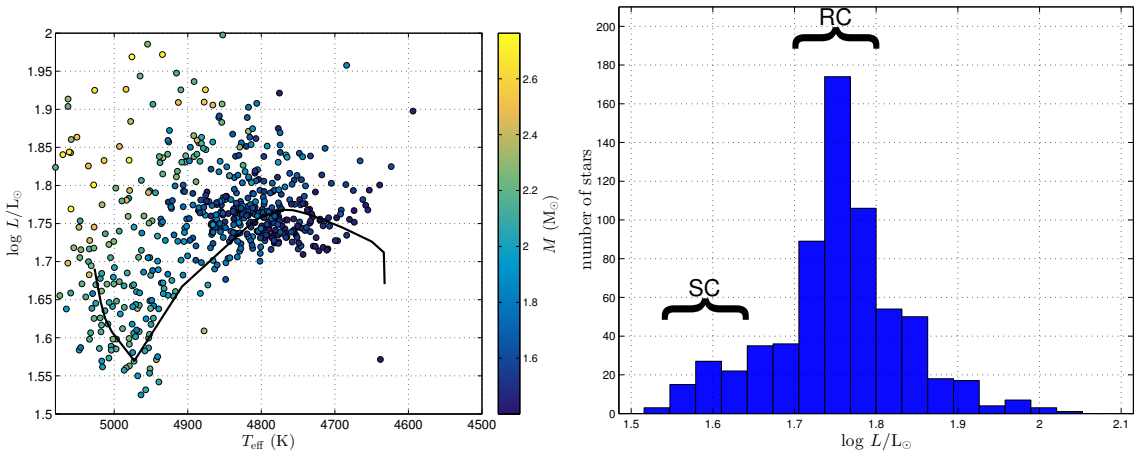


**Figure 6.2:** *left panel:* HRD of the HeCB stars in the APOKASC catalogue crossed with Vrard, Mosser & Samadi (2016). The stars are selected in a metallicity range of $-0.2 < [\mathrm{Fe/H}] < 0.2$. In black the model ZAHB. *right panel:* the luminosity distribution of the stars in the left panel. The graphs brackets mark indicatively the position of the secondary clump and the red clump.

in the interval $[-0.2, 0.2]$. The selection of the HeCB stars has been done considering only stars with period spacings greater than 100 s. The HRD of the catalogue is presented in figure 6.2 (left panel), where we can see the presence of stars with luminosity below the red clump with masses on average greater than in the RC. For further clarity, the corresponding luminosity distribution was also plotted (figure 6.2, right panel) in which are shown the indicative locations the SC and RC stars. The stellar masses are calculated using the scaling relation eq. 2.87, while the errors are estimated using the formula

$$\sigma_M = \sqrt{\left(\frac{\partial M}{\partial \nu_{\rm max}}\right)^2 \sigma^2_{\nu_{\rm max}} + \left(\frac{\partial M}{\partial \Delta\nu}\right)^2 \sigma^2_{\Delta\nu} + \left(\frac{\partial M}{\partial T_{\rm eff}}\right)^2 \sigma^2_{T_{\rm eff}}}. \tag{6.1}$$

The distribution of the relative error $\sigma_M/M$ is shown in figure 6.3 where we observe that the vast majority of the stars have uncertainties in mass between 6% and 10%. The estimation of the $\sigma_M$, however, does not consider systematic errors in mass due to the limitation of the scaling relation (see section 3.4.1, figure 3.12c) that, for a metallicity $[\mathrm{Fe/H}] = 0.00$, are of the order about $0.5-1\%$ in the mass range between 1.00 $M_\odot$ and 2.50 $M_\odot$. Figure 6.3 also shows the relative error in $\Delta\Pi_{\rm g}$.

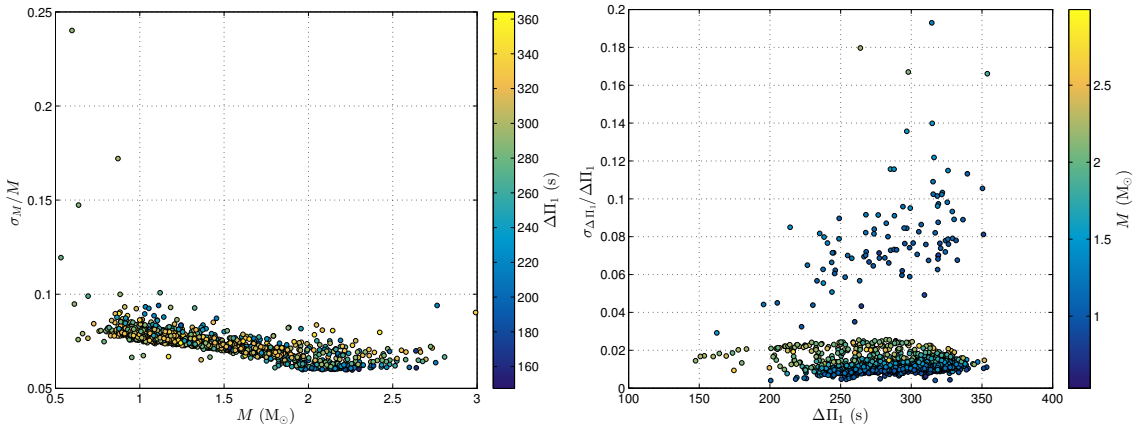


**Figure 6.3:** Relative errors in mass (left panel) and period spacing (right panel) of the stars in figure 6.2.

## 6.3 Dependence of $M_{c,RGB-tip}$ and HeCB-$\Delta\Pi_g$ on the MS overshooting

In Chapter 1, we saw that LMSs climb the RGB growing a highly degenerate helium core until the latter reaches the critical value of $M_{HeF}$ and starts the process that will remove the electron degeneracy (helium flash). On the contrary, IMSs ignite the helium-core-burning in quiescent conditions, i.e. before encountering the total electron degeneracy. In figure 6.4 I show how the size of the helium core at the RGB-tip ($M_{c,RGB-tip}$) varies with the mass, assuming different amount of MS overshooting. Let's first focus only the models without extra mixing (black line). We can identify three regimes: (1) $M_{c,RGB-tip}$ is independent of the mass for $M \lesssim 1.70$ M$_\odot$, (2) it decreases with mass until a minimum at $\sim 2.30$ M$_\odot$, after which (3) the $M_{c,RGB-tip}$ grows monotonically with the stellar mass. The first regime corresponds to LMS stars that develop no or small convective core in MS. The core of these stars becomes degenerate before the temperature necessary to activate helium nuclear reactions ($T_{He,ignite}$) is reached. Simultaneously with the growth of the He-core, the central degeneracy also increases, along with the neutrino cooling of the centre that shifts the temperature maximum off-centre. In LMS the position of the maximum temperature and the size of the He core is independent from the stellar mass. However, when increasing the initial mass, the He-core mass at the end of the MS becomes large enough and sufficiently far from degenerate conditions so that $T_{He,ignite}$ requires a smaller He core (second regime).

From the mass corresponding to the minimum upward (third regime), stars ignite helium-core burning in quiescent conditions and the size of their cores starts to increase with the initial mass. It is now easy to understand that by increasing the

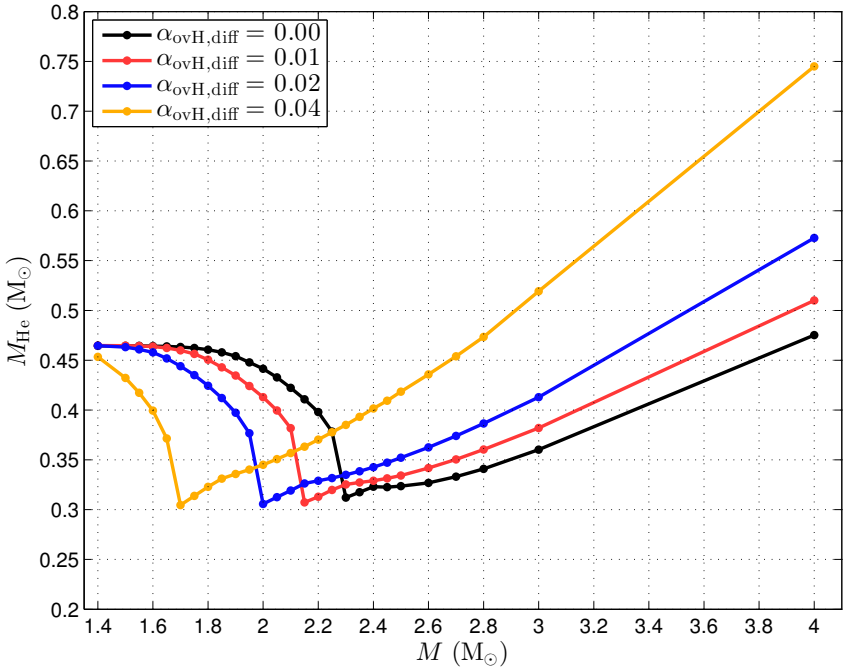


**Figure 6.4:** Mass of the helium core at he RGBtip as function of the initial mass for 4 different MS diffusive overshooting parameter.

MS overshooting parameter, we are going to increase as well the He core at the beginning of the RGB, anticipating in mass the second and third regimes.
Resuming the discussion presented in section 5.2, in which I explained the dependence of $\Delta\Pi_{\rm g}$ on the metallicity, we saw there that the period spacing of the gravity modes during the HeCB phases has a dependency on the central temperature of the star which, in turn, is related to the $M_{\rm c,RGB-tip}$. Again, a larger $M_{\rm c,RGB-tip}$ will increase the central temperature in the HeCB phase and as a consequence it will also increase the range of the period spacing in HeCB. We define a average value of $\Delta\Pi_{\rm g}$ that stars have during the helium-core burning, this value will have the same behaviour with mass than $M_{\rm c,RGB-tip}$, presenting a decrease with mass until a minimum at $M_{\rm tr}$ followed by a monotonic increase (see figure 6.4 and 6.6). By modifying $M_{\rm tr}$, the MS-overshooting has therefore a large impact also on the range of period spacing.

## 6.4 Comparison with Data and Discussion

The main comparison between the data and the models has been done on the diagram $\Delta\Pi_{\rm g} - M$ (figure 6.6).

- In order to highlight the behaviour of $\Delta\Pi_{\rm g}$ in the data, I need to estimate

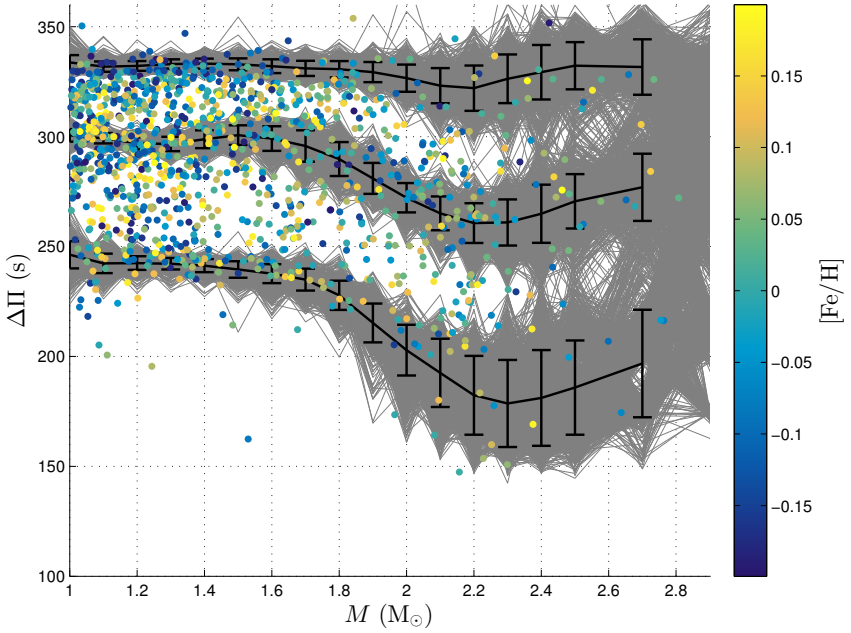


**Figure 6.5:** Visualization of how the bootstrapping was applied. The figure shows the period spacing against initial mass of the selected stars in the APOKASC catalogue (see the main test). The grey lines are the 95th, 50th, 5th percentiles of the single synthetic populations based on the original catalogue. The black lines are the mean value of each group of percentiles.

the mean maximum and minimum values that the period spacing assumes in function of the mass. To do so, similarly to the previous chapter on section 5.2, I estimate the 95th, 50th, and 5th percentiles of the $\Delta\Pi_{\rm g}$ distribution within bins in mass taking advantage of a bootstrapping technique (figure 6.5). In figure 6.5 and 6.6 we notice that in all the three curves, corresponding to the bottom (5th percentile,$\Delta\Pi_{1,\rm min}$), the top (95th percentile$\Delta\Pi_{1,\rm max}$), and the median $\Delta\Pi_{\rm g}$(50th percentile, $\Delta\Pi_{1,\rm aver.}$) in HeCB, a monotonically decreasing trend is followed by an increase in $\Delta\Pi_{\rm g}$. However, the position of the minimum, that appears to be located around 2.2 $M_\odot$ (according to $\Delta\Pi_{1,\rm aver.}$and $\Delta\Pi_{1,\rm max}$), is not clearly identified. This is mainly caused by the scarceness of stars with masses $M \gtrsim 2.2$ $M_\odot$. This increases the errorbars on the percentiles, and the uncertainties on the mass estimation (6-10%) spread artificial stars along the $M$ axis in a region where we expect large variations in the $\Delta\Pi_{\rm g}$ axis.

- Regarding the models, in order compare them with the data, I estimate the minimum, maximum, and average $\Delta\Pi_{\rm g}$ in the HeCB phase. I therefore generate a synthetic population along each track (limiting it to the HeCB phase) in which I calculate the 95th, 50th, and 5th percentiles of the $\Delta\Pi_{\rm g}$ distribution. As we discussed in the previous chapters, models reach the maximum value of $\Delta\Pi_{\rm g}$ near the end of the HeCB ($Y_{\rm c} \sim 0.1 - 0.2$), while the $\Delta\Pi_{1,\rm min}$ is referred

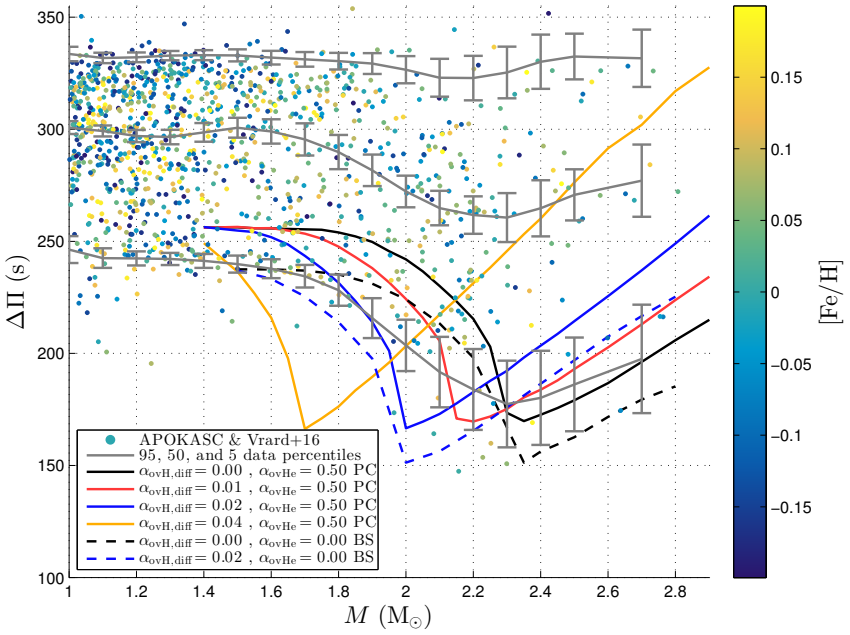


**Figure 6.6:** Period spacing against the initial mass for the selected stars in the APOKASC catalogue with their 95th, 50th, and 5th mean percentiles.The coloured lines are the $\Delta\Pi_{1,\min}$ curve predicted by the models for several MS diffusive overshooting.

to stars at the beginning of the phase. Since the latter are the only structures that are not affected by the known issues related to He-semiconvection, I decide to use in this analysis only the model-predicted $\Delta\Pi_{1,\min}$. In figure 6.6 I plot the $\Delta\Pi_{1,\min} - M$ curve for each track. The observed average $\Delta\Pi_{\rm g}$ suggests that the mixing scheme that better represents, among those explored here, the data has confined between $0.00 < \alpha_{\rm ovH,diff} < 0.02$ with a preference for the value 0.01. However, since the ambiguity in the location of the minimum in the data, due to the size of the errorbars on the 50th percentile, additional statistical tests are needed for a quantitative inference on $\alpha_{\rm ovH,diff}$, which will be carried out in future work.

- Another important difference between the models and the data is given by the offset of the $\Delta\Pi_{1,\min}$ curves at masses $M < 2{\rm M}_\odot$. The offset is due to the adiabatic $\nabla_T$ in the overshooting region that tends to create a larger period spacing with respect to a radiative gradient (as explained in chapter 4). The difference disappears when the adiabatic excess in the extra-mixing region is reduced or removed. The BS models (represent by dashed lines in figure 6.6) seem to reproduce well the behaviour of $\Delta\Pi_{1,\min}$ for $M \lesssim 1.6 - 1.7{\rm M}_\odot$ but starts to deviate approching to the transition mass. We can also notice that the minimum in each curve is independent from the mixing scheme adopted in the HeCB. This is because the interval in which the $\Delta\Pi_{\rm g}$ varies depends

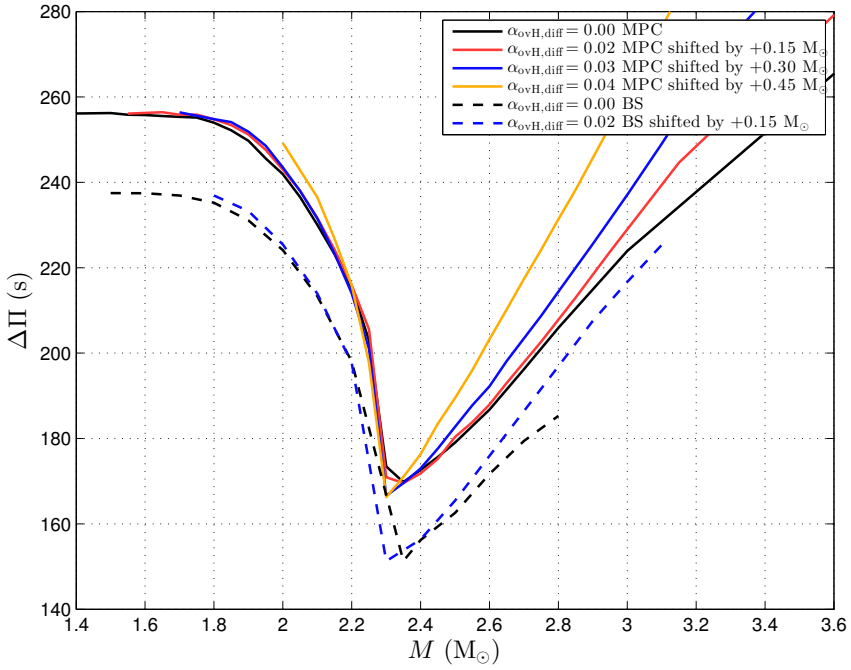


**Figure 6.7:** Period spacing against the initial mass for the $\Delta\Pi_{1,\min}$ curve predicted by the models and linear shifted in mass by +0.15 $M_\odot$ every increment of $\Delta\alpha_{ovH,diff} = 0.01$.

on the mass of the He-core at the start of the HeCB phase, that is the result of the past evolution. At the very beginning of the HeCB, BS models have similar $\Delta\Pi_g$ with respect to low and high overshooting models (see figure 4.2). The comparison between PC and BS models suggests that at the start of the helium-core burning the pure penetrative convection is not the preferred model. However, the only pure radiative overshooting scheme we saw able to produce the period spacing compatible with the observation is the high overshooting (HOV) which, on the other hand, we know is not able to describe classical proprieties, like the AGBb luminosity. A possible solution may be a mixing scheme in which the temperature stratification has a smooth transition from the fully adiabatic one in the convective core, to the radiative one at the outer border of the overshooting region (see e.g. Christensen-Dalsgaard et al., 2011).

- Finally, figure 6.6 and figure 6.4 also show that the mass corresponding to the minimum $\Delta\Pi_g$ (i.e. $M_{tr}$) appears to be in linear relation with the MS overshooting parameter $\alpha_{ovH,diff}$. More precisely, for an increase of $\Delta\alpha_{ovH,diff} = 0.01$, $M_{tr}$ decreases of about 0.15 $M_\odot$. Moreover, the four curves are perfectly overlapped during the second regime (figure 6.7). This suggests that the behaviour of $\Delta\Pi_{1,\min}$ in this region can be predicted by a simple parametrization of the $\Delta\Pi_{1,\min}$ curve without extra mixing in MS (black lines in figure 6.6), with the

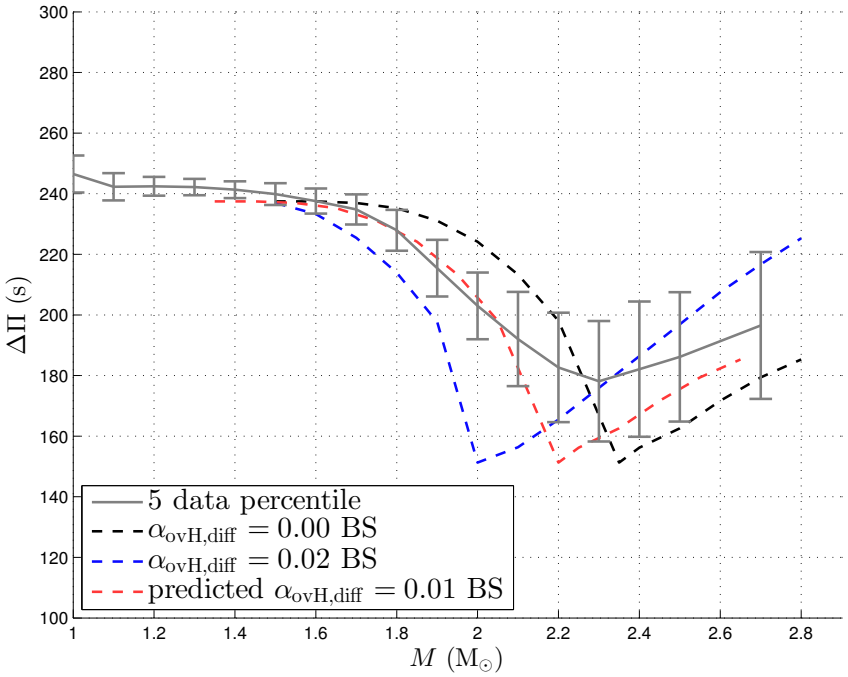


**Figure 6.8:** Comparison on the $\Delta\Pi_g$-$M$ diagram between the 5th percentile and the BS models for $\alpha_{\rm ovH,diff} = 0.00, 0.01, 0.02$ . The curve corresponding to $\alpha_{\rm ovH,diff} = 0.01$ was predicted by shifting in mass $\alpha_{\rm ovH,diff} = 0.00$ by $-0.15$ $M_\odot$.

only free parameter $\alpha_{\rm ovH,diff}$ that shifts linearly the the curve in mass. Since the second regime is well populated in the APOKASC catalogue, the determination of the optimum value for $\alpha_{\rm ovH,diff}$ can be done by comparing the 5th percentile in the mass range 1.4 $M_\odot < M <$ 2 $M_\odot$with the parametrized curve, varying the $\alpha_{\rm ovH,diff}$ values. As a preliminary test I create the $\Delta\Pi_{1,\rm min}$ curve for $\alpha_{\rm ovH,diff} = 0.01$ and BS scheme in HeCB by shifting the no extra-mixing curve of $-0.15$ $M_\odot$. By comparing the curve with 5th percentile (figure 6.8, red line) I found an excellent agreement.

# Conclusions

The main topic of this thesis was the investigation of the propierties of red-giant stars throughout the different stages of their evolution, with particular emphasis on stars that burn helium in their cores. The ability to predict accurately the properties of He-core-burning stars depends on our understanding of convection, which remains one of the key-open questions in stellar modelling (e.g. see Castellani, Giannone & Renzini 1971a; Chiosi 2007; Salaris 2007; Bressan et al. 2015). Crucially, stringent tests of models have been limited so far by the lack of observational constraints specific to the internal structure of evolved stars. In recent years, however, the seismology of red giants has become a very fruitful field in stellar astrophysics, mainly thanks to space-based telescopes like *Kepler* and CoRoT. Red giants have very rich frequency spectra that can provide several stringent constraints to their, otherwise inaccessible, internal structures.
Using a combination of theoretical models, classical and asteroseismic data, I have shown that it is now possible to make a step forward in the study of the physical processes that occur in their interiors, as well as in the determination of their global parameters (like mass, age, radius, and metallicity).

## Near-core mixing, AGB bump, and Period spacing

In Chapter 4 I investigated how stellar models of helium-core-burning stars are affected by various prescriptions for the transport of chemicals and for the thermal stratification of near-core regions. Here I resume my conclusion, also written written in (Bossini et al., 2015). I have computed a series of models using different evolution codes (MESA, BaSTI, and PARSEC). First, I used these models to make predictions about the duration of the red clump and early AGB phases, the luminosity of the AGB bump, and C/O ratios in White Dwarfs (a summary of the models characteristics can be found in Table 4.1). I then focussed on the prediction of seismic observables (see Sec. 4.3.3), and found that the asymptotic period spacing of gravity modes depends strongly on the prescription adopted (with differences up to about

40%, when comparing the BS and HOV model).
I complemented this analysis by a numerical computation of adiabatic oscillation frequencies. This allowed us to confirm that the asymptotic approximation (eq. 2.78) is a good representation of the period spacing of gravity-dominated modes. Moreover (see Sec. 4.3.4), the detailed behaviour of the period spacing of g modes shows the seismic signature of sharp variations in the Brunt-Väisälä frequency, which could potentially give additional information about near-core features (localised chemical composition gradients and near-discontinuities in the temperature gradient).
I then presented (Sec. 4.4) a first comparison between our predictions and the observational constraints obtained from the analysis of *Kepler* light curves (Pinsonneault et al., 2014; Mosser et al., 2014). I found evidence for the AGB-bump among *Kepler* targets, which allowed us to make a first combined analysis of classical (AGBb luminosity) and seismic (RC $\Delta\Pi_g$) constrains. The main conclusion is that, while standard models (BaSTI-SC, PARSEC-LOV) are able to reproduce the luminosity of the AGBb, they cannot describe satisfactorily the distribution of the observed period spacing of RC stars. On the other hand models with high overshooting (HOV), although giving a much better description of the observed RC $\Delta\Pi_g$ distribution, fail to reproduce the AGBb luminosity. I then suggested a candidate model to describe simultaneously the two observed distributions: a model with a moderate overshooting region in which I apply an adiabatic thermal stratification. This prescription (which I have tested using PARSEC, see PARSEC-MPC model) gives indeed a better description of the observations.
With only this evidence in hand, however, I could not draw any further quantitative conclusions. Stars in the catalogues used belong in fact to the composite disk population an therefore of different mass and metallicity. This may introduce possible observational biases, both in the target selection and in the detection of the period spacing from oscillations spectra. To limit/quantify such biases, it is necessary to test models considering stars in the clusters, which, differently from field stars, are formed by single stellar populations, i.e they are coeval and chemical homogeneous stars.

## Clusters and Field Stars

Recently, Vrard, Mosser & Samadi (2016) presented a revised catalogue of APOKASC red giants, for which they measured the gravity-mode period spacing. In addition, their data sample also contains red giants belonging to the clusters NGC 6791 and NGC 6819. This gave me the unique opportunity to study $\Delta\Pi_g$ in open clusters,

testing the prescription introduced in Chapter 4, reducing considerably the uncertainties given by the metallicity and mass. With the exception of few stars, I found a good agreement between the period spacing of NGC6819 and NGC 6791 red clump giants and the model predictions, computed adopting the mixing scheme I proposed at the end of chapter 4. The mixing scheme consists in a moderate ($\alpha_{\rm ovHe} = 0.50$) penetrative convection (MPC).

To test the robustness of this conclusion, I then analysed the source of uncertainties that can affect the model predictions. First of all I tested my MPC mixing scheme on a large number of field stars with different masses and chemical composition, in order to quantify the effect that the metallicity and the stellar mass might introduce in the HeCB $\Delta\Pi_{\rm g}$ (section 5.2). I have found a clear dependence of $\Delta\Pi_{\rm g}$ on the metallicity (figure 5.4) also suggested by the models, which strengthens further the result on the clusters (since cluster stars are chemically homogeneous). However, the comparison between the data percentiles and the predicted values for $\Delta\Pi_{1,\rm max}$ and $\Delta\Pi_{1,\rm min}$, suggests that the models fail at fully covering the observed range of period spacing. While the maximum can be extended by simply increasing the overshooting parameter, the minimum can be reduced only by changing the thermal stratification in the overshooting region from adiabatic, to radiative. The issue could also explain why a few stars in NGC6819 are not fitted by the MPC track. This might suggest that the mixing scheme I adopted should be somehow revised, for instance by considering in the overshoot region a thermal stratification between the radiative and the adiabatic one (see e.g. Christensen-Dalsgaard et al. 2011).

Finally, I found that the effects of changing the initial helium abundance and using different nuclear reaction rates available in the literature (section 5.3.1 and 5.3.2) are limited, suggesting that these two possible source of uncertainties do not have a large impact on the model prediction of $\Delta\Pi_{\rm g}$.

# Secondary Clump

The discussion presented in Chapter 5 was limited to low-mass stars with mass lower then $\sim 1.5$ M$_\odot$. From this value upward, stars approach the secondary clump, in which the transition between LMSs and IMSs takes place.

In Chapter 6 I analysed the period spacing of the APOKASC catalogue of red giants (Pinsonneault et al., 2014) for HeCB stars with mass larger then 1.40 M$_\odot$ up to 2.80 M$_\odot$. The data show indeed a decreasing trend of $\Delta\Pi_{\rm g}$ with the mass for stars between $M = 1.40$ M$_\odot$ up to $M = 2.20$ M$_\odot$, as also predicted by the models (Girardi, 1999; Montalbán et al., 2013).

Varying the overshooting parameter in MS in models computed by MESA, I investigated the dependence of $M_{\rm tr}$ and of the HeCB-$\Delta\Pi_{\rm g}$ on the amount of overshooting considered, finding results comparable to those presented in Montalbán et al. 2013. However, their comparison with data was limited to a small number of stars, no information on [Fe/H]was available, and only the observed value of $\Delta\Pi_{\rm g}$, On the contrary, the catalogue I used was significantly larger, and with information about metallicity and asymptotic period spacing. This allowed me to perform a more stringent comparison with model predictions, reducing the biases introduced by the metallicity by selecting stars in a interval $-0.2 <$ [Fe/H] $< 0.2$]. The main results of the analysis can be summarized as follows:

- Despite both the 5th($\Delta\Pi_{1,\rm min}$), 95th($\Delta\Pi_{1,\rm max}$), and the 50th percentile of the $\Delta\Pi_{\rm g}$ distribution in HeCB showing a monotonically decreasing trend with mass, the position of the expected minimum, which appears to be located around 2.2 $M_\odot$, is not clearly identified. The observed median $\Delta\Pi_{\rm g}$ suggests that the mixing scheme that better represents the data, among those explored in the chapter, has a parameter in the range between $0.00 < \alpha_{\rm ovH,diff} < 0.02$ with a preference for the value 0.01. However the ambiguity in the location of the minimum in the data does not allow me to quantify with accuracy the best value for $\alpha_{\rm ovH,diff}$.

- The observed median $\Delta\Pi_{\rm g}$ suggests that the mixing scheme that better represents, among those explored here, the data is confined between $0.00 < \alpha_{\rm ovH,diff} < 0.02$ with a preference for the value 0.01. However, since the ambiguity in the location of the minimum in the data, additional statistical tests are needed for a quantitative inference on $\alpha_{\rm ovH,diff}$, which will be carried out in future work.

- Another important difference between the models and the data is given by the offset of the $\Delta\Pi_{1,\rm min}$ curves at masses $M < 2M_\odot$. The offset is due to the adiabatic $\nabla_T$ in the HeCB overshooting region that tends to create a larger period spacing with respect to a radiative gradient (as explained in chapter 4). The difference disappears when the adiabatic excess in the extra-mixing region is reduced or removed. The bare-Schwarzschild models (BS) seems to reproduce well the behaviour of $\Delta\Pi_{1,\rm min}$ for $M \lesssim 1.6 - 1.7M_\odot$ and starts to deviate from the observation when the decreasing region begins. At the very beginning of the HeCB, BS models have similar $\Delta\Pi_{\rm g}$ with respect to low and high overshooting models (see figure 4.2). The comparison between PC and BS models suggests that at the start of the helium-core burning the pure penetrative convection is not the preferred model. However, the only

pure radiative overshooting scheme we saw able to produce the period spacing compatible with the observation is the high overshooting (HOV) which, on the other hand, we know is not able to describe classical proprieties, like the AGBb luminosity. A possible solution may be a mixing scheme in which the temperature stratification has a smooth transition from the fully adiabatic one in the convective core, to the radiative one at the outer border of the overshooting region (see e.g. Christensen-Dalsgaard et al., 2011).

- Finally, I found that the mass corresponding to the $\Delta\Pi_{1,\min}$ (i.e. $M_{\rm tr}$) appears to be in linear relation with the MS overshooting parameter $\alpha_{\rm ovH,diff}$. More precisely, for an increase of $\Delta\alpha_{\rm ovH,diff} = 0.01$, $M_{\rm tr}$ decreases of about 0.15 $M_\odot$. Moreover, the four curves are perfectly overlapped during the decreasing regime of $\Delta\Pi_{1,\min}$. This suggests that the behaviour of $\Delta\Pi_{1,\min}$ in this region can be predicted by a simple parametrization of the $\Delta\Pi_{1,\min}$ curve without extra mixing in MS (black lines in figure 6.6), with the only free parameter $\alpha_{\rm ovH,diff}$ that shifts linearly the the curve in mass. Since the second regime is well populated in the APOKASC catalogue, the determination of the optimum value for $\alpha_{\rm ovH,diff}$ can be done by comparing the 5th percentile in the mass range 1.4 $M_\odot < M <$ 2 $M_\odot$with the parametrized curve, varying the $\alpha_{\rm ovH,diff}$ values. As a preliminary test I create the $\Delta\Pi_{1,\min}$ curve for $\alpha_{\rm ovH,diff} = 0.01$ and BS scheme in HeCB by shifting the no extra-mixing curve of $-0.15$ $M_\odot$. By comparing the curve with 5th percentile I found an excellent agreement.

# Future prospects

The issue related with the He-semiconvection is, indeed, one of the major problems encountered during my work. Correct models for the final stages of the Helium-core-burning are necessary to fully explore the physics of the observed stars and to give more accurate predictions of the global parameters of the current and subsequent evolutionary phases. It become necessary, therefore, to introduce a treatment for He-semiconvection in MESA code, in order also to revise the results obtained, if needed. However, classical He-semiconvection treatments already implemented in various codes, like e.g. BaSTI and PARSEC, have not a solid physical background and in reality require many times arbitrary numerical "tricks". This, on the hand, gives the opportunity to explore alternative ways to treat this delicate phase. A first attempt was already proposed in section 3.2.6 and provisionally called "Modified Overshooting". This model however still needs to be tested thorougly.

In addition, an alternative to the standard mixing schemes was recently proposed by (Christensen-Dalsgaard et al., 2011) to describe the overshooting region underneath the solar convective envelope, and it may represent the correct solution to describe the period spacing distribution of the observed stars showed in Chapters 5 and 6. Once a well-tested mixing scheme is ready to be used, I will be able to perform more accurate data-model comparison in order to calibrate stellar models. These models will be also used to develop PARAM, a unique tool introduced in Chapter 3 that, joining classic and asteroseismic information, can determine precise stellar proprieties. PARAM can be then used to characterize thousands of stars for the most different cases: from the purpose of studying a single stellar population to helping galactic archaeology in improving our knowledge of the Milky Way.

# Appendix A

# Publication Record

## Articles published in peer-review journals

1 Miglio, A.; Chaplin, W. J.; Brogaard, K.; Lund, M. N.; Mosser, B.; Davies, G. R.; Handberg, R.; Milone, A. P.; Marino, A. F.; **Bossini, D.**; Elsworth, Y. P.; Grundahl, F.; Arentoft, T.; Bedin, L. R.; Campante, T. L.; Jessen-Hansen, J.; Jones, C. D.; Kuszlewicz, J. S.; Malavolta, L.; Nascimbeni, V.; Sandquist, E. L.
Detection of solar-like oscillations in relics of the Milky Way: asteroseismology of K giants in M4 using data from the NASA K2 mission
Accepted for publication in MNRAS, 2016, eprint arXiv:1606.02115

2 Lagarde, N.; **Bossini, D.**; Miglio, A.; Vrard, M.; Mosser, B.,
Testing the cores of first ascent red giant stars using the period spacing of g modes,
Monthly Notices of the Royal Astronomical Society, 2016, Volume 457, Issue 1, p.L59-L63

3 Campante, T. L.; Lund, M. N.; Kuszlewicz, J. S.; Davies, G. R.; Chaplin, W. J.; Albrecht, S.; Winn, J. N.; Bedding, T. R.; Benomar, O.; **Bossini, D.**; Handberg, R.; Santos, A. R. G.; Van Eylen, V.; Basu, S.; Christensen-Dalsgaard, J.; Elsworth, Y. P.; Hekker, S.; Hirano, T.; Huber, D.; Karoff, C.; Kjeldsen, H.; Lundkvist, M. S.; North, T. S. H.; Silva Aguirre, V.; Stello, D.; White, T. R.,
Spin-orbit alignment of exoplanet systems: ensemble analysis using asteroseismology,
Accepted for publication in ApJ, 2016, eprint arXiv:1601.06052

4 **Bossini, Diego**; Miglio, Andrea; Salaris, Maurizio; Pietrinferni, Adriano; Montalbán, Josefina; Bressan, Alessandro; Noels, Arlette; Cassisi, Santi; Girardi, Léo; Marigo, Paola,
Uncertainties on near-core mixing in red-clump stars: effects on the period spacing and on the luminosity of the AGB bump,
Monthly Notices of the Royal Astronomical Society, 2015, Volume 453, Issue 3, p.2290-2301

5 Rodrigues, Thaíse S.; Girardi, Léo; Miglio, Andrea; **Bossini, Diego**; Bovy, Jo; Epstein, Courtney; Pinsonneault, Marc H.; Stello, Dennis; Zasowski, Gail; Prieto, Carlos Allende; Chaplin, William J.; Hekker, Saskia; Johnson, Jennifer A.; Mészáros, Szabolcs; Mosser, Benoît; Anders, Friedrich; Basu, Sarbani; Beers, Timothy C.; Chiappini, Cristina; da Costa, Luiz A. N.; Elsworth, Yvonne; García, Rafael A.; Pérez, Ana E. García; Hearty, Fred R.; Maia, Marcio A. G.; Majewski, Steven R.; Mathur, Savita; Montalbán, Josefina; Nidever, David L.; Santiago, Basilio; Schultheis, Mathias; Serenelli, Aldo; Shetrone, Matthew,
Bayesian distances and extinctions for giants observed by Kepler and APOGEE,
Monthly Notices of the Royal Astronomical Society, 2014, Volume 445, Issue 3, p.2758-2776

## Articles published in conference proceedings

1 Lagarde, N.; Miglio, A.; Eggenberger, P.; Montalbán, J.; **Bossini, D.**,
Constraining angular momentum transport processes in stellar interiors with red-giant stars in the open cluster NGC6819,
The Space Photometry Revolution - CoRoT Symposium 3, Kepler KASC-7 Joint Meeting, Toulouse, France, Edited by R.A. García; J. Ballot; EPJ Web of Conferences, 2015, Volume 101, id.06042

2 **Bossini, Diego**; Miglio, Andrea; Salaris, Maurizio; Girardi, Léo; Montalbán, Josefina; Bressan, Alessandro; Marigo, Paola; Noels, Arlette
The AGB bump: a calibrator for core mixing
The Space Photometry Revolution - CoRoT Symposium 3, Kepler KASC-7 Joint Meeting, Toulouse, France, Edited by R.A. García; J. Ballot; EPJ Web of Conferences, 2015, Volume 101, id.06012

3 Campante, Tiago; Lopes, Ilídio; **Bossini, Diego**; Miglio, Andrea
Asteroseismology of red-giant stars as a novel approach in the search for grav-

itational waves
IAU General Assembly, Meeting 29th, 2015 ,id.2252323

4 Girardi, Léo; Barbieri, Mauro; Miglio, Andrea; **Bossini, Diego**; Bressan, Alessandro; Marigo, Paola; Rodrigues, Thaíse S.
The Expected Stellar Populations in the Kepler and CoRoT Fields
Asteroseismology of Stellar Populations in the Milky Way, Astrophysics and Space Science Proceedings, 2015,Volume 39. ISBN 978-3-319-10992-3. Springer International Publishing Switzerland, p. 125

5 **Bossini, D.**; Girardi, L.; Miglio, A.; Bressan, A.; Marigo, P.
Combined photometric and asteroseismic constraints on the properties of NGC 6791
40th Liège International Astrophysical Colloquium. Ageing Low Mass Stars: From Red Giants to White Dwarfs, Liège, Belgium, Edited by J. Montalbán; A. Noels; V. Van Grootel; EPJ Web of Conferences, 2012, Volume 43, id.03005

## Oral presentations during conferences with scientific selection committee

1 **Bossini, Diego**
talk: Uncertainties on near-core mixing in red-clump stars: effects on the period spacing and on the luminosity of the AGB bump.
Seventh Meeting on Hot Subdwarfs and Related Objects, 2015, Oxford, United Kingdom

2 **Bossini, Diego**
talk: Uncertainties on near-core mixing in red-clump stars: effects on the period spacing and on the luminosity of the AGB bump.
The KASC8/TASC1 Workshop, 2015, Aarhus, Denmark

3 D. R. Reese, **D. Bossini**, G. Buldgen, T. L. Campante, W. J. Chaplin, H. R. Coelho, G. R. Davies, J. Kuszlewicz, A. Miglio
poster: Asteroseismology with the AIMS code
The KASC8/TASC1 Workshop, 2015, Aarhus, Denmark

4 **Bossini, Diego**; Miglio, Andrea; Salaris, Maurizio; Girardi, Léo; Montalbán, Josefina; Bressan, Alessandro; Marigo, Paola; Noels, Arlette
poster: Uncertainties on Near-Core Mixing in Red-Clump Stars: effects on the

period spacing and on the luminosity of the AGB bump
CoRoT Symposium 3, Kepler KASC-7 joint meeting, 2014,Toulouse. France

5 Lagarde, N.; Miglio, A.; Eggenberger, P.; Montalbán, J.; **Bossini, D.**,
Constraining angular momentum transport processes in stellar interiors with red-giant stars in the open cluster NGC6819,
CoRoT Symposium 3, Kepler KASC-7 joint meeting, 2014,Toulouse. France

6 **Bossini, Diego**; Miglio, Andrea; Salaris, Maurizio; Girardi, Léo; Montalbán, Josefina; Bressan, Alessandro; Marigo, Paola
The AGB bump: a calibrator for core mixing
CoRoT Symposium 3, Kepler KASC-7 joint meeting, 2014,Toulouse. France
Asteroseismology of stellar populations in the Milky Way, 2013, Sexten, Italy

7 **Bossini, D.**; Girardi, L.; Miglio, A.; Bressan, A.; Marigo, P.
poster: Combined Photometric and Asteroseismic Constraints on the Proprieties of NGC 6791
Astrophysical Colloquium,Ageing low mass stars: from red giants to white dwarf, 2012, Líege, Belgium

# Bibliography


Aerts C., 2015, in IAU Symposium, Vol. 307, New Windows on Massive Stars, Meynet G., Georgy C., Groh J., Stee P., eds., pp. 154–164

Aerts C., Christensen-Dalsgaard J., Kurtz D. W., 2010, Asteroseismology, Springer, ed.

Alcock C. et al., 1997, ApJ, 482, 89

Angulo C. et al., 1999, Nuclear Physics A, 656, 3

Baglin A. et al., 2006, in COSPAR Meeting, Vol. 36, 36th COSPAR Scientific Assembly, p. 3749

Basu S. et al., 2011, ApJ, 729, L10

Beccari G., Ferraro F. R., Lanzoni B., Bellazzini M., 2006, ApJ, 652, L121

Beck P. G. et al., 2011, Science, 332, 205

Bedding T. R. et al., 2011, Nature, 471, 608

Benomar O., Takata M., Shibahashi H., Ceillier T., García R. A., 2015, MNRAS, 452, 2654

Berthomieu G., Provost J., 1988, in IAU Symposium, Vol. 123, Advances in Helio- and Asteroseismology, Christensen-Dalsgaard J., Frandsen S., eds., p. 121

Bono G., Caputo F., Cassisi S., Castellani V., Marconi M., 1997, ApJ, 479, 279

Bono G., Castellani V., degl'Innocenti S., Pulone L., 1995, A&A, 297, 115

Borucki W. J., Koch D., Basri G., et al., 2010, Science, 327, 977

Bossini D. et al., 2015, MNRAS, 453, 2290

Brassard P., Fontaine G., Wesemael F., Hansen C. J., 1992, ApJS, 80, 369

Bressan A., Bertelli G., Chiosi C., 1986, Mem. Soc. Astron. Italiana, 57, 411

Bressan A., Girardi L., Marigo P., Rosenfield P., Tang J., 2015, Astrophysics and Space Science Proceedings, 39, 25

Bressan A., Marigo P., Girardi L., Nanni A., Rubele S., 2013, in European Physical Journal Web of Conferences, Vol. 43, European Physical Journal Web of Conferences, p. 3001

Bressan A., Marigo P., Girardi L., Salasnich B., Dal Cero C., Rubele S., Nanni A., 2012, MNRAS, 427, 127

Brogaard K., Bruntt H., Grundahl F., Clausen J. V., Frandsen S., Vandenberg D. A., Bedin L. R., 2011, A&A, 525, A2

Broomhall A.-M., Chatterjee P., Howe R., Norton A. A., Thompson M. J., 2014, Space Sci. Rev., 186, 191

Brown T. M., Gilliland R. L., Noyes R. W., Ramsey L. W., 1991, ApJ, 368, 599

Buonanno R., Corsi C. E., Fusi Pecci F., 1985, A&A, 145, 97

Caffau E., Ludwig H.-G., Steffen M., Freytag B., Bonifacio P., 2011, Sol. Phys., 268, 255

Campbell S. W., Lattanzio J. C., 2008, A&A, 490, 769

Cannon R. D., 1970, MNRAS, 150, 111

Caputo F., Castellani V., Wood P. R., 1978, MNRAS, 184, 377

Caputo F., Chieffi A., Tornambe A., Castellani V., Pulone L., 1989, ApJ, 340, 241

Cassisi S., Salaris M., 2013, Old Stellar Populations: How to Study the Fossil Record of Galaxy Formation, Wiley, ed.

Cassisi S., Salaris M., Irwin A. W., 2003, ApJ, 588, 862

Castellani V., Chieffi A., Pulone L., 1991, ApJS, 76, 911

Castellani V., Chieffi A., Tornambe A., Pulone L., 1985, ApJ, 296, 204

Castellani V., Giannone P., Renzini A., 1971a, Ap&SS, 10, 340

—, 1971b, Ap&SS, 10, 355

Catelan M., 2007, in American Institute of Physics Conference Series, Vol. 930, Graduate School in Astronomy: XI Special Courses at the National Observatory of Rio de Janeiro (XI CCE), Roig F., Lopes D., eds., pp. 39–90

—, 2009, in IAU Symposium, Vol. 258, IAU Symposium, Mamajek E. E., Soderblom D. R., Wyse R. F. G., eds., pp. 209–220

Caughlan G. R., Fowler W. A., 1988, Atomic Data and Nuclear Data Tables, 40, 283

Chaplin W. J., Miglio A., 2013, ARA&A, 51, 353

Chiosi C., 2007, in IAU Symposium, Vol. 239, IAU Symposium, Kupka F., Roxburgh I., Chan K. L., eds., pp. 235–246

—, 2008, Struttura ed evoluzione delle stelle

Christensen-Dalsgaard J., 2002, Reviews of Modern Physics, 74, 1073

—, 2012, in Astronomical Society of the Pacific Conference Series, Vol. 462, Progress in Solar/Stellar Physics with Helio- and Asteroseismology, Shibahashi H., Takata M., Lynas-Gray A. E., eds., p. 503

Christensen-Dalsgaard J., Monteiro M. J. P. F. G., Rempel M., Thompson M. J., 2011, MNRAS, 414, 1158

Constantino T., Campbell S. W., Christensen-Dalsgaard J., Lattanzio J. C., Stello D., 2015, MNRAS, 452, 123

Constantino T., Campbell S. W., Lattanzio J. C., van Duijneveldt A., 2016, MNRAS, 456, 3866

Corsaro E. et al., 2012, ApJ, 757, 190

Cunha M. S., Stello D., Avelino P. P., Christensen-Dalsgaard J., Townsend R. H. D., 2015, ApJ, 805, 127

Cyburt R., Schatz H., Smith K., Warren S., 2007, in APS Division of Nuclear Physics Meeting Abstracts, p. J8

Cyburt R. H. et al., 2010, ApJS, 189, 240

da Silva L. et al., 2006, A&A, 458, 609

Dalcanton J. J. et al., 2012, ApJS, 200, 18

degl'Innocenti S., Fiorentini G., Ricci B., Villante F. L., 2004, Physics Letters B, 590, 13

Deheuvels S., Brandão I., Silva Aguirre V., Ballot J., Michel E., Cunha M. S., Lebreton Y., Appourchaux T., 2016, ArXiv e-prints

Deubner F.-L., Gough D., 1984, ARA&A, 22, 593

Ferguson J. W., Alexander D. R., Allard F., Barman T., Bodnarik J. G., Hauschildt P. H., Heffner-Wong A., Tamanai A., 2005, ApJ, 623, 585

Ferraro F. R., Messineo M., Fusi Pecci F., de Palo M. A., Straniero O., Chieffi A., Limongi M., 1999, AJ, 118, 1738

Gabriel M., Noels A., Montalbán J., Miglio A., 2014, A&A, 569, A63

Gallart C., 1998, ApJ, 495, L43

Gautschy A., Althaus L. G., 2007, A&A, 471, 911

Girardi L., 1999, MNRAS, 308, 818

Girardi L. et al., 2012, in Red Giants as Probes of the Structure and Evolution of the Milky Way, Miglio A., Montalbán J., Noels A., eds., p. 165

Girardi L., Salaris M., 2001, MNRAS, 323, 109

Godart M., 2007, Communications in Asteroseismology, 150, 185

Grevesse N., Noels A., 1993, Physica Scripta Volume T, 47, 133

Herwig F., 2000, A&A, 360, 952

—, 2005, ARA&A, 43, 435

Iglesias C. A., Rogers F. J., 1996, ApJ, 464, 943

Imbriani G., Limongi M., Gialanella L., Terrasi F., Straniero O., Chieffi A., 2001, ApJ, 558, 903

Jiang C., Christensen-Dalsgaard J., 2014, MNRAS, 444, 3622

Kippenhahn R., Weigert A., Weiss A., 2013, Stellar Structure and Evolution, Springer, ed.

Kjeldsen H., Bedding T. R., 1995, A&A, 293

Krishna Swamy K. S., 1966, ApJ, 145, 174

Kunz R., Fey M., Jaeger M., Mayer A., Hammer J. W., Staudt G., Harissopulos S., Paradellis T., 2002, ApJ, 567, 643

Maeder A., 1975, A&A, 40, 303

Marigo P., Aringer B., 2009, A&A, 508, 1539

Marino A. F., Villanova S., Piotto G., Milone A. P., Momany Y., Bedin L. R., Medling A. M., 2008, A&A, 490, 625

Mazzitelli I., D'Antona F., 1986, ApJ, 308, 706

Metcalfe T. S., Salaris M., Winget D. E., 2002, ApJ, 573, 803

Miglio A. et al., 2012, MNRAS, 419, 2077

—, 2016, MNRAS, 461, 760

—, 2013a, in European Physical Journal Web of Conferences, Vol. 43, European Physical Journal Web of Conferences, p. 03004

—, 2013b, MNRAS, 429, 423

Miglio A., Montalbán J., Noels A., Eggenberger P., 2008, MNRAS, 386, 1487

Montalbán J., Miglio A., Noels A., Dupret M.-A., Scuflaire R., Ventura P., 2013, ApJ, 766, 118

Montalbán J., Noels A., 2013, in European Physical Journal Web of Conferences, Vol. 43, European Physical Journal Web of Conferences, p. 3002

Mosser B. et al., 2011, A&A, 532, A86

—, 2014, A&A, 572, L5

—, 2012a, A&A, 537, A30

—, 2012b, A&A, 540, A143

Nelder J. A., Mead R., 1965, Computer Journal, 7, 308

Nidever D. L. et al., 2014, ApJ, 796, 38

Noels A., Montalban J., Miglio A., Godart M., Ventura P., 2010, Ap&SS, 328, 227

Paxton B., Bildsten L., Dotter A., Herwig F., Lesaffre P., Timmes F., 2011, ApJS, 192, 3

Paxton B. et al., 2013, ApJS, 208, 4

—, 2015, ApJS, 220, 15

Pietrinferni A., Cassisi S., Salaris M., Castelli F., 2004, ApJ, 612, 168

—, 2006, ApJ, 642, 797

Pietrinferni A., Cassisi S., Salaris M., Hidalgo S., 2013, A&A, 558, A46

Pinsonneault M. H. et al., 2014, ApJS, 215, 19

Piotto G. et al., 2002, A&A, 391, 945

Rodrigues T. S. et al., 2014, MNRAS, 445, 2758

Roxburgh I. W., 1992, A&A, 266, 291

Salaris M., 2007, in American Institute of Physics Conference Series, Vol. 948, Unsolved Problems in Stellar Physics: A Conference in Honor of Douglas Gough, Stancliffe R. J., Houdek G., Martin R. G., Tout C. A., eds., pp. 87–98

Salaris M., Chieffi A., Straniero O., 1993, ApJ, 414, 580

Sandquist E. L. et al., 2013, ApJ, 762, 58

Sarajedini A. et al., 2007, AJ, 133, 1658

Schönberg M., Chandrasekhar S., 1942, ApJ, 96, 161

Schwarzschild M., 1958, Structure and evolution of the stars.

Schwarzschild M., Härm R., 1965, ApJ, 142, 855

Scuflaire R., Montalbán J., Théado S., Bourge P.-O., Miglio A., Godart M., Thoul A., Noels A., 2008, Ap&SS, 316, 149

Stello D. et al., 2011, ApJ, 739, 13

Straniero O., Domínguez I., Imbriani G., Piersanti L., 2003, ApJ, 583, 878

Sweigart A. V., Lattanzio J. C., Gray J. P., Tout C. A., 2000, in Liege International Astrophysical Colloquia, Vol. 35, Liege International Astrophysical Colloquia, Noels A., Magain P., Caro D., Jehin E., Parmentier G., Thoul A. A., eds., p. 529

Tassoul M., 1980, ApJS, 43, 469

Townsend R. H. D., Teitler S. A., 2013, MNRAS, 435, 3406

Unno W., Osaki Y., Ando H., Saio H., Shibahashi H., 1989, Nonradial oscillations of stars

Vrard M., Mosser B., Samadi R., 2016, A&A, 588, A87

White T. R. et al., 2011, ApJ, 742, L3

Zahn J.-P., 1991, A&A, 252, 179